UNIVERSITY OF NAPLES FEDERICO II

DEPARTMENT OF INDUSTRIAL ENGINEERING

PH.D. COURSE IN INDUSTRIAL ENGINEERING

COORDINATOR PROF. MICHELE GRASSI

XXIV CYCLE

PH.D. THESIS

DISTRIBUTED SAR SYSTEMS BASED ON CLUSTER OF COMPACT MODULAR SATELLITES FOR NEW EARTH OBSERVATION MISSIONS

By

Marco Grasso

Supervisors:

Alfredo Renga

Maria Daniela Graziano

Michel Grassi

Abstract

A space program targeted to rapid develop and launch high-performance small satellites for Earth Observation (EO) represents a big challenge for the present and the next generation of satellite designers. Indeed, many EO scientific missions have very tight requirements which usually can be met only by traditional large satellites. Moreover, platform design is typically complex and time-consuming, with a strong relation to the specific mission scenario. The ability to start and complete an affordable space program based on small satellites in short timeframe, with performance capabilities suitable for high-demanding scientific missions, is linked to the exploitation of some promising paradigms, introduced in last decades. These paradigms are distributed mission configurations enabling advanced operational modes, fleet of compact satellites flying in formation, and modular design for new satellite development techniques.

This PhD thesis aims to analyze the paradigms in question by focusing on different concepts for the design of distributed Synthetic Aperture Radar (DSAR) systems based on modular small satellites flying in close formation. In a first step, a literature review on distributed SAR systems, small satellites, and spacecraft modularity has been conducted. This is intended to define the state-of-the-art and the current technological capabilities. Subsequently, different applications enabled by the distribution of SAR payload are collected and described. Procedures to select system parameters (e.g., the number of platforms and suitable formation configurations) are also given. To demonstrate distributed concepts, several scenarios have been designed, simulated, and tested. Each scenario involves a specific space architecture with different mission configurations to evaluate the performance enhancements achievable by exploiting DSAR techniques.

Afterwards, a DSAR simulator is introduced to evaluate the effects of different error sources on system performances. These error sources are modelled and applied during the processing phase, enabling the estimation of the effects in terms of bistatic SAR focusing and high level DSAR processing. Critical design aspects related to spacecraft subsystems dictated by formation-flying and SAR operations are addressed to confirm the technical feasibility of the spaceborne distributed system based on compact satellites. Additionally, technological aspects and space components related to satellite budgets are outlined, in order to match mission requirements with either space-qualified or in-development hardware, feasible for small platforms.

Finally, methodologies and concepts for the development of a modular satellite architecture have been investigated in this thesis. These concepts were analyzed to identify the problems that arise by designing a traditional satellite subsystem in a modular fashion. The focus of this work is specifically on the Attitude Determination and Control Subsystem (ADCS) considered as a reference point for the design of the entire modular platform since it is strongly coupled with other subsystems. In this context, a solution for abstracting the attitude estimation algorithms from the actual hardware is discussed. The proposed algorithm is a generic version of the Murrell’s Multiplicative Extended Kalman Filter (MMEKF) used to perform attitude estimation for different test cases with different pointing modalities and accuracies, different spacecraft and hardware configurations, without any modifications from case to case.

In summary, this thesis analyses distributed SAR systems in several respects evaluating the performances of different mission scenarios, achievable by exploiting new operational modes, and the feasibility of using small satellites as the reference platforms for the missions. In addition, a preliminary investigation about spacecraft modularity is performed to develop a generic and reusable method for attitude estimation.

Table of contents

List of Figures

List of Tables

List of Acronyms

ADCS	Attitude Determination and Control Subsystem
AFRL	Air Force Research Laboratory
ARF	Antenna Reference Frame
ASIM	Applique Sensor Interface Module
COTS	Commercial-Off-The-Shelf
CRE	Coherent Resolution Enhancement
CRS	Cellular Reconfigurable Spacecraft
DC	Duty Cycle
DOD	Depth-of-Descharge
DPCA	Displaced Phase Center Antenna
DSAR	Distributed SAR Systems
ECEF	Earth-Center Earth-Fixed
EDS	Electronic Datasheet
EO	Earth Observation
EPS	Electrical Power Subsystem
FF-SAR	Formation Flying SAR
GMTI	Ground Moving Target Indication
GNSS	Global Navigation Satellite System
GPS	Global Positioning Receiver
HPBW	Half Power Beamwidth
HRWS	High-Resolution Wide-Swath
ILS	Inter Satellite Link
InSAR	SAR Interferometry
IRW	Impulse Response Width

ISLR	Integrated Side Lobe Ratio
LEB	Long Effective Baseline
LEO	Low-Earth Orbit
LLA	Latitude, Longitude, and Altitude
LOS	Line-Of-Sight
LS	LookUp Service
MB-InSAR	Multi-Baseline SAR Interferometry
MMEKF	Multiplicative Extended Kalman Filter
NESZ	Noise Equivalent Sigma Zero
PnP	Plug and Play
PRF	Pulse Repetition Frequency
PSLR	Peak Side Lobe Ratio
RD	Range Doppler
RRL	Reuse Readiness Levels
SA	Solar Array
SAR	Synthetic Aperture Radar
SAT	Safe Along-Track
SM	Subnet Manager
SNR	Signal-to-Noise Ratio
SPA	Space Plug and Play Architecture
SSM	SPA Service Manager
SSO	Sun Synchronous Orbit
SWaP	Size, Width and Power
UHF	Ultra High Frequency
USO	Ultra Stable Oscillators
xTEDS	Extended Transducer Electronic Data Sheet

1. Introduction

1.1 Motivation

The need for high-performance and low-cost systems is redefining the way in which Synthetic Aperture Radar (SAR) missions for Earth Observation (EO) must be designed. Traditional monolithic SAR missions based on large and expensive satellites are expected to be substituted by distributed SAR systems (DSAR) [1] based on number of compact and cheap platforms [2]. In the same way, integral platforms, customized for very specific mission with time-consuming development cycles and difficult product changes, are very likely to be replaced by modular platforms characterized by reusable design, ease component modifications, high flexibility, and standardization [3]. The synergetic use of these new paradigms will lead the development of the next generation of EO systems whose key elements can be summarized as follows:

- Distribution. Many EO missions can experience the advantages to have a large amount of information acquired by many tiny platforms in aggregate. In this sense, the belief that “more is better” can be no longer just an old myth.
- Miniaturization. The advances in technology are drastically improving the performance of microelectronics, compact hardware, and nanotechnologies. High performance components can be effectively packed into smaller and smaller spaces.
- Modularity. The ability to develop and launch platforms quickly can be the game changer for the next EO space systems.

Specifically, the distribution of SAR payload on more than one platform flying in close formation, i.e., Formation-Flying SAR (FF-SAR) system [4]-[8], can guarantee the enhancement of SAR performance of the whole cluster with respect to the single isolated platform. Indeed, the formation can be properly designed to enable and/or to improve particular applications, as pulse repetition frequency (PRF) relaxation and the enlargement of observable unambiguous swath width [5]. In addition, the availability of multiple observations of the same area can improve the Signal-to-Noise-Ratio (SNR). Compact satellites, at the same time, can be rapidly assembled using commercial-off-the-shelf (COTS) components, which substantially decreases development costs with limited size and launch mass of the platform. Finally, the facility of replacing single element of the formation in case of failure, coupled with high responsiveness to new available technologies, enhances the overall reliability [9]. Modularity, instead, is a powerful weapon for shortening development cycles in a dramatic way by using standardized and reusable modules, universal interfaces and protocols, generic design, and a set of conventions to rapid integrate a flexible and cost-effective platform [10].

Despite these capabilities, moving from theory to practice is far from easy. The distribution of SAR payload among several co-flying platforms poses new technological challenges, e.g. formation-flying, multistatic SAR synchronization, multistatic SAR processing [5], [11]. The use of CubeSat, strong limited in Size, Width and Power (SWaP), to perform SAR observations and formation-flying operations, represents a major setback towards the feasibility of this kind of system [12]. Finally, the implementation of modularity is likely to require a higher initial investment to determine how to split out functional units, develop the common core units and variants, and design the standardized interfaces and processes [13]. Consequently, all these paradigms are still active research topics, requiring analysis and investigation for answering the questions they posed. For example, important questions to be addressed are:

- What are the relations between DSAR working modes and system parameters in terms of number of platforms, formation configurations, and signal processing?
- What are the effects of error sources on DSAR performance when applied to real world applications?
- How formation-flying SAR operations impact on the design of platform at subsystem level?
- Is it possible, at least in theory, to use small satellites in high-demanding scenarios as the ones posed by FF-SAR system?
- Can the current technology available for small satellites provide the required performances in terms of generation of power, pointing requirements and orbit control, communication link budgets, and propulsive capabilities?

- What are the problems that arise by designing a traditional satellite subsystem in a modular fashion?

To answer the first question, the fundamental applications of distributed SAR system are first described and then translated into specific space architectures pointing out the related design issues. To this aim, the definition of the minimum number of required platforms, suitable formation-flying configurations, and techniques for signal processing, is given for each application. To understand the effect of error sources on DSAR performances a simulation environment has been developed to model and integrate each error in the bistatic SAR focusing and DSAR processing chain. The effects are evaluated in terms of main imaging SAR parameters (geometric/radiometric resolution, ambiguity to noise ratio, integrated side-lobe ratio, peak to side-lobe ratio). The third question is addressed by defining the capabilities the platform must have to perform both formation-flying and SAR operations. These capabilities are then converted into specific subsystem requirements. A step-by-step procedure to design each subsystem is reported to provide preliminary budget estimates needed to confirm the feasibility to use small satellites in the selected class (e.g., microsatellites, nanosatellites, CubeSat). The results of the preliminary design are used to carry out a market analysis to individuate appropriate hardware for small satellite applications fulfilling the requirements. Finally, in the context of modularity the focus was put on the Attitude Determination and Control Subsystem (ADCS). This because the design of ADCS is strictly interconnected with other subsystems, as well as with the specific configuration of the platform, and, consequently, an investigation on modular ADCS can be a good reference for designing other satellite modular subsystems.

1.2 Contribution of this work

The purpose of this thesis is to propose reference guidelines to answer the questions stated above. To this aim, this study is intended to put together theoretical concepts, numerical tools/simulations, and procedures to be followed for designing distributed SAR systems using small satellites and modularity, and for improving the general knowledge about the subject.

To achieve this goal, this thesis provides:

- Literature review about DSAR, small satellites, and spacecraft modularity

- Systematic analysis about FF-SAR systems
- Application of FF-SAR concept to different test case scenarios
- Preliminary design examples of small satellites in different classes at both system and subsystem level
- Description of numerical tools and simulation environments
- Generic and reusable attitude estimation algorithm applied to different missions with different pointing requirements, hardware configuration, and spacecraft properties

2. State-of-the-Art

2.1 Distributed SAR systems

In the last two decades a huge effort has been undertaken to demonstrate in space distributed concepts for new satellite systems. In this respect, some missions relying on two cooperative satellites have been successfully flown: GRACE (aimed at gravimetry) [14], PRISMA (a technology demonstrator) [15], and TanDEM-X (high-resolution SAR interferometry) [16]. These missions represent great achievements, and they are likely to be the precursors of future Earth observation missions based on multiple co-flying platforms.

With specific reference to DSAR, no space mission has been realized yet demonstrating and exploiting the relevant properties and peculiarities. Nonetheless, important examples of mission concepts based on the idea of a SAR distributed among several formation flying satellites have been proposed. These missions can be divided in two main categories: companion and fully active configuration (Figure 1).

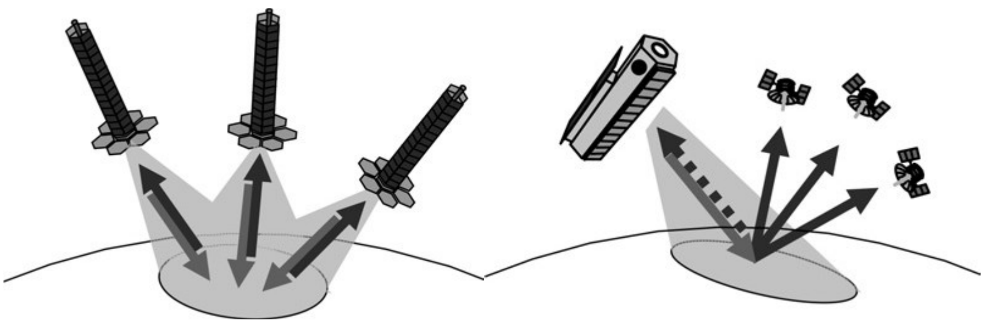

Figure 1 Example of fully active configuration (left) and companion configuration (right) [17]

In a companion or semi-active configuration, a single-active satellite transmits the radar signal with a set of passive receivers onboard a small satellite formation acquiring the backscattered echoes. In a fully active configuration, instead, each satellite has full monostatic capabilities. Fully active systems have, in general, higher sensitivity and flexibility, are less prone to ambiguities, and enable easier phase synchronization. Furthermore, they also provide a pursuit monostatic mode as a natural fallback solution in the case of problems with orbit control or instrument synchronization. In contrast, semi-active radar constellations have a significant cost-advantage and will therefore provide more interferometric baselines per unit money.

The first distributed SAR mission concept was the Interferometric Cartwheel [18], with three formation flying receive-only satellites using ENVISAT as common illuminator. Proposed in 1995, this was also the first SAR companion mission concept, where a formation flying low-cost satellites are used to acquire the backscattered echoes of an existing fully active transmitting satellite, allowing to reduce the costs of the mission. In the late 90s, TechSAT 21 mission was proposed [19], consisting in clusters of formation flying micro-satellites used in a cooperatively way to improve single satellite capabilities. As companion SAR missions, BiSSAT was proposed [20] to complete COSMO/SkyMed with bistatic and interferometric capabilities. More recently, in 2014, SAOCOM CS was proposed [21], an ESA mission with two-satellite flying in formation with Argentina's L-band SAOCOM satellite [22], enabling for the first time single-pass interferometry in L-band. Even though these missions were never realized, their technological and scientific contributions to improve the know-how about DSAR systems is still considerable. The only successful mission which has flown is the TanDEM-X mission [16], proposed in 2004 as an add-on to the TerraSAR-X mission. Indeed, he TanDEM-X satellite was successfully launched in 2010, with the operative starting time of the mission in the same year. As examples of upcoming mission concepts, which are very likely to lead to space realization in the next years, SESAME [23] and Harmony [24] are two ESA missions proposed to extend the Sentinel-1 interferometric capabilities, enabling single-pass interferometric applications, while the MirrorSAR mission [25] is intended to continue and enhance DLR/German bi-/multistatic capabilities at X-Band. These mission concepts are based on satellite class more than 100 kg. Specifically, SESAME consists of two 200 kg class spacecraft, Harmony consists of two sub-500 kg class satellites while the space segment of MirrorSAR mission consists of three sub-500 kg satellites. All these missions are briefly described in the next sections.

2.1.1 Past mission concepts

Interferometric Cartwheel

The interferometric Cartwheel is a CNES patent concept, introduced by Massonnet [18], where three small and cheap microsatellites fly behind or ahead a bigger active SAR satellite. The active satellite is used as illuminator of opportunity, whose transmitted signal is backscattered from Earth surface and collect by the three passive satellites. The main purpose of this mission was to enable a low-cost multistatic mission with single-pass interferometry capability. The name comes from the orbital configuration known as cartwheel and illustrated in Figure 2.

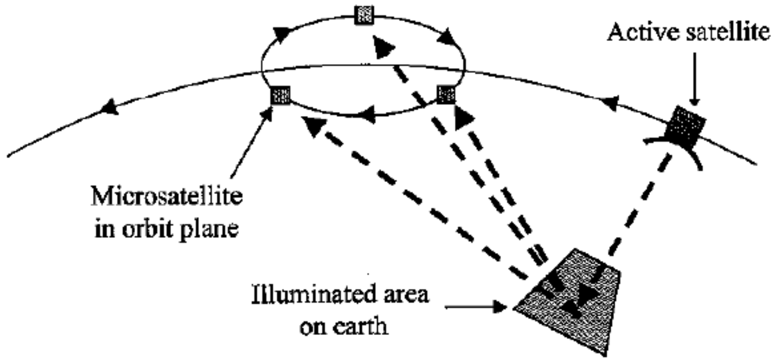

Figure 2 Interferometric Cartwheel configuration [18]

The primary mission goal was the computation of a Digital Elevation Model (DEM), exploiting cross-track formations. Secondary mission goals were the mapping of ocean currents, by using along-track interferometry, and volume scattering estimations. Despite the fact this mission had never been realized, its conceptual idea introduced a practical and feasible solutions to lots of conventional SAR limitations, introducing new SAR applications and technical challenges for future multistatic SAR missions.

TechSat-21

The first example of a real distributed SAR is represented by the TechSAT-21 concept [19] developed by US Air Force Research Laboratory. Clusters of cooperative micro-satellites flying in formation are used to match the performance of much larger, complex, and expensive single satellite. Each small satellite communicates with the others in the cluster and shares the processing, communications, payload, and mission functions. Thus, the cluster realizes a virtual bigger satellite. The key feature of TechSAT-21 is that the achievable angular resolution is not governed by the diameter of the individual apertures but by the maximum separation distance between them. This means that multiple aperture radar systems can use reasonably sized apertures located on separated spacecraft to achieve superior angular resolution while maintaining a broad coverage area. In addition, the signal combination provides an additional gain in the strength of the received signals after processing.

Figure 3 TechSat-21 [19]

BiSSAT

BiSSAT (Bi-static Sar SATellite) [20] was proposed as receiving-only passive SAR sensor to be deployed as an add-on to one satellite of Cosmo/SkyMed constellation. When envisaged, the main features of BiSSAT were:

- Possibility to manage new scientific applications and to explore novel applications
- Demonstrate the opportunities of a bistatic configuration
- Low-cost mission

A pictorial representation of BiSSAT geometry is shown in Figure 4. Even tough, the feasibility of the mission was demonstrated, the BiSSAT mission was never realized. Nevertheless, the outcomes of this study have represented a starting-point for the design of subsequent bistatic SAR missions.

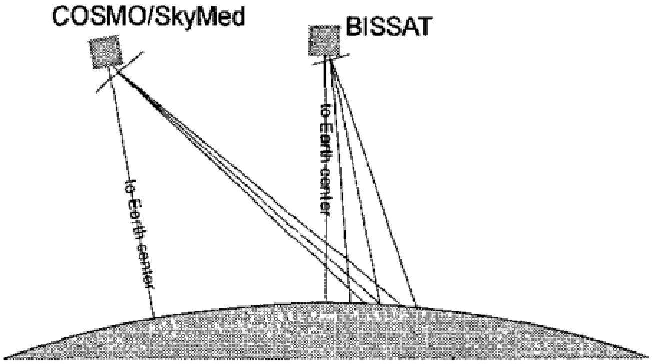

Figure 4 BiSSAT geometry [20]

SACOM-CS

SAOCOM-CS [21] was a passive companion satellite proposed to fly with Argentina's L-band SAR satellite SAOCOM. This was a mission concept studied by ESA to highlight the technical feasibility and the scientific value of a bi-static extension of SAOCOM constellation, using this passive, receive-only, satellite flying in formation with SAOCOM acting as illuminator. SAOCOM is a two-spacecraft constellation flying in sun-synchronous orbit operated by Argentina space agency through the Comisión Nacional de Actividades Espaciales (CONAE). CONAE's SAOCOM satellites are aimed to collect L-band SAR imagery, with full polarimetric and interferometric capabilities, for applications mainly in agriculture, hydrology, and forestry.

2.1.2 DSAR space demonstration

Currently, the TanDEM-X mission represents the only example of bistatic SAR mission turned into reality. Main mission characteristics are recalled in this section.

TanDEM-X

TanDEM-X (TerraSAR-X add-on for Digital Elevation Measurements) [16] is an extension of the TerraSAR-X (TSX) mission, which relies on a second satellite (TDX) orbiting in a close formation with TSX. The formation acts as a large single-pass radar interferometer with the opportunity for flexible baseline selection to generate an extremely accurate global DEM. This innovative spaceborne system represents the first operational example for demonstrating new SAR techniques and applications. The acquisition of unrivalled DEMs requires coordinated operation between the satellites, which is made possible by disposing them in a Helix configuration [17]. During a Tandem-X acquisition both the radars act as one interferometric SAR instrument with different sensitivities to detect ground targets. Data-take operations require both TSX and TDX operating in the same imaging modality (e.g., stripmap, Spotlight, ScanSAR) and polarization (single, dual and, experimental quad) mode. Three different cooperative modes can be implemented, as shown in Figure 5:

- pursuit monostatic
- bistatic
- alternating bistatic

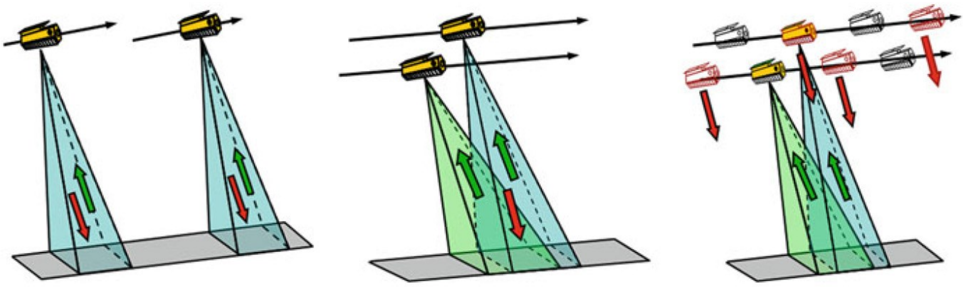

Figure 5 (left) Pursuit monostatic mode. (center) Bistatic. (right) Alternating bistatic [17]

During the first mode, both the monostatic SARs operate in an along-track configuration, with separations up to 20 km. This pattern enables pursuit monostatic imaging, with satellites just few seconds apart. On the other hand, bistatic modes use either TSX or TDX or alternate TSX and TDX as transmitter to illuminate common radar footprint on the Earth's surface. The scattered signal is then recorded by both satellites simultaneously. Bistatic and alternating bistatic configurations are classified as operational when along-track baselines are below 1 km and cross-track separations are below 4 km, respectively.

TanDEM-X mission was developed with the main goal of providing a global, consistent, and high-precision DEM of the Earth's surface with 2 m relative height accuracy at 12 m horizontal resolution, by means of single-pass SAR interferometry with variable across-track baseline between 200 to 500 m. In December 2010, the TanDEM-X global DEM acquisition started, with the following four years dedicated almost exclusively to data acquisition for DEM generation. The first global coverage (except Antarctica) was completed in January 2012. By the end of 2014, the Earth's entire land mass had been mapped at least twice (four times in the case of difficult terrain) with varying baselines. Delivery of DEM products started in 2014 and in October 2016 the delivery of all 19,389 DEM tiles covering the entire earth land mass was completed.

Beyond the generation of a global DEM as the primary mission goal, in October 2014 a science phase started. This phase was aimed at demonstrating the generation of even more accurate DEMs on local scales, applications based on along-track interferometry, and new SAR techniques. Specific focus was on multistatic SAR, polarimetric SAR interferometry, digital beamforming, and super resolution.

2.1.3 Upcoming mission concepts

Brand-new mission concepts have been recently proposed which are likely to lead to space realization in the next years. These mission concepts are illustrated in the next subsections.

HARMONY

The Harmony is a mission dedicated to augment the Sentinel-1 capabilities, proposed as one of an Earth Explorer 10 Mission Candidate to Observe Land, Ice, and Ocean Surface Dynamics. Augmentation is based on the use of several azimuth line-of-sights to support precise measurement of small-scale motion and deformation fields of the ocean surface, glaciers, and solid Earth. This is expected to generate important data required to better understand dynamic processes in these domains. The space segment of the mission will consist of two identical sub-500 kg class spacecraft carrying a receive-only radar instrument as the main payload and flying in a re-configurable formation with Sentinel-1 C or D, which will be used as illuminator [24].

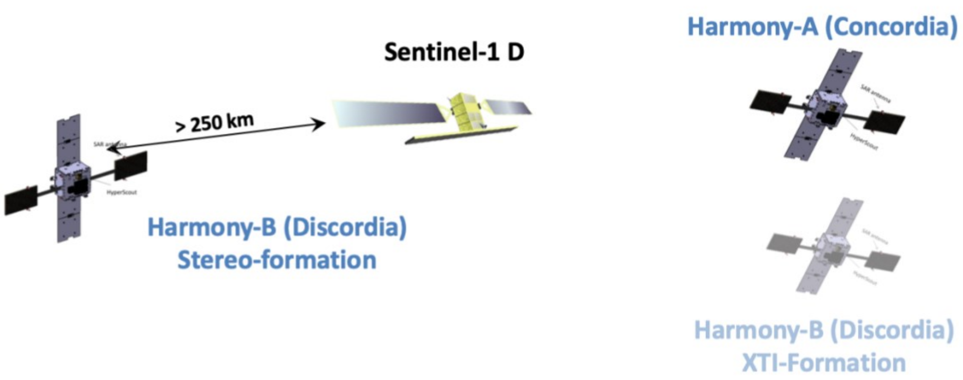

Figure 6 Harmony mission [24]

The Harmony mission will be organized in several phases, with different formation configurations optimized for the retrieval of deformation fields over land, ice, oceans, and topographic changes over land and ice. These configurations are stereo configuration, cross-track (XTI) configuration, and along-track (ATI) configuration. In stereo configuration, one spacecraft, Harmony-A, will fly 250 km ahead of Sentinel-1, with the other Harmony-B, at about the same distance behind Sentinel-1, sharing approximately the same orbital plane (see Figure 6).

MirrorSAR mission

Among the upcoming earth observation missions, the MirrorSAR mission [25] is intended to continue and enhance the DLR/German capabilities at X-Band. The mission is intended as the evolution of TerraSAR-X and TanDEM-X missions and will provide very high-resolution SAR data. MirrorSAR will use both digital beamforming and satellite formation flying as well as the newly available chirp bandwidth of 1200 MHz. This will lead to much better image resolution over very large swath widths. The system consists of one transmitter and N receiving-only system on separate platforms flying in close formation at a relatively long along-track separation (about 15 km) from the transmitter, as shown in Figure 7.

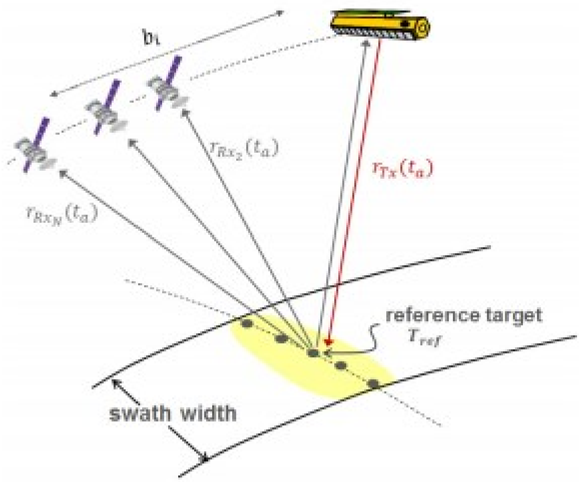

Figure 7 MirrorSAR configuration [25]

2.2 Small Satellites

The small satellite industry is experiencing disruptive changes over the last few years [2], [26]. Thanks to high level of flexibility, overall reliability, low costs, and high performance, small satellites are becoming more and more relevant for government space programs, small space consortia, commercial customers, and universities. With companies such as OneWeb and SpaceX intending to launch huge constellations of small satellites, this market seems to be ready to explode in the near future. As proof, the number of missions based on small satellites is continuously growing up in the last years, as listed in Table 1.

Table 1 Small Satellites Launches by Year

Year	Number of Launches
2010	10
2011	20
2012	19
2013	59
2014	70
2015	80
2016	91
2017	160
2018	322
2019	385
2020	1029

Satellites with a mass under 500 kg can be considered as small satellites. Indeed, small satellites are primarily classified according to the mass, as reported in Table 2.

Table 2 Satellite classification according to mass

Satellite classification	Mass (kg)
Minisatellites	200 to 500
Microsatellites	10 to 200
Nanosatellites	1 to 10
Picosatellites	< 1

Figure 8 shows some examples of small satellites in different classes.

Figure 8 Some examples of small satellites. Microsatellite (upper-left), minisatellite (upper-right), nanosatellite (bottom-left), picosatellite (bottom-right).

Nanosatellites can be further classified according to their volume to make CubeSats [27]. CubeSats are type of miniaturized satellites that are made up with multiple cubic units of standard dimensions [28]; specifically, one-unit, known as 1U, is sized 10x10x10 cm with a mass <1.33 kg [28]. Multiple units can be arranged in different form factors, as listed in Table 3. An important note is that while a maximum weight is prescribed as part of the CubeSat definition it is not a stringent requirement. Introduced in 1999 in the ambit of a university educational program, in the last decades the CubeSat concept has raised its importance in all space community. Indeed, it is becoming a reference point towards small platform design either for technology demonstration missions or scientific measurements [29]. The CubeSat standard enables great settings for satellite researcher and developers, including: (i) relatively simple design, high flexibility and adaptability to different mission requirements and design phases, (ii) general low costs, (iii) rapid technological capabilities development, (iv) a new space access philosophy [30]. CubeSats are carried into orbit as secondary payload, deployed in an orbit similar to the primary payload, or as soft-stowed cargo from the International Space Station. This enables faster and more frequent access to space [30]. Small space industries and university consortia have had the possibility to conduct their own space projects independently, thanks to unique capabilities introduced by CubeSats. The ease in the space access and the low development costs are particularly attractive for Earth observation (EO) missions too. Indeed, EO missions could take advantage from increased number of spatial and temporal acquisitions enabled by constellation or swarm of many co-flying small platforms. A great effort is being made both to propose and test new CubeSat-compatible radar components and to demonstrate solutions and algorithms for the nanosatellite autonomous formation-flying [29], [31]-[33].

Table 3 CubeSat classification

CubeSat name	Dimensions	Mass
CubeSat 1U	10 x 10 x 10 cm	1 – 1 kg
CubeSat 2U	10 x 10 x 20 cm	2 – 3 kg
CubeSat 3U	10 x 10 x 30 cm	3 – 5 kg
CubeSat 6U	10 x 20 x 30 cm	6 – 9 kg
CubeSat 12U	20 x 20 x 30 cm	12 – 15 kg

2.2.1 Radar missions based on CubeSat

The first radar mission based on CubeSat was RainCube [34]. The success of this mission has demonstrated in space the feasibility of a radar payload to work on-board a CubeSat platform. The satellite is a 6U CubeSat, deployed from International Space Station in June 2018, and it is still orbiting. The primary payload is an active real aperture radar (RAR), operating at Ka-band, designed with a miniaturized architecture enabling the reduction of the number of components, power consumption and mass, of one order with respect to other existing spaceborne radar systems. Specifically, the radar requires 22 W in transmission with a 10% duty cycle. Power reduces to 10 W in reception and to 3 W in stand-by mode. The antenna is a deployable parabolic antenna, Ka-band radar parabolic deployable antenna (KaRPDA) [35], with an aperture of 0.5m, a gain of 42.6 dB at 35.75 GHz, and a stowage volume of only 1.6U, thanks to the Cassegrain architecture (reflector placed below the focal point of the antenna). RainCube has achieved its main goal to make vertical precipitation profiling, at an altitude ranging from 0 to 18 km from earth surface, with a horizontal resolution <10 km and a vertical resolution <250m.

In the ambit of NASA Earth Science Technology Office (ESTO) program, the SRI international organization has designed and built a completely new and innovative S-band mini-SAR, the CubeSat Imaging Radar for Earth Science (CIRES) [36], as the radar sensor for a 16U CubeSat constellation aimed to interferometric SAR acquisitions for studying ground surface movements. The constellation will be composed by 27 CubeSat orbiting at 500 km altitude and 55° of inclination, to ensure global coverage and daily revisit time, in such a way to maximize the coherence of interferometric acquisitions. Currently under development, CIRES claims to obtain high SAR and InSAR performances with a very ultra-compact design. The declared resolution is 6 x 6 m (upgrade up to 1 m), a bandwidth of 40 MHz, with a peak power consumption of 600 W in transmission and 60 W average power. The radar fits in only 1.5 U with a mass <1kg and it consists of three components: power amplifier, transponder, and high-speed processor. The Physical Sciences Inc. (PSI) is developing a large deployable S-band membrane antenna [37], with high gain and an aperture of 1.6 x 3.2 m to meet SAR imaging requirements. The stowed volume is about 8U with a gain of 28.6 dB working at 3.6 GHz with 18% efficiency.

RainCube and CIRES characteristics are resumed in Table 4.

Table 4 RainCube and CIRES mission characteristics

Mission	Application	Payload	#Satellites	Status
RainCube	Precipitation profiling	RAR	1	Launched
CIRES	SAR interferometry	SAR	27	Development

2.2.2 Nanosatellite Formation-Flying missions

Several Formation-Flying missions have flown in the past years, with satellite class ranging from large to micro-scale: GRACE [39], aimed at gravimetry; GRAIL [38], a NASA mission of two 200 kg satellites that flew in formation to perform gravitational mapping of the moon; PRISMA [15], launched in 2010 to demonstrate formation-flying technology and procedures, based on two satellite, one of 150 kg (the active thrusting satellite) and the other one of 40 kg (only passive).

For what concerns nanoscale, more recently, different Formation-Flying missions based on CubeSat has been proposed. Successfully launched in 2014, the Canadian mission CanX-4&5 [40] has demonstrated, for the first time ever, that autonomous formation-flying is achievable at nanosatellite scale. The twin nanosatellites, CanX-4 and CanX-5 have performed different formation-flying operations in four configurations: two along-track (ATO) formations with 1000 and 500 m baselines, and two projected-circolar orbit (PCO), for which one satellite seems orbiting around the other if seen from the Earth. Each satellites have a cubic form with dimensions of 20x20x20cm and a mass of about 7 kg. The mission has accomplished all mission objectives set, achieving an accuracy of 1 m and 10 cm in control and relative positioning, respectively, with a 0.5° and 1.0° accuracy in attitude determination and control. Each spacecraft is equipped with 4 UHF antennas, two S-band antennas for downlink, two S-band antennas for Inter Satellite Link (ILS), with 5 km range capabilities and a data rate of 10 kbit/s, GPS receiver and antennas for absolute and relative positioning, an on-board computer to perform formation-flying algorithms, such the FIONA algorithm [41], that reduce fuel consumption during maintenance and orbit reconfiguration manoeuvres. Control propulsive capabilities has been provided by the micro-propulsion sytem CNAPS [42], that is a cold gas thruster, developed for small platform applications, able to provide 18 m/s of total delta-V, a specific impulse of 45s, thrust of 5 mN, with a mass of 1.5 kg, volume of 2U and a steady-state power consumption of 0.25 W.

The CubeSat Proximity Operations Demonstration (CPOD) mission [43] seeks to demonstrate rendezvous, proximity and docking operations with two 3U CubeSats. The success of this mission will give useful information for future small sat formation-flying missions, enhancing the level of technological readiness of different formation-flying systems and subsystems, as for example, relative navigation systems, attitude control and determination subsystems, and micro-propulsion system for nanoplatforms. The launch is scheduled in the late 2021. The satellites have been built by Tyvak Nano-Satellite Systems, Inc. using CubeSat standard, with dimensions of 10x10x33cm and mass of about 5kg. They will be equipped with attitude determination and control components with an accuracy of 0.15° and 0.25°, respectively, GPS receiver, a kilometric ISL and the VACCO propulsion unit [44], a cold gas thruster delivering a total delta-V of 30 m/s, specific impulse of 40s, maximum thrust of 25 mN, with a wet mass of 1.244 kg and a volume of 1U.

Another example of formation-flying mission based on small-satellites is The Space Autonomous Mission for Swarming and geOlocation with nanosatellites (SAMSON) [45] aimed at demonstrating in space new algorithms for cluster-keeping and geolocation by using a cluster of three formation-flying CubeSats.

Last but not the least, RACE, Rendezvous Autonomous CubeSats Experiment [46], is intended as a mission concept aimed to test and demonstrate the capability of two 6U CubeSats, flying in close formation, to deal with different close-proximity operations, as rendezvous, docking and flyby around uncooperative targets.

Table 5 resumes the characteristics of the above-described missions.

Table 5 Formation-flying missions based on nanosatellites

Mission	Application	Class	#Satellites	Status
CanX-4&5	Formation-flying	Nanosatellites	2	Launched
CPOD	Proximity operations	3U	3	Launch in late 2021
SAMSON	Cluster-keeping and geolocations	3U	2	Launched
RACE	Proximity operations	6U	2	Development

2.2.3 Microsatellites SAR missions

ICEYE is building a constellation of 18 X-band SAR microsatellites [47], with the aim to offer a global service, delivering products each few hours to encounter different customer needs. Currently, 7 satellites have been launched, operative in orbit, with the first launch of IceEye-X1 in 2018, while the last two satellites, IceEye X-6 and IceEye X-7 were launched on 28 September 2020, as secondary payload on Soyuz. High resolution imagery or, in contrast, wide swath imaging, enable different application in different fields. In particular, ICEYE mission results ideal for maritime surveillance, glacier mapping and ice pack spotting. ICEEYE satellite are X-band SAR microsatellites (9.65 GHz), working in side-looking (both left and right), with a mass of 85 kg. They are equipped with active phased array antenna (electronically steerable) whose dimensions are 3.2 x 0.4 m. SAR units work at PRF of 2-10 kHz, bandwidth of 40-300 MHz, peak power of 4 kW and single polarization (VV). The available imaging modes are Stripmap and Spotlight. In the Stripmap mode the incidence angles range is 10-30°, while in the Spotlight mode is 20-35°. For what concerns SAR performances, the Stripmap mode allows to obtain a nominal swath of 30 km, with a ground range resolution of 3m and an azimuth resolution of 2.5-3 m. In the Spotlight mode, the swath is about 5 km, while the resolution improves up to 1 x 1 m, ground range x aximuth. The NESZ value is < -17dB.

NovaSAR-1 is a small S-band SAR satellite mission [48], developed as technology demonstrator to test the feasibility of SAR payload from small platform at low-cost. All main mission objectives can be linked to the scope of making SAR observations more affordable, frequent and reliable. Thanks to medium resolution capabilities and very wide swath imagery, the EO applications are manifold, including maritime, disaster monitoring, land classification, mineral mapping, elevation models, cartography and biodiversity monitoring. Moreover, as secondary payload, NovaSAR-1 is carrying out an Automatic Identification System (AIS), that, integrating its own data with SAR measurements, enables high-capability for shipping, fishing, and maritime surveillance from space. For what concerns satellite orbit, platform and payload specifications, NovaSAR-1 is orbiting at 583 km in a Sun-Synchronous Orbit (SSO) 10:30 am LTAN, with repeat cycle of 14 days and 97 mins per orbit. The satellite mass is of 450 kg, and it is equipped with a microstrip patch phased array antenna, whose dimensions are 3 x 1 m. S-band SAR operates at frequency of 3.1-3.3 GHz, in multiple polarisations, with a data cycle of 2 minutes, with a peak RF power of 1.8 kW. The designed lifetime of about 7 years. Four different imaging modes are available, depending on the use case: the Stripmap mode can be used for precise observations, with high resolution (6 m) and small swath (13-20 km); the ScanSAR mode represents the nominal mode with a medium resolution of 20 m and medium swath of 50-100 km; for monitoring large areas, the ScanSAR wide mode enables wide swath (up to 195 km) but with low resolution of 30-50 m; for ship detection applications, in combination with AIS data, it is possible the maritime mode characterized very wide swath (up to 400 km).

As part of feasibility study of low-cost SAR working from 100kg-class microsatellites, authors in [49] proposed a new architecture for a compact X-band SAR. X-band is selected to achieve high resolution with low satellite mass and high observation frequency. RF peak power is about 1000 W achievable with GaN solid state amplifiers. At 618 km altitude, with a NESZ of -20 dB, a ground range resolution of 10 m can be obtained, while 3 m in case of degraded NESZ of -15 dB. At 400 km altitude, high ground range resolution of 1 m can be obtained, but with limited lifetime due to atmospheric drag. The architecture for SAR antenna consists in a deployable passive plane antenna, with no RF electronics installed on antenna to enable low stowage volume (all electrics instruments are in the satellite body. The stowed size is 0.7 m x 0.7 m x 0. 15 m. The deployed antenna is composed by three panels, each of 0.7 m x 0.7, in such a way to obtain a SAR antenna with an aperture of 4.9m x 0.7 m.

Table 6 resumes the characteristics of the missions above described.

Table 6 Microsatellites SAR missions characteristics

Mission	Application	Mass (kg)	#Satellites	Status
ICEEYE	Maritime	80	18	Launched
NovaSAR	Small SAR demonstrator	400	1	Launched
Compact X-SAR	Compact SAR architecture	100	1	-

2.3 Spacecraft Modularity

The first modular standard for spacecraft design was introduced with the Multimission Modular Spacecraft standard [50], developed by NASA in 1978. This standard was applied for the design of six spacecrafts from 1980 to 1992. Then, in 1997, the IEEE published the IEEE 1451.2-1995 standard for the Transducer Electronic Data Sheets (TEDS) [51]. This standard allows to describe the characteristics and capabilities of the generic modular component. In the early 2000's software architectures for creating modular spacecraft started to appear [52]. In 2003, the IEEE 1355 standard was modified for space applications delivering the SpaceWire standard [53]. In 2005 new ideas for plug-and-play spacecraft using the USB and SpaceWire standards were introduced to create an onboard spacecraft plug-and-play network. This was the beginning of the Space Plug-and-Play Architecture (SPA) [54].

SPA first appears in the literature by name in 2005 at the Responsive Space conference pioneered by AFRL in support of Operational Responsive Space (ORS) mission. This is a complete hardware/software model based on a set of modular conventions to rapid integrate a platform. The first fully SPA spacecraft was PnPSat-1 [54]. The failure of this program yields to the creation of the PnPSat-2 [55]. Over the years, different SPA subnet types have been introduced. The SPA-SpaceWire was first published in 2007 [56]. SPA-Optical was first published in 2010 [57]. SPA-1 based on the I2C standard was also first published in 2010 [58]. SPA-1 was selected for the TrailBlazer cubesat mission [59]. SPA-USB and SPA-SpaceWire were own on the TacSat-3 satellite as an experimental bus technology [60].

In 2010, a SPA training course was developed around CubeSat technologies. Several CubeSats have been developed using SPA [61]. Finally, the AFRL work evolved to a new program called Nanosatellite and Plug-and-play architecture (NAPA) [62], intended to advance the readability of plug-and-play concepts for developing a high-performance CubeSat platform and architecture, referred to as Space Plug-and-play Architecture Research Cubesat-1 (SPARC-1) [63].

2.3.1 SPARC-1 mission

SPARC-1 is a single spacecraft of an intended series of missions that would explore technologies, design approaches, and operations concepts for spacecraft modularity [63]. Figure 9 represents an artistic depiction of SPARC-1. The platform is based on a set of principles that include: i) modularity in hardware and software, with ground support equipment and tools, ii) avionics miniaturization, iii) simplified ground architecture, iv) emphasis on missions based on distributed constellations.

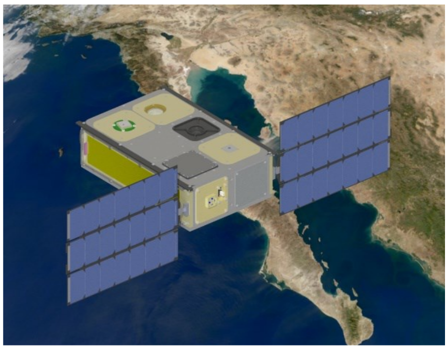

Figure 9 Artistic depiction of SPARC-1 6U CubeSat [63]

Figure 10 shows the satellite bus with the key components.

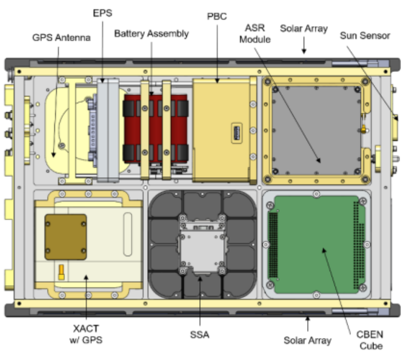

Figure 10 SPARC-1 satellite components [63]

Specifically, SPARC-1 is based on the SUPERNOVA 6U structure modified to support the ASR S-band antennas. The EPS consists of the power supply unit (PSU), the battery pack and the solar array. All three systems were developed by different vendors and then integrated into a cohesive system. The solar array is the High Watts per Kilogram (HaWK) system. The HaWK has three panels of solar arrays per wing and two wings. It has a mass of approximately 276 grams and utilizes Spectrolab solar cells. At beginning of life, it can provide 36 watts at seventy degrees Celsius. Blue Canyon Technologies developed the fleXible Attitude Control Technology (XACT) attitude control system to provide reliable high-performance attitude control, compatible with a variety of CubeSat configurations. The SSA sensor is a Hyperion Technologies IM400 Imaging Star Tracker able to take images of point source objects with a resolution of 88 μrad/pixel.

2.3.2 Modular ADCS review

Though not great in number, some research studies focused on modular ADCS can be found in literature. To the best of author's knowledge, the most prominent work in this sense is [64], where a clear and detailed analysis about modular ADCS systems is given. The focus of this work was on the development of ADCS modules for reconfigurable space systems. A minimum set of modularity requirements is defined to design a module catalogue. This catalogue contains several modules whose combination can generate different ADCS systems able to fulfil requirements for a set of reference missions. Since the number of module combinations is very high, design automation methods are proposed to generate and optimize module catalogues, automatically. Based on this module catalogue, concepts for modular ADCS are defined and then used to develop algorithms for online calibration of sensors and actuators, with a mathematical analysis for their scalability to different platforms. Indeed, the orbit reconfiguration of the modules may cause changing on Center of Mass, Moment of Inertia, mass of the platform, sensor biases and scale factors which must be computed as input to the attitude control algorithms. An elegant discussion about modular ADCS for small satellites is given in [65]. This forerunner work provides an in-depth assessment about the essential philosophy to apply modularity concepts to ADCS. The fundamental idea is that combining many simple instruments is preferable to use one complex and high-cost instrument. A building block approach is used to design the ADCS structure. This structure is based on a bus structured architecture where a basic and simple ADCS configuration can be augmented by using a set of simple instruments according to the requirements dictated by the mission. In [66] a flexible 3D simulation framework is proposed for creating a Virtual Testbed for simulating attitude control systems of modular satellites. The Virtual Testbed comprises all the simulation algorithms for modelling rigid body dynamics, control algorithms and sensor simulations. The simulator is conceived to set a certain scenario for evaluating attitude control performance varying the actuator configuration, sensor uncertainties, orbital perturbations, and the type of control algorithms. The modular Dynacon High Performance Attitude Control (HPAC) system is presented in [67]. Taking advantage of a small number of reusable algorithm modules, the modular HPAC can be applied to various spacecraft missions with very different performance requirements. High-level description of each module making up the HPAC system is given but more in a discursive way. For example, the need of parametrizing algorithm equations for enabling the reusability from mission to mission is highlighted but how the parametrization has been performed is not very clear. Anyway, the work is an excellent starting point for understanding the way in which organising a modular software for ADCS. Plug-and-Play (PnP) concepts for reusable Guidance, Navigation and Control (GNC) systems are introduced and discussed in [68]-[70]. For demonstrating the reusability of PnP ADCS, the software is partitioned in several functional elements. An ADCS Subsystem Controller is the interface between the network and the ADCS dictating the ADCS task to be performed. It comprises software applications that manage subsystem activities. Helper applications (helper apps), instead, are used to translate the component specific information into or out of atomic data elements. Atomic data are data completely abstracted from the type of sensors and actuators. These data are dependent only to the geometry and on the physics of the problem rather than to components and subsystems. In this way, the GNC core algorithms can be abstracted from actual configuration to be reusable. Another interesting work about modular ADCS can be found in [71], which presents a new approach to design and simulate ADCS by exploiting an application-based architecture. The goal is to maximize the possibility to modify software by changing, adding, deleting, or modifying an application without affecting the rest of the software, thereby reducing the test requirements on the system. A comprehensive comparison between traditional ADCS architecture and modular ADCS architecture is also given. While traditional ADCS software is optimized for a specific mission, contained in a single block with specific mode of operations, with rigid definition of mass and inertia properties and hard modifications to hardware/software, the modular ADCS is designed for reuse, split in several elementary applications with generic mode of operations externally defined, ease of modification and adaptation of modules by generic algorithms and external logic control mode.

3. Formation-Flying SAR Mission

The term formation flying SAR (FF-SAR) is used in this thesis to indicate a cluster of satellites flying in a close formation [4]-[8]. Each satellite collects the echoed signal emitted by the transmitter and scattered from the area of interest. These collected echoes are then coherently combined to enhance the overall system performance and the quality of the delivered products. In contrast, FF-SAR system may pose challenging requirements in terms of electrical power, orbit control, communication link, payload synchronization, and formation-flying operations [11]. In this chapter, the fundamental FF-SAR principles are presented. Based on these principles, new working modes and applications are defined, accounting for main technological issues posed by this system. Analyzed FF-SAR scenarios are described to point out how performance requirements impact on system architecture. These scenarios are characterized by different space system architectures involving a specific number of platforms, formation configurations, and payload capabilities.

3.1 Definition and principles

An FF-SAR represents a generalization of the conventional SAR principle [72], and of standard interferometric SAR (InSAR) techniques [73], toward a highly flexible system able to implement a wide range of different working modes. The key concepts are redundant samples and spatial variability. Indeed, when FF-SAR is considered working with a formation of N receivers, the coherent combination of the multiple echoes collected by each receiver can be exploited to enhance the overall performance [4]. When both cross-track/radial and along-track separations are available among the N receivers, the coherent processing approach can be adaptively modified to improve the desired imaging feature to the current scene and to the observation requirements. In addition, the separations among the receivers can be changed during the mission to further improve the system capabilities.

3.2 Applications

Expected FF-SAR techniques allowing for performance improvements with respect to a traditional single-channel monostatic SAR include [5]:

- Signal-to-Noise Ratio (SNR) improvement (up to a factor given by the number of receivers)
- Coherent Resolution Enhancement, CRE (same for the SNR improvement)
- High-Resolution Wide-Swath (HRWS) imaging (e.g., the swathwidth can be extended up to a factor given by the number of receivers without degrading the azimuth resolution)
- 3D Imaging and Tomography, which cannot be achieved by a monostatic SAR in a single-pass fashion
- Ground Moving Target Indication (GMTI), which cannot be implemented by a single-channel monostatic SAR

3.2.1 SNR improvement

SNR improvement deals with the property that the coherent combination of N SAR images, collected by identical receivers flying in close-formation, results in an increased signal power, by a factor of N, without altering noise power. Assuming perfect synchronization and coherent combination with no errors, the resulting FF-SAR working with N receivers can be written as

$$SNR_{FF-SAR} = \sum_{i=1}^{N} SNR^{i}{}_{bistatic} \tag{3.1}$$

If the elements of the formation are close enough, i.e., when the separations are negligible with respect to slant-range of the platform, Eq. (3.1) can be rewritten as

$$SNR_{FF-SAR} = N \cdot SNR_{bistatic} \tag{3.2}$$

Consequently, FF-SAR ensures an SNR improvement up to N times with respect to an equivalent bistatic configuration.

3.2.2 HRWS Imaging

When more than one receiver is available, the PRF of the transmitter can be relaxed to values that are significantly lower than the Doppler bandwidth of the illuminated scene. This allows FF-SAR system to increase the swath width which can be observed without range ambiguities, i.e., to implement high-resolution wide-swath (HWRS) techniques. To estimate unambiguous swath width one can use the chronogram, which shows ground-range values in relation to PRF. In Figure 11, the solid lines are the ground range values affected by range ambiguities. The dashed lines, instead, represent ground range values affected by nadir echoes. Hence, for each PRF value, the unambiguous swath is the interval between the intersection of solid and dashed lines.

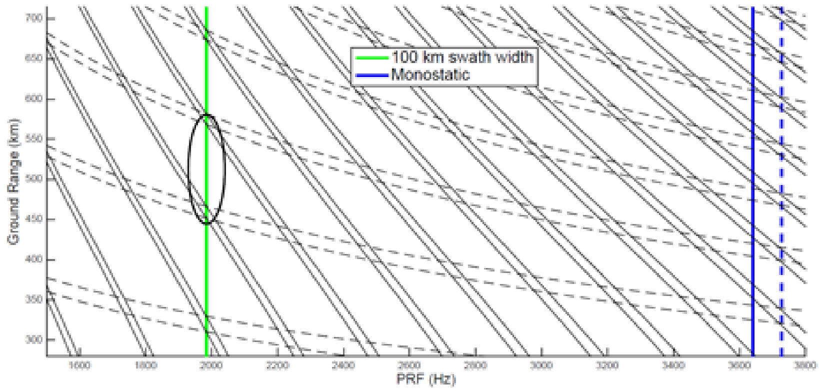

Figure 11 Chronogram. The solid black lines refer to ambiguities in range. The dotted lines, on the other hand, represent nadir returns. The blue line refers to the Nyquist PRF, while the green line refers to a halved PRF, at which a greater swath can be obtained.

As one can see from Figure 11, high values of PRF correspond to small unambiguous swaths, while, decreasing the PRF, the achievable swathwidth can be enlarged. At the same time, unambiguous reconstruction of the Doppler history is achieved in processing combining the data collected by each receiver by using beamforming algorithms for HRWS imaging. Beamforming algorithms can be applied both in the frequency and time domain. The main differences between the two domains are computational load, applicability to different geometry and configurations, and the position in the DSAR processing chain. Indeed, in the time domain the beamforming must be performed together with SAR focusing while in the frequency domain the beamforming step precedes the focusing step.

Time Domain

Time domain processing is relatively easy to implement and can be applied to very general multistatic configurations. This means that no specific assumption about platforms' motion (e.g., straight path, constant velocity) and bistatic geometry (e.g., parallel tracks) is necessary. Moreover, no specific requirement concerning geometrical features of the observed scene (e.g., flat Earth) must be met. Any absolute and relative motion and scene geometry can be accommodated if they are known with sufficient accuracy. The most important drawback is the huge computational burden. This is because pixel-by-pixel correlations and operations must be carried out. Nonetheless, strategies for reducing the computational load can be applied. For instance, performance parameters depending on DSAR point target response can be estimated focusing only, relatively small, sub portions of the raw image (e.g., tens of pixels by tens of pixels wide). An example of time domain algorithm for the cancellation of the ambiguities in azimuth resulting from the use of an operational PRF lower than the Doppler band value is reported in [74] and briefly described herein.

Considering an FF-SAR system of N receivers, for each pair of bistatic couples N focused bistatic images can be obtained. These images are co-registered and geo-referenced on a single common grid. For each pixel of the grid, the following parameters are assumed to be known: (i) position and velocity vectors of the transmitter, (ii) position of the receiver, (iii) position of the pixel, with vectors calculated in the Earth-Centered Earth-Fixed (ECEF) reference system. From the known parameters it is possible to calculate the position of the ambiguities in azimuth generated by the target imposing that: (1) the position of the ambiguity is on the surface of the Earth; (2) the position of the ambiguities depends on the PRF; (3) the distance between the transmitter and the ambiguity is equal to the slant range. The beamforming weights of each receiver related to the target can be calculated by imposing 0 in the position of ambiguities and 1 in the position of the target. These weights can be used to build "partial" images (because they refer to the single target) which can then be coherently combined to obtain the final image.

Frequency Domain

Beamforming for HRWS imaging can be also applied in the frequency domain. The algorithm is faster, but the applicability is limited to relatively close formations. In a HRWS scenario, the PRF is lower than the Doppler bandwidth of the scene, so bistatic data are aliased. The term reconstruction is thus used as the method to enable for the coherent combination of these aliased data into an unambiguous SAR signal. The reconstruction consists of linear filters that are applied to the aliased spectra of the bistatic signals. The definition of the linear filters derives from the generalization of the sampling theorem, according to which a band-limited signal is uniquely determined in terms of the samples of the responses of N linear systems working at 1/N of the Nyquist frequency. The resulting signal from the reconstruction features a sampling frequency which is multiplied by a factor of K with respect to Tx PRF. For K = N, all the degrees of freedom of the implemented distributed SAR are used to increase the PRF or, equivalently, to suppress N azimuth ambiguities affecting the individual bistatic data. This is a specific class of reconstruction methods thoroughly analyzed in [75]-[77], [80].

3.2.3 Coherent Resolution Enhancement (CRE)

Coherent resolution enhancement is an FF-SAR technique which can be used to enhance the resolution with respect to a monostatic SAR working with the same parameters. The technique is based on coherent combination of data collected by spatially separated receivers. The idea is that the synthetic aperture, either monostatic or bistatic, represented by a single receiver of the formation, is completed by the physical array realized by all the receivers in the formation. Azimuth resolution can be thus improved if the half-power beamwidth of the physical array in the azimuth direction is narrower than that of the synthetic aperture. Beamforming algorithms can be applied to achieve azimuth resolution enhancement. The same idea can be exploited in the cross-track/vertical plane to improve ground range resolution. Specifically, resolution enhancement in ground range is a mixture of slant range resolution with angular resolution, and this combination can generate conceptual errors if interpreted as a pure beamforming. Therefore, range resolution enhancement is typically presented and analysed in the range frequency domain, where it is referred to as super-resolution. Super-resolution in range relies on the coherence combination of the range spectra of the data collected by each receiver. Those spectra can be assumed to show spectral shifts depending on the effective baselines. Hence the relevant combination increases the overall total range bandwidth thus enhancing the resolution. Specifically, if the spectra of the received signals overlap, they can be combined by an appropriate set of weight functions to obtain a new spectrum with a wider band. In this way, by operating the inverse Fourier transform of the combined spectrum, an image with a better resolution in range is obtained. A similar result can also be obtained for small separations between the satellites but using several transmitters operating on a suitably shifted frequency band. To operate the above resolution increase technique, the algorithm proposed in [78] can be used. In a bistatic configuration the shift in frequency between the spectra acquired by the two receivers can be expressed as

$$\Delta f = \frac{cB_{\perp}}{2\lambda R \tan\theta} \tag{3.3}$$

where $B_{\perp}$ represents the perpendicular baseline, R is the platform-target distance, λ is the wavelength, θ is the incidence angle, c is the speed of light. The previous equation shows that when the baseline is lower than the critical baseline value, there is a certain amount of overlap between the spectra, which can be exploited to combine them. In an FF-SAR system with N receivers, the combination operation can be applied to each pair of images, as shown in Figure 12. In particular, the spectrum obtained from the combination of the first and second image is combined with the spectrum of the third image and so on, until the final spectrum is obtained as a combination of the N-th spectrum of the image acquired by the rightmost receiver in the formation with the last combined spectrum obtained in the chain of successive combinations (Figure 13).

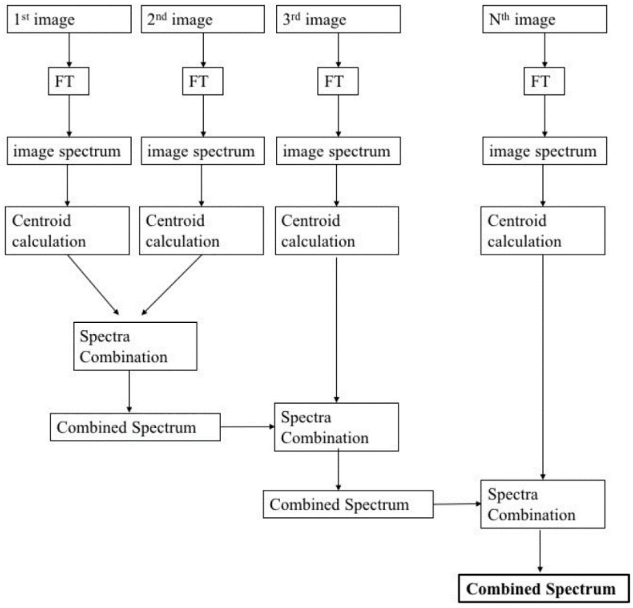

Figure 12 Scheme of the CRE algorithm

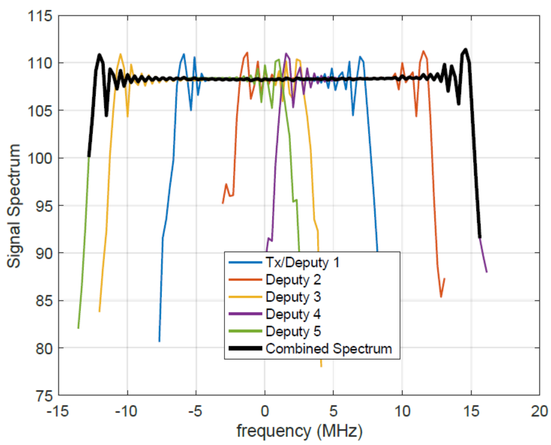

Figure 13 Example of 5 spectra combination in one spectrum with wider band

3.2.4 3D Imaging

As far as 3D imaging is concerned, cross-track interferometry (XTI) is the standard technique used to generate three-dimensional radar images. The vertical information associated to each pixel is derived from phase differences of two different images of the same region. On the other hand, the vertical detail within the single pixel cannot be evaluated by cross-track interferometry, whereas it can be obtained by means of 3D imaging techniques derived from the principle of SAR tomography. This technique relies on several receivers covering the target scene with slightly different observation geometries. Vertical structures are thus identified using a vertical aperture synthesis and following array theory, i.e., again, by digital beamforming. The technique poses requirements in terms of total effective baseline that are very similar to those of coherent range resolution improvement. FF-SAR can also achieve GMTI capabilities. This is because the satellite formation realizing the considered FF-SAR system can be interpreted as a multi-channel receiver composed of more than two Rx channels (at least 3). This means that suitable combinations of ATI and Displaced Phase Center Antenna (DPCA) techniques can be exploited to gain advantage of their complementary characteristics while simultaneously solving the major related drawbacks. Indeed, on one side, ATI allows removing false moving-target detections caused by the presence in the scene of strong stationary scatterers (which may be characterized by a residual magnitude in the GMTI map even after DPCA is applied). On the other side, DPCA allows neglecting in the moving-target search those regions in the GMTI map, located in the shadow of strong scatterers, which can cause false moving-target detections if only ATI is used (since the ATI phase would be dominated by random noise in absence of moving targets). With more detail, a 3-Rx configuration can ensure satisfying performance in terms of moving-target detection and velocity estimation provided that the along-track baseline between the Rx channels is not too large (e.g., in the interval 100 m - 200 m). If more receivers are available, operations constraints dealing with PRF selection [6], DPCA blind velocities, and wrapped ambiguities of ATI phase are relaxed notably.

3.2.5 Multi-purpose

Concluding this section, the term multi-purpose is referred to FF-SAR applications able to accomplish different goals simultaneously (i.e., more than one application at the same time and over the same areas) exploiting system redundancy. Assuming a formation composed of N platforms, such a system has got N degrees of freedom which can be exploited. So, M degrees of freedom can be used to enable an application and the remaining N-M degrees of freedom can be exploited for a different one. As an example, if the selected PRF is about M times smaller than that required to correctly sample the Doppler bandwidth of the scene, residual redundancy is available to improve SNR or equivalently to reduce the required Tx power.

Using M degrees of freedom, applying the reconstruction algorithm, as detailed in section 3.2.2, the PRF can be reduced to the minimum value of

$$PRF_{\min} \geq \frac{B_D}{M} \tag{3.4}$$

This PRF value must be refined to avoid echoes coming in the nadir direction and maximize the uniformity of the distribution of samples, as detailed in [6]. Since not all degrees of freedom are used for PRF reduction, the residual redundancy can be exploited to improve the SNR. As demonstrated in [80], by recombining the signals with an HRWS technique, it is possible to obtain, simultaneously, an increase in the SNR, compared to a monostatic configuration operating with the same parameters, equal to

$$SNR_{DSAR} = N \cdot SNR_{MONO} \tag{3.5}$$

Thus, a DSAR system with N receivers can obtain the same azimuth resolution as an equivalent monostatic system, but at the same time

- obtain a swath larger by a factor equal to the number of degrees of freedom used
- work at a lower operating PRF
- increase the signal-to-noise ratio by a factor of N

3.3 Design issues

Despite these capabilities, the practical realization of FF-SAR system must deal with a number of technological challenges, mainly related to the non-traditional configurations in which the co-working platforms must operate [5], [11]. In details,

- satellite formation flying
- multistatic SAR synchronization
- multistatic SAR processing

Satellite formation flying, intended as the problem of relative motion design and relative navigation, as well as autonomous formation maintenance, reconfiguration and control, may involve different issues, for example, to avoid collision risk among the satellites, particularly when the formation includes many members operating with short separations [81]-[82]. In addition, the increased propulsive demand, and operational efforts to acquire formation geometry after launch, as well as any possible reconfigurations during the mission, must be carefully included in the formation design.

At payload level, different levels of multistatic SAR synchronization [25] are needed to enable suitable coherent combination of signal collected by different platforms. Indeed, for the proper working of FF-SAR operations, one must consider techniques for either spatial, time and clock synchronization. Specifically, spatial synchronization is needed to ensure all the receiving antennas cover the ground area illuminated by transmitter; time synchronization, instead, deals with the need to know with sufficient precision the time instants in which echoes from the scene are expected to reach Rx antenna; clock synchronization is targeted to make sure that all the receivers remain coherent for the period required to get useful data from the scene.

Last but not least, multistatic SAR processing [76] that is digital beamforming to generate higher performance images/products from the low performance signals, collected by each receiver separately, poses challenges when real-world observation conditions and scenes are met [77].

3.4 System Satellite Architecture

Each working mode described in the former paragraph poses specific requirements on the space architecture of the satellite system. Indeed, the geometry of the formation is dictated by the application to be performed while the number of platforms is given by the analysis of imaging performance.

3.4.1 Formation configurations

To have the same SNR for each receiver, *SNR improvement* requires a close formation in which the separations between the elements of the formation must be minimized. This ensures the same SNR for each receiver and the applicability of Eq.(3.1). For example, for X-Band system operating in Low-Earth Orbit (LEO), the total dimension of the cluster should be less than 500 m. Finally, the SNR application need the proper coherent combination of signals gathered by the available platforms by using specific processing techniques.

HRWS imaging must be tested under dominant along-track separations among the satellites. The cluster dimension should be short enough to properly combine the acquired samples. Even though a linear distribution may lead to a better multi-static SAR processing, the formation geometry should not be purely linear, as a short radial/cross track baseline (of the order of a few tens of meters) is needed to partially decouple collision risk from along-track design. Specifically, a safety tube is established around the velocity vector of each satellite [81], so that the satellites are allowed to drift in along-track direction. In this way, the formation falls within the “safe-ellipse” category.

Safe ellipses represent a generalization of the helix concept. As in the helix case, they exploit dynamics in all the relative motion coordinates (radial, along-track, cross-track), and they allow keeping a minimum separation in the radial/cross-track plane (hence the definition of “safe” ellipses), which relaxes formation control requirements in the along-track direction. The along-track/cross-track projection of the trajectory is in general an ellipse (not a line, as in the helix case), and the separation, in general, is never purely radial (as it happens in the helix case), which means that the deputy is never above/below the chief. Given a minimum distance to achieve in the radial/cross-track plane, safe ellipses can be optimized in view of different aims, such as minimizing the range variation, or obtaining a given cross-track separation when the along-track coordinate is nullified.

The application of *CRE* requires dominant cross-track and along-track baselines, with a cluster dimension >1km. A possible formation that enables these applications can be obtained from the requested maximum effective baseline. Natural formation dynamics is such that effective baseline oscillates at orbital frequency, so the “optimal” values can be obtained only in two positions along the orbit. However, relative trajectories can be designed so that effective baseline requirements are made equal to the amplitude of the oscillations.

Dominant perpendicular baselines, with a cluster dimension >1km, are required for *3D* imaging/*tomography* applications. The formation must realize a so-called minimum redundancy array [82],[83]. Such configurations are very useful for FF-SAR tomography because allow one to emulate a formation of M, equally spaced, receivers using just N < M receivers characterized by not uniform separations. For example, a formation working with three-receiver is equivalent to an equally spaced formation of four receivers.

Finally, *GMTI applications* can be performed using the same formation as for HRWS imaging. Table 7 lists the requirements posed by each FF-SAR application.

Table 7 Formation requirements dictated by FF-SAR applications for an X-Band system operating in LEO in Stripmap mode with a resolution of 3 meters

Application	**Formation requirements**
SNR improvement	Close formation (cluster dimension < 500 m)
HRWS imaging	Dominant along-track baselines (cluster dimension in along-track < 1 km)
CRE	Dominant cross-track/along-track baselines (cluster dimension >1km)
3D imaging/tomography	Dominant perpendicular baselines (perpendicular baselines >1km)
GMTI	Dominant along-track baselines (cluster dimension in along-track < 1 km

3.4.2 Definition of the minimum number of platforms

SNR improvement and HRWS imaging techniques allow to estimate the minimum number of satellites needed to ensure the required imaging performance, in terms of achievable SNR, image resolution, and swath size. A formation conceived to include the minimum number of platforms enable the implementation of all the FF-SAR techniques described above. Performance clearly improves as the number of used satellites increases. In Section 3.2.1 it was seen that, in the case of perfect synchronization and coherent combination between the different receivers, the resulting SNR can be expressed as

$$SNR_{FF-SAR} = N \cdot SNR_{bistatic} \tag{3.6}$$

Consequently, the number of platforms can be set to match the required SNR starting from the performance of bistatic configuration. This will be described in detail in Section 3.5.2.

The HRWS application can be exploited to obtain a greater unambiguous swath. In fact, by using the timing diagram, described in paragraph 3.2.2, it is possible to estimate the behaviour of the imaging performance as the PRF varies. As stated before, decreasing the PRF leads to enlargement of the achievable swath width. The reduction of the PRF implies the need for an appropriate reconstruction of the ambiguous signal in azimuth, and consequently, the HRWS application has a direct impact not only on the type of data processing to be implemented, but also on the number of platforms to be used. In fact, if the PRF is halved, at least 2 receivers will be required. If the PRF is reduced to one third of the Doppler band, at least 3 passive platforms will be required to reconstruct an unambiguous signal.

3.5 Analyzed FF-SAR scenarios

The FF-SAR concept has been tested under multiple satellite configurations. Specifically, three scenarios have been considered including different satellite system architectures, imaging requirements, FF-SAR working modes, and number of platforms. This enables to highlight how mission characteristics and requirements impact on formation and platform design.

In particular, the first scenario has been selected to demonstrate FF-SAR features, as HRWS, CRE, and SAR tomography, by designing a formation of three micro-satellites, in which a fully a monostatic SAR platform flies in formation with two Receiving (Rx) only satellites. The design is targeted to define suitable formation characteristics to match the imaging requirements and to enhance monostatic performance. The second scenario aims to define and select a suitable configuration for implementing single-pass multi-baseline SAR interferometry to achieve better surface changes estimation. The space system has been designed to ensure daily revisit time and global coverage by working with a single-plane constellation of eight evenly spaced formations, each involving a fully active configuration with four co-flying monostatic SAR platforms. Finally, the third scenario has been selected to demonstrate the capability of FF-SAR system to match the SAR performances of an equivalent monostatic SAR platform used as illuminator of opportunity.

Scenario 1

The first scenario includes an FF-SAR system based on a fully active Transmitting-Receiving (Tx/Rx) microsatellite, i.e., a monostatic SAR platform, flying in formation with two

Receiving (Rx) only microsatellites [5]. The monostatic platform has been designed to achieve 8m x 8m resolution on ground, with -24 dB Noise Equivalent Sigma Zero (NESZ), from an orbit altitude of 550 km, and 20° inclination. Imaging and relevant parameters for the Tx/Rx satellite design are listed in Table 8. FF-SAR system must ensure the enhancement of the monostatic performance exploiting a combination of DSAR techniques like SNR enhancement, HRWS, CRE, 3D imaging, but with limited SAR duty cycle per orbit (a few minutes), limited lifetime (two years), limited revisit time and coverage (no ground-track control).

Table 8 Imaging and relevant parameters for Tx/Rx design

	Parameter	**Value**
Imaging Requirements	Resolution	8m x 8m
	NESZ	-24 dB
Tx/Rx SAR parameter	Antenna Size	0.7 x 4.9 m
	Chirp Bandwidth	up to 100 MHz
	PRF	3.5 kHz
	Incidence Angle	30°
	Swath Width	35 km
	Peak Power	2 kW
	Average Power	136 W
	Data Rate	200 Mbps
	Orbit Duty Cycle	5%

Specifically, three working modes have been simulated to demonstrate FF-SAR features. The main characteristics of each working mode can be summarized as

Mode 1

- 3 satellites with dominant along-track separations (up to 200m)
- 8 m x 4 m resolution
- Ambiguities suppressed by digital beamforming in azimuth
- SNR improvement

Mode 2

- 3 satellites with dominant cross-track/ vertical separations (up to 1km)

- 6 m x 6 m ground-range resolution
- CRE in range
- SNR improvement

Mode 3

- Same working parameters as in Table 1
- 8 m x 8 m resolution
- 3D imaging
- GMTI

Important examples are available in the literature for the design and realization of a compact monostatic SAR compatible to microsatellite operations [49]. SAR design parameters are selected to meet the above introduced imaging requirements, according to the limitations set by the radar equation. From the point of view of the antenna design, with reference to already flown SAR missions [154], a passive planar antenna is taken as reference herein. It is composed by 7 panels, each 0.7 m x 0.7 m wide, which realize a rectangular aperture antenna with a maximum length of 4.9 m and a total mass of about 30 kg. With reference to the radar Radio Frequency (RF) unit when non-space components are selected as in [154], very compact solutions can be realized keeping the required mass below 15 kg.

Working mode 1

Mode 1 is aimed at applications requiring along-track observation geometries, such as HRWS imaging. All the satellites are assumed to work with 3 among the 7 available panels, thus realizing a shorter antenna of 2.1 m length. This leads to a Doppler bandwidth of 6.7 kHz. If the Pulse Repetition Frequency (PRF) is kept at 3.5 kHz, azimuth ambiguities arise but a wider swath can be covered without range ambiguities. HRWS imaging is thus enabled if the azimuth ambiguities can be suppressed. This can be achieved by digital beamforming combining the images collected by the three formation flying sensors. In this mode the Tx is asked to transmit about 3 kW peak power, which corresponds to more than 200 W average power. All the other budgets and parameters of Table 8 are confirmed in Mode 1. Figure 14 shows a simulation illustrating the effect of FF-SAR imaging through digital beamforming. If one considers the receivers as isolated items (Figure 14, left) azimuth ambiguities are as strong as the target response. Nonetheless, suitable coherent combination of the signal collected by all the available three receivers can be performed to effectively suppress the ambiguous contributions (Figure 14, right).

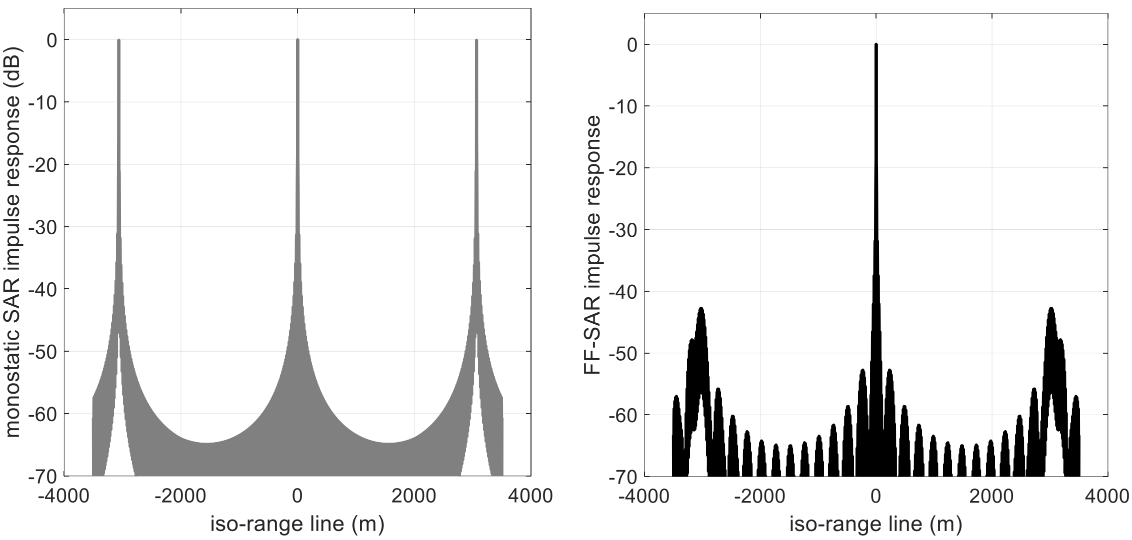

Figure 14 Simulated response from a point target located at the origin of an iso-range line: (left) single receiver response with strong azimuth ambiguities and (right) FF-SAR response after digital beamforming with suppressed azimuth ambiguities.

For what concerns formation design, a quasi-linear formation (described in Section 3.4.1) is assumed, in which all the satellites are displaced in the along-track direction. The formation includes 3 satellites: one transmitter/receiver, considered as the chief of the formation, and two receiving-only systems, assumed as deputies. A minimum distance of 20 m in the radial/cross-track plane is guaranteed for any considered pair of satellites, and the designed formation falls within the "safe ellipses" category (see Section 3.4.1). It is assumed that the chief satellite orbit is an almost circular orbit at 550 km attitude, an inclination equal to 20°, 0.001 eccentricity, argument of perigee at 45°, initial right ascension of the ascending node and true anomaly equal to zero (these numbers refer to initial mean orbit parameters). The same ballistic coefficient has been assumed for all the satellites. Table 9 lists the initial differences in mean orbit parameters for the two deputies.

Table 9 Initial differences in mean orbit parameters for the two deputies in Mode 1

Parameter	Deputy 1	Deputy 2
Δa (km)	0	0
Δe	$4.10 \cdot 10^{-6}$	-0.234
Δi (°)	0	0
$\Delta \Omega$ (°)	$-9.67 \cdot 10^{-4}$	$-1.93 \cdot 10^{-3}$
$\Delta \omega$ (°)	0.234	0.466
$\Delta \upsilon$ (°)	-0.234	-0.465

Figure 15 reports the computed 3D trajectories with respect to the chief, and their projections on the coordinate planes. The achieved along-track baseline is depicted in Figure 16.

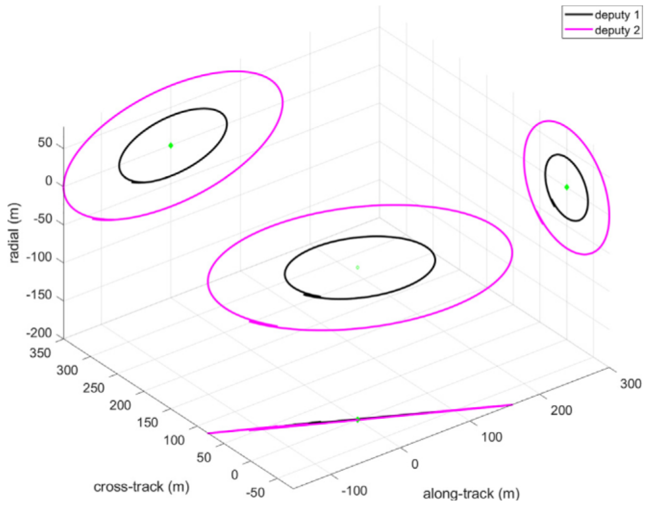

Figure 15 3D trajectories in the chief HRF and projections on the coordinate planes (one orbit)

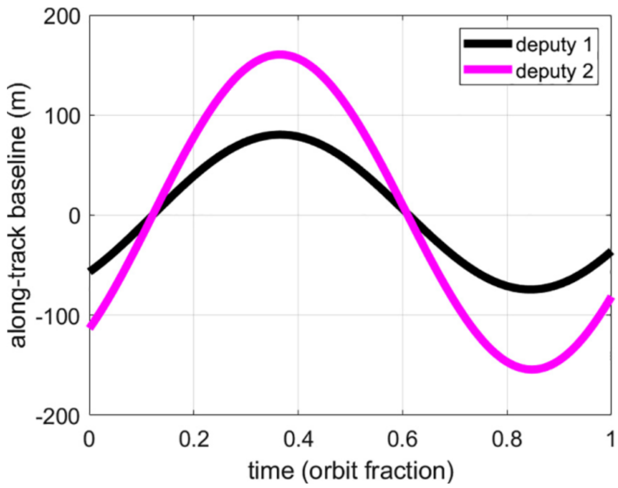

Figure 16 Along-track dynamic as a function of time in the considered formation.

Working mode 2

Mode 2 is characterized by relevant cross-track baselines. Hence, this configuration shall be used to demonstrate improvement in the ground-range resolution, by means of CRE technique. The system can switch from Mode 1 to Mode 2 assuming all the 7 panels working in this case, so the signal is not ambiguous in azimuth and performing a formation flying maneuver to realize a longer cross-track separation. The required Tx peak power is 1.6 kW, that corresponds to 116 W average power during Tx operation. As described in Section 3.2.3, the working principle of CRE is that the relative positions among the available receivers realize a physical array so an equivalent antenna [84]. The pattern of this antenna can be steered by beamforming towards any image pixel. Ground range resolution improves because, owing to the long cross-track separation, the peak of the array pattern is narrower than the impulse response width of the single receiver which depends on the Tx signal bandwidth. A cross-track separation can be thus interpreted as a widening of signal bandwidth [85]

$$\Delta W = \frac{c \Delta B_{\perp}}{2 \lambda R \tan \theta} \tag{3.7}$$

where R is the slant range, λ is Tx signal wavelength, c is the speed of light, θ is the incidence angle, and $B_{\perp}$ is the effective baseline, that is the maximum separation in the direction normal to the line-of-sight between two receivers in the formation. According to this model the ground range resolution resulting from FF-SAR processing is

$$\Delta R_g = \chi_\omega \frac{c}{2(W + \Delta W)\sin\theta} \tag{3.8}$$

where χ_ω is a factor depending on the adopted weighting function (i.e., 0.886 for a rectangular window). Starting from a transmitter working with 33 MHz signal bandwidth at 30° incidence angle (8 m ground range resolution), Eqs. (3.7)-(3.8) can be inverted to compute the effective baseline able to guarantee the desired ground range resolution. An effective baseline of about 1.5 km must be used to achieve less than 6 m ground range resolution. Table 10 reports the initial differences in mean orbit parameters for the two deputies.

Table 10 Initial differences in mean orbit parameters for the 2 deputies in Mode 2

Parameter	**Deputy 1**	**Deputy 2**
Δa (km)	0	0
Δe	$4.11 \cdot 10^{-6}$	$-4.09 \cdot 10^{-6}$
Δi (°)	0	0
$\Delta \Omega$ (°)	$-2.79 \cdot 10^{-2}$	$-2.23 \cdot 10^{-3}$
$\Delta \omega$ (°)	0.257	0.254
$\Delta \upsilon$ (°)	−0.231	0.233

Figure 17 depicts the resulting 3D relative trajectories in the HRF and their projections. The figure shows how the cross-track oscillation is exploited to generate the required effective baseline. For the sake of clarity, different scales are used for the different axes.

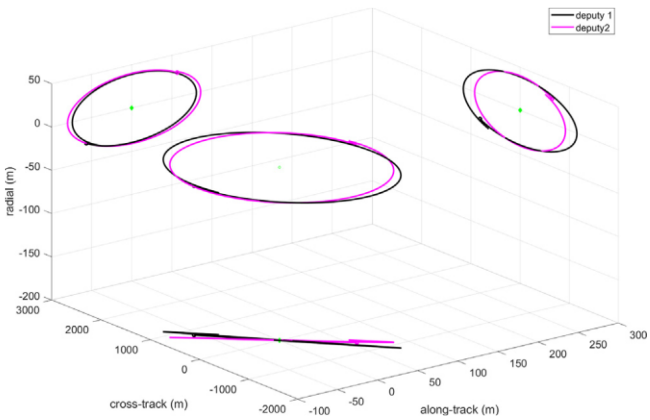

Figure 17 3D trajectories in the chief HRF and projections on the coordinate planes

Figure 18 shows the effective baselines for the two deputies.

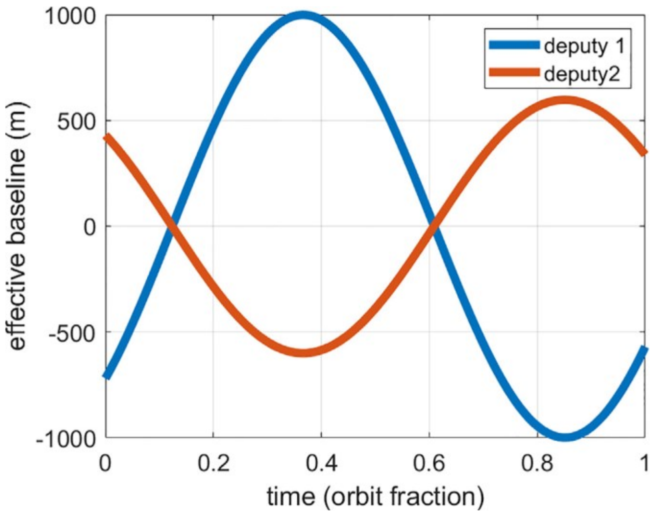

Figure 18 Effective baselines as a function of time

CRE by the designed formation is again verified using a simulation. Figure 19 shows the impulse response along an iso-Doppler line (ground range direction) for the Tx/Rx satellite of the formation (monostatic) and for the result of FF-SAR processing, considering the maximum cross-track baseline along the orbit. As expected, the result of the coherent combination of the signals collected by the available three receivers shows a ground range resolution which is better than 6 m, together with weaker side-lobes.

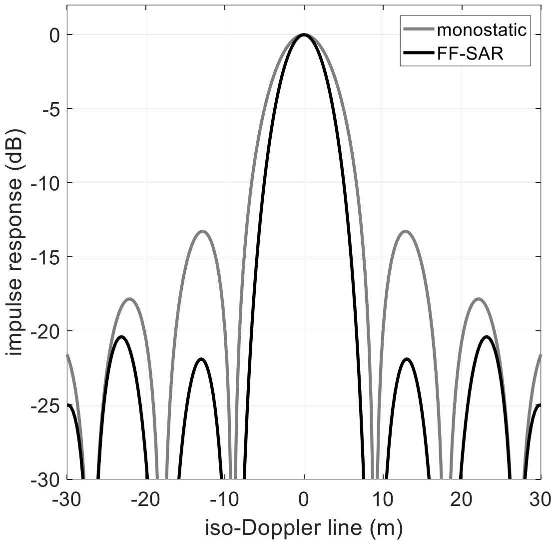

Figure 19 Impulse response along the ground range direction for a monostatic SAR and for the FF-SAR working with large cross-track separation.

Working mode 3

Mode 3 assumes that the monostatic SAR image of the Tx/Rx satellite and the two bistatic SAR images are coherently combined for SAR tomography [82], [86] or using SAR GMTI techniques, depending on the available baseline components. The discussion is herein limited to SAR tomography only. The goal of SAR tomography is to process multi-baseline acquisitions to calculate the complex reflectivity function of a generic image pixel in the elevation direction, that is in the direction normal to the line-of-sight. Depending on the observed objects this reconstruction enables either for volume scattering analysis or for solving the problem of layover affecting SAR images [82]. The computation of the reflectivity function, $\boldsymbol{\gamma}$, can be discretized for each pixel value as

$$\mathbf{g} = A\boldsymbol{\gamma} \tag{3.9}$$

where $\mathbf{g}$ is the measurement vector including, for the current pixel, the N values of single-look complex images collected by each receiver, and A is the so-called steering matrix depending on the relative positions among the receivers. The problem of inversion of Eq. (3.9) is in general not trivial. The easiest approach to the inversion is by beamforming, that is the estimated complex reflectivity function is

$$\hat{\boldsymbol{\gamma}}_{BF} = A^H \mathbf{g} \tag{3.10}$$

where the superscript H indicates the Hermitian matrix or conjugate transpose. The derived $\hat{\boldsymbol{\gamma}}_{BF}$ is used herein to evaluate the performance of the designed FF-SAR working with 3 receivers. Starting from the formation used in mode 2, a deputy can be maneuvered to lead to the configuration of Table 11.

Table 11 Initial differences in mean orbit parameters for the 2 deputies in Mode 3

Parameter	**Deputy 1**	**Deputy 2**
Δa (km)	0	0
Δe	$4.11 \cdot 10^{-6}$	$-2.05 \cdot 10^{-6}$
Δi (°)	0	0
$\Delta \Omega$ (°)	$-2.79 \cdot 10^{-2}$	$1.17 \cdot 10^{-2}$
$\Delta \omega$ (°)	0.257	−0.132
$\Delta \upsilon$ (°)	−0.231	0.116

Figure 20 illustrates an example of tomographic reconstruction considering the maximum available separations along the orbit. The complex reflectivity function was simulated as two-point targets located at -60 m and -20 m along the elevation direction.

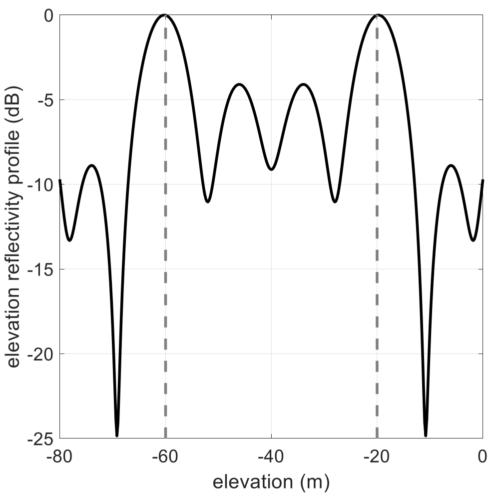

Figure 20 Example of FF-SAR tomography applied to 3 receivers working with dominant cross-track separation in a minimum redundancy array configuration. Beamforming used to compute the complex reflectivity profile for a scene including two-point targets located at -60 m and -20 m along the elevation direction.

3.5.1 Scenario 2

The second scenario includes a satellite system for enabling single-pass multi-baseline interferometry. In this case, the satellite system shall guarantee:

- SAR images with a resolution better than 1 m
- High frequency of observation, i.e., at least a daily revisit of the area is required
- Accuracy of displacements measurements of the order of 1 mm

The space segment design is, hereinafter, conceived to provide an unambiguous swathwidth of 30-50 km (typical values of Stripmap mode in X-band) with a resolution of 1 meter (i.e., as for high-resolution spotlight products). Since these values are not enabled by a monolithic configuration, a formation of platforms will be properly designed to meet both resolution and power consumption requirements. The number of formations and their dispositions in the orbital plane is stated by the revisit time and interferometric performance. In fact, the requirement of daily revisit time is beyond the capability of the spaceborne missions which are currently operating. Indeed, the single formation of satellites in LEO orbit passes over the same target on ground after several to many days. Consequently, a constellation of formations will be proposed, and their phasing angle will be defined to revisit the same area within 24 hours. In such a contest, the global coverage condition is assumed. A constellation of formations enables also the single-pass interferometry, which is strongly related to the requirement on the displacement accuracy of 1 mm. From the point of view of the space segment, the need for single-pass interferometry along with the requirements of the revisit time and resolution implies the design of a constellation of formations, in which, at first, the orbital parameters and the number of components of the constellation are defined by the revisit time requirement. Then, the number of the platforms in each formation is given by the analysis of imaging performance (resolution vs swath) as described in Section 3.4.2, and, finally, the number of formations is doubled to guarantee two single-pass images at each acquisition.

Constellation design

The design of the constellation, in terms of number of orbital planes, their distribution along the equator and the number of satellites per plane, is strongly dependent on the requirement of revisit time. Usually, if a revisit frequency lower than 12 hours is desired, more than 1 plane is required. On the contrary, a single plane configuration enables revisit time larger than 12 hours, even if the orbit parameters shall be properly selected to satisfy the coverage requirements. Hence, the requirement of daily revisit time is fulfilled by a single-plane constellation. The parameters of the orbit have been selected to enable the global coverage. The number of constellation components in the plane, instead, have been defined to achieve a revisit time less than 24 hours is defined. Specifically, a single plane constellation composed of 8 formations is proposed. The formations shall be evenly spaced along the orbit with a phasing angle of 360°/8 (see Figure 21).

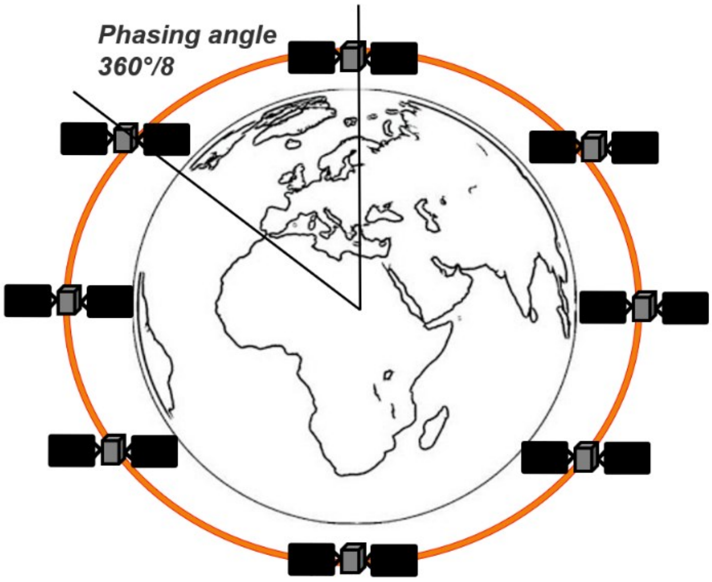

Figure 21 Single-plane constellation of 8 evenly spaced formations

Formation design

In the previous section, a constellation composed of 8 evenly spaced formations have been proposed to meet the requirement of the daily revisit time. In this section, the formation design with the main driver of achieving 1 meter of resolution is described. Such design is carried out as trade-off between power requirement, width of unambiguous swath and number of platforms. The inputs listed in Table 12 have been assumed.

Table 12 Design parameters

Parameter	Value
Antenna Width	1 m
Antenna Length	2 m
Altitude	528 km
Chirp Duration	37 μs
Incidence Angle Range	15°- 45°
Wavelength	3.1 cm
Pixel Area	1m x 1m
Noise Temperature	300 K
Noise Figure	0.5 dB
NESZ	-18 dB

Referring to the input in Table 12, the timing diagram of Figure 22 can be obtained where the red line corresponds to the Nyquist frequency which guarantees a proper signal sampling of the signal. At such PRF value, the unambiguous swathwidth is of the order of 15 km at far range. As mentioned in Section 3, FF-SAR enables wide swath width together with unambiguous sampling of the Doppler bandwidth, which is recovered by Digital Beamforming. Figure 22 clearly shows that halving the PRF with respect to the Nyquist frequency, the extent of unambiguous swath is strongly widened, varying from about 50 km at near range to 30 km at far range.

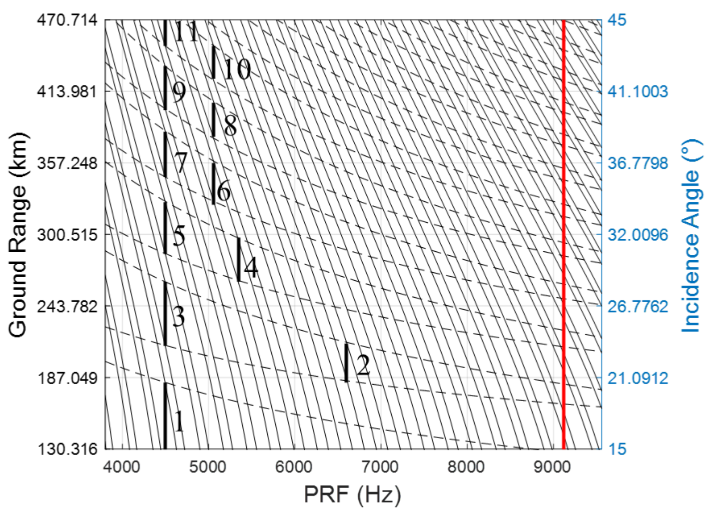

Figure 22 Timing Diagram for Scenario 2

From the point of view of space segment design, the exploitation of DSAR potentialities for PRF reduction implies the definition of the number of platforms of the formation (see Section 3.4.2). In details, ideally if the PRF is halved, to proper recover the Doppler bandwidth the reconstruction algorithm requires as input the signals gathered by 2 platforms. However, power considerations have also been included. One of the key SAR parameters that dictates the transmitter peak power is the Noise Equivalent Sigma Zero (NESZ). NESZ is defined as the backscattering coefficient, σ_0, for which the signal is equivalent to noise. Therefore, it determines the minimum target cross section whose signal is distinguishable from noise, i.e., detectable by the SAR system. The equation for NESZ is

$$NESZ = \frac{(4\pi)^3 R_{Tx}{}^2 R_{Rx}{}^2 k_B T_n B_n F_n}{N \cdot (CPI \cdot PRF) \cdot (\tau_p B) \cdot P_{Tx} G_{Tx} \Delta A \lambda G_{Rx}} \tag{3.11}$$

where each term is defined in *Table 13* with the correspondent values.

Table 13 Description of symbols in Eq.3.11

Symbol	**Parameter description**	**Value**
CPI	coherent processing interval	-
PRF	pulse repetition frequency	4.5 Hz (blu) 5.1 Hz (verde) 5.4 Hz (magenta)
τ_P	pulse length	30 μs
B	signal bandwidth	-
P_{Tx}	trasmitter peak power	750 W
G_{Tx}	trasmitter antenna gain	38.9 dB
R_{Tx}	range from trasmitter to target *(far range)*	535 km
ΔA	pixel area	9 m^2
λ	radar wavelength	3.1 cm
k_B	Boltzmann's constant	$1.38 \cdot 10^{-23}$ K · J^{-1}
T_n	Noise temperature	600 K
B_n	Noise bandwidth	-
F_n	Noise figure	0.5 dB

The Coherent Processing Interval (CPI) can be computed as

$$CPI = \frac{2 \cdot R_{Tx} \cdot \tan\left(\frac{0.886\lambda}{L_A}\right)}{v_{sat}} \tag{3.12}$$

where L_A is the length of the antenna along the azimuth direction, while v_{sat} represents platform velocity. In details, a monolithic system working at the Nyquist frequency and input parameters of Table 12 requires about 5.1 kW of peak power, estimated with N=1 in Eq. (3.11). To reduce this value of power, the DSAR formation can be conceived with larger number of degrees than the ones strictly required by the reconstruction algorithm. Since not all the degrees of freedom are used to reduce PRF, residual redundancy is available to improve SNR or equivalently to reduce the required Tx power, as stated in Section 3.2.5. From Eq. (3.11), it is immediate to verify that the following relation holds

$$P_{Tx\_DSAR} \cong \frac{M}{N} P_{Tx\_Mono} \tag{3.13}$$

So, the designed DSAR system with N receivers is able to achieve the same azimuth resolution as an equivalent monostatic SAR, but simultaneously

- achieving a swathwidth that is larger by a factor of M
- working with PRF that is lower by a factor of M
- working with a transmitted power that is smaller by a factor of about M/N.

In the case of this study, a formation composed of 4 platforms working at PRF halved with respect to the Nyquist frequency enables the achievement of azimuth resolution of 1 meter with 2.6 kW of peak power.

3.5.2 Scenario 3

This scenario comprises a cluster of passive receivers flying in formation in the same orbit of an illuminator of opportunity [87]. This is an active satellite, which can be also part of a pre-existing mission, emitting radar signals echoed by the illuminated scene and collected by the passive receivers in the formation. The distance between the cluster and the illuminator is about 100 km. The distance between the satellites in the formation, instead, is in the order of hundreds of meters. Table 14 lists the orbital and SAR parameters of the considered illuminator.

Table 14 Orbital and SAR parameters of the selected illuminator of opportunity [87]

Parameter	**Value**
Orbit	SSO dawn-dusk LTAN 05:45
Mean altitude	410 km
Eccentricity	0.001095
Inclination	97.0021
Daily orbits	15.5625
Swath	15x15 km
Risoluzioni	3 x 3 m
Incidence angles	20°- 40°
NESZ	-13 dB
Incidence angle	20° - 40 °
Peak power	< 1 kW
Antenna dimensions	3.4 m x 0.7 m

The aim of test case scenario 3 is to show the capability to match illuminator SAR performances even working with limited platforms by exploiting FF-SAR applications.

Monostatic performance

The first value to be set is the working PRF. This value should guarantee a) proper sampling of Doppler band, b) avoid range ambiguities, c) avoid nadir echoes. To do this, again, the timing diagram described in Section 3.4.2 has been used. Using the values listed in Table 14, the timing diagram shown in Figure 23 has been obtained. The vertical lines indicate, respectively:

- the Doppler band, which is the PRF lower bound for proper sampling (blue line) equals to 4.5 kHz
- the PRF with an up-sampling factor of 20% with respect to the Doppler band (magenta line) equals to 5.1 kHz
- the working PRF which ensures the required swath without range ambiguities and nadir echoes equals to 5.4 kHz

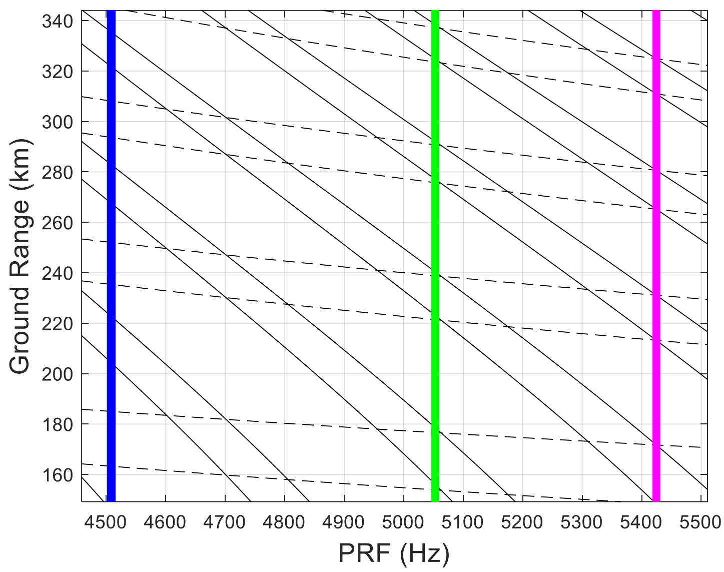

Figure 23 Timing Diagram for Scenario 3

To verify that these PRF values are correct for the required NESZ of -13 dB, the NESZ can be computed by Eq. (3.11). Using the values listed in Table 14 in the Eq. (3.11), the following values of $NESZ_{mono}$, at far range, are obtained:

- Minimum PRF (4.5 kHz): -12.9 dB
- Medium PRF (5.1 kHz): -13.5 dB.
- Maximum PRF (5.4 kHz): -13.7 dB.

These values confirm the requirement of -13 dB of the illuminator, i.e., the correct definition of the PRF values by varying the off-nadir pointing of the monostatic SAR antenna.

Bistatic configuration

Once defined the parameters of the illuminator of opportunity, it is possible to characterize the formation of passive receivers. First, a formation including a single receiver is considered. In this way the bistatic SAR performance of the single receiver can be compared to the performance of the monostatic platform. In the Figure 24, a bistatic configuration comprises a monostatic SAR and bistatic passive platform working at the same altitude and separated of 100 km in along-direction is shown.

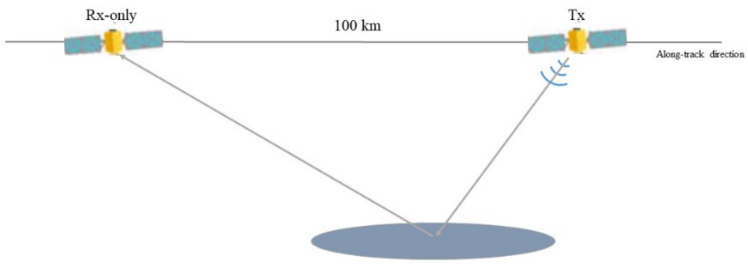

Figure 24 Bistatic Configuration

For a X-Band LEO satellite, the critical baseline, i.e., the relative distance between distance after which is not more possible the coherent combination of the collected signals, is in the order of kilometres. Specifically, this value can be evaluated as

$$B_{AT,critical} = \frac{2\lambda}{V_{Tx}} R_0 \frac{V_g}{L_{eff}} \tag{3.14}$$

where V_g is the ground velocity of the beam, while L_{eff} is the effective length of the antenna, computed as $L_{eff} = \sqrt{\frac{{L_{Tx}}^2 + {L_{Rx}}^2}{2}}$. In this case, the value of $B_{AT,critical}$ is about 15 km. Table 15 resumes the values characterizing the configuration in exam.

Table 15 Characteristics of configuration in exam

Parameter	**Value**
Altitude	410 km
Critical baseline	15.3 km
Along-track baseline	100 km

Therefore, an along-track baseline of 100 km is way bigger than the critical value, and consequently, it is not possible to combine coherently the bistatic data with the monostatic ones. However, this condition does not affect the operability of the formation and the applicability of the FF-SAR applications. Indeed, the only requirement is on the distance between the elements of the formation and not between the formation and the illuminator. Moreover, it is known that the bistatic configuration introduces geometric and radiometric distorsions in the bistatic images (range/azimuth skewing, changing resolution, bistatic scattering). Nonetheless, these effects can be ignored because:

- the along-track baseline is still much less than the slant range
- the velocity vectors of the platforms are very similar

The estimation of resolution and NESZ of the single satellite of the formation is now given. For this purpose, three different beams inside the assigned interval (20° - 40°) of incidence angles are taken into consideration. For each beam, the variation of ground range and azimuth resolutions is determined. Table 16 reports the beams with the corresponding incidence angles and swath width.

Table 16 Selected beams

Beam ID	**Interval of incidence angles (deg)**	**Swath (km)**
B1	20 – 22	15
B2	29 – 31	15
B3	38 – 40	15

For each beam, the gradient method [88] can be applied to compute the ground-range and azimuth resolutions by considering the transmitter and receiver velocities and positions, the target position, and system parameters as the bandwidth of the transmitted signal and CPI. The values obtained for each beam are reported in Figure 25 and Figure 26.

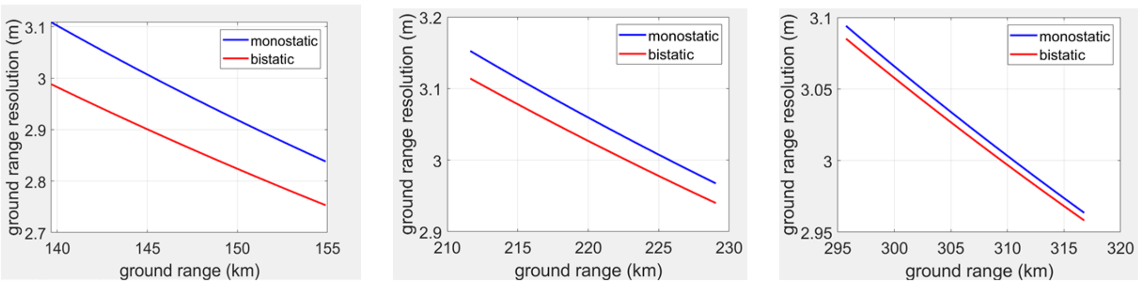

Figure 25 Comparison of ground-range resolutions, with an along-track baseline of 100 km, between the monostatic and bistatic configurations. B1 (left), B2 (center), B3 (right).

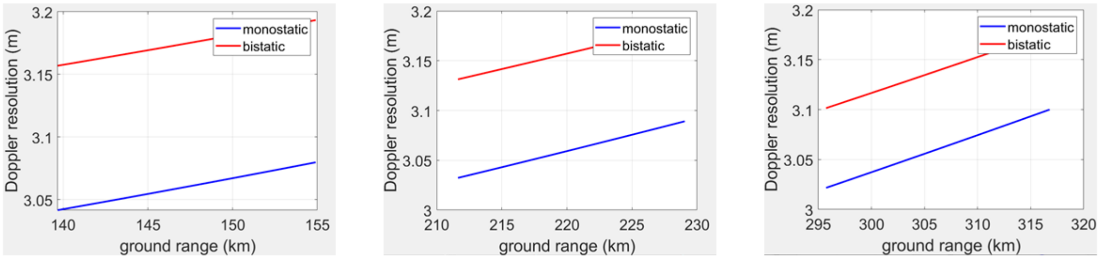

Figure 26 Comparison of azimuth resolutions, with an along-track baseline of 100 km, between the monostatic and bistatic configurations. B1 (left), B2 (center), B3 (right).

From Figure 25 and Figure 26, one can conclude that the bistatic geometry does not introduce significant variations in terms of resolution, confirming the design hypothesis. For what concerns the bistatic NESZ, this must be computed and compared to the value of -13.5 dB, obtained in the monostatic case with a PRF of 5.1 kHz. The NESZ is estimated in the worst case, i.e., for a far-range target at an incidence angle of 40°. The bistatic NESZ can be computed as

$$NESZ_{bistatico} = \frac{(4\pi)^3 {R_{Tx}}^2 {R_{Rx}}^2 k_B T_n B_n F_n}{(CPI \cdot PRF) \cdot (\tau_P B) P_{Tx} G_{Tx} \Delta A \lambda^2 G_{Rx}} \tag{3.15}$$

in which R_{Rx} represents the target-receiver range and G_{Rx} is the gain of the antenna used in the passive platform. The other parameters are listed in Table 13. For what concerns the bistatic antenna on-board of each platform of the formation, the reference parameters of the antenna in [35] have been assumed, which are listed in Table 17.

Table 17 Parameters of reference antenna [35]

Parameter	**Value**
Aperture (radius)	0.5 m
Efficiency	60 %
Gain	34.8 dB
CubeSat class	12U

Hence, a value of -9.41 dB for the NESZ can be obtained. Table 18 reports the comparison between the monostatic and bistatic case.

Table 18 NESZ comparison between monostatic and bistatic configuration

Configuration	NESZ
Monostatic	-13.48 dB
Bistatic	-9.41 dB

To match the monostatic performance, the formation must include more than one platform. The number of platforms can be computed as described in Section 3.4.2, where it has been seen that

$$SNR_{FF-SAR} = \sum_{i=1}^{N} SNR^{i}{}_{bistatic} \tag{3.16}$$

Hence, by using three receivers in close formation, the NESZ value improves from -9.41 dB of the bistatic case, to -14.18 dB of the FF-SAR, matching the monostatic performance. Table 19 resumes the value of NESZ for each configuration.

Table 19 Computed NESZ for each configuration

Configuration	NESZ
Monostatic	-13.5 dB
Bistatic	-9.41 dB
FF-SAR (3 receivers)	-14.2 dB

4. DSAR Simulator

Since no real space acquisitions are yet available to verify properties and performance achievable by FF-SAR system, high-fidelity numerical simulations are the only way to test FF-SAR concept. Furthermore, existing analytical models for performance estimation are not adequate to include all the error sources that can spoil the actual performance. In this chapter, a DSAR simulator is introduced to estimate the effects of different error sources on system performance. These error sources are modelled and applied during the processing phase, enabling the estimation of the effects of a single error and/or of a combination of them.

4.1 Simulation Environment

A simulator has been developed to generate raw data collected by each receiver, then to perform DSAR processing, and, finally, to derive image quality parameters to test how SAR imaging is affected by the integrated errors. Point targets are assumed to be in the scene thus leading to an estimate of DSAR point target response. Distributed targets and topography-related effects can be simulated as dense clusters of point targets. A scheme of the implemented simulator is shown in Figure 27. Specifically, "orbit propagation" block is in charge of propagating the orbits and the attitude of the transmitter and all of the receivers, "scene simulator" is in charge of generating N raw images, one for each Tx/Rx couple, while "DSAR processing" block is in charge of implementing beamforming and bistatic SAR focusing to generate R focused images (R≤N). Those images can be subject to a further, higher level, processing to implement special working modes like 3D imaging (SAR tomography) or GMTI. The relevant algorithms are well-known from the interferometric SAR literature, so they are not further discussed herein (the interested reader is referred to [89]). With reference to Figure 27, initial conditions are set on the basis of the available DSAR formation design, including starting time epoch, initial position and velocity of both the transmitter and the N receiving-only platforms. Based on these input initial parameters, orbits have been propagated by GMAT software [90].

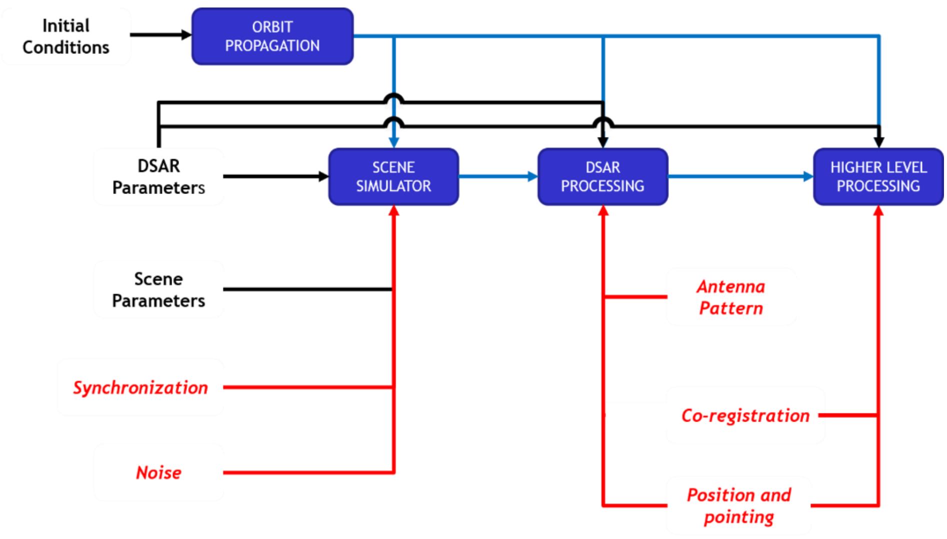

Figure 27 Simulation environment architecture: input parameters are indicated in black, whereas error sources are depicted in red

Output parameters from the orbit propagation, as well as DSAR parameters (i.e., wavelength, pulse length, signal bandwidth, PRF of the transmitter, antenna type, and antenna size), scene parameters including the location of a given number of point targets distributed over Earth surface, and first and last time instant of data take, are the input to the scene simulator block. Every raw image generated by the scene simulator block is a fast-time slow-time matrix, completed by fast and slow time vectors. The scene is simulated accounting for sensor related perturbations, and for both lack of synchronization among the SARs and signal noise. The N raw images are then processed by DSAR processing block that generates R focused images (where the current value of R depends on the considered application). Since the processing can be affected by uncertainties on the position, velocity and attitude of the orbiting platforms, these effects have been integrated in the simulation environment modifying the error-free data to generate simulations of the errors due to antenna-pattern, co-registration, positioning and pointing as illustrated in the next sections.

4.2 Scene simulation

The first step of scene simulation is the interpolation of satellite positions, velocities, and attitude at the working PRF. This interpolation is necessary because propagation is realized, typically, at relatively long-time steps (e.g., 0.1-1 s) whereas raw data generation requires the definition of satellite positions and velocities at each slow time instant (e.g., with a frequency in the order of kHz). Moreover, interpolation allows the same propagated orbits to be used in different DSAR simulation, that is considering a DSAR operating with different working parameters. In the implemented simulation, interpolation is performed as 1D spline for each position and velocity coordinate. Based on the interpolated orbits and assigned locations of point targets, raw images are generated using the start/stop approximation [91], i.e., neglecting the instantaneous Doppler affecting the transmission/reception of each pulse. The model of the simulated target echo is [91]

$$
\begin{aligned}
S_{Rx}(\tau, t, \mathbf{P}_{\text{target}}) = & \, G_{Tx}\left(t, \mathbf{P}_{\text{target}}\right) \cdot G_{Rx}\left(t, \mathbf{P}_{\text{target}}\right) \cdot \\
& \exp\left\{ j \left[-\frac{2\pi}{\lambda}\left(R_{Tx}(t) + R_{Rx}(t)\right) \right] \right\} \cdot \exp\left\{ j \left[\pi\alpha \left(\tau - \frac{R_{Tx}(t) + R_{Rx}(t)}{c} \right)^2 \right] \right\} \cdot \\
& rect\left(\frac{\tau_d\left(\tau, t, \mathbf{P}_{\text{target}}\right)}{\tau_p} \right)
\end{aligned}
\tag{4.1}
$$

where τ is fast time, t is slow time, $\mathbf{P}_{\text{target}}$ is target position in ECEF, G_{Tx} and G_{Rx} are, respectively, Tx and Rx antenna gains in the direction of the targets which depend on the positions of Tx and Rx at the considered slow time, i.e. $\mathbf{P}_{Tx}(t)$ and $\mathbf{P}_{Rx}(t)$, λ is the radar wavelength, α is the chirp rate, c is the speed of light and

$$
\begin{aligned}
R_{Tx} &= \left|\mathbf{P}_{Tx}(t) - \mathbf{P}_{\text{target}}\right| \\
R_{Rx} &= \left|\mathbf{P}_{Rx}(t) - \mathbf{P}_{\text{target}}\right|
\end{aligned}
\tag{4.2}
$$

The basic assumption of the model in Eq. (4.1) is that demodulation (or carrier removal) can be correctly done, i.e., the case of perfect clock synchronization is assumed. In the application at hand, the simulation of the acquired data accounts for both synchronization errors, due to an offset between the oscillator nominal frequencies (Δf) and to the phase noise affecting the Tx and Rx clocks (ϕ_{st}) [92] (Section 4.2.1). The standard thermal signal noise is also injected (see Section 4.2.2). More specifically, synchronization errors are introduced by modifying the collected bistatic raw data according to pseudorandom realizations of Δf and ϕ_{st} that perturb each bistatic receiver.

Taking into account synchronizations errors, the simulated target echo of Eq. (4.1) can be rewritten as

$$
\begin{aligned}
S_{Rx}(\tau,t,\mathbf{P}_{\text{target}}) &= G_{Tx}\left(t,\mathbf{P}_{\text{target}}\right)\cdot G_{Rx}\left(t,\mathbf{P}_{\text{target}}\right)\cdot \\
&\exp\left\{j\left[-\frac{2\pi}{\lambda}\right]\left(R_{Tx}(t)+R_{Rx}(t)\right)\right\}\cdot\exp\left\{j\left[\pi\alpha\left(\tau-\frac{R_{Tx}(t)+R_{Rx}(t)-\varepsilon_{time}}{c}\right)^2\right]\right\}\cdot \\
&\exp\left[j\left(\varepsilon_{phase}\right)\right]\cdot rect\left(\frac{\tau_d\left(\tau,t,\mathbf{P}_{\text{target}}\right)}{\tau_p}\right)
\end{aligned}
\tag{4.3}
$$

with ε_{time} representing the synchronization error in the fast time and ε_{phase} referring to the phase error that are illustrated in the next subsection.

4.2.1 Synchronization errors

The first contribution in Eq. (4.3) is assumed to depend only on slow time. Basically, it is caused by the deviation of both the Tx and Rx actual carrier frequencies (f_c^{Tx} and f_c^{Rx}, respectively) from the nominal value (f_c). In such a circumstance

$$\varepsilon_{time}(t)=\frac{\delta f}{f_c}t \tag{4.4}$$

where t is the generic slow-time instant and δf is the difference in carrier frequencies, i.e. $\delta f = f_c^{Tx}-f_c^{Rx}$. Since it is assumed to be a constant value over the whole acquisition period [93], δf is simulated for each Tx-Rx couple as single random extraction from a normal distribution with zero-mean and $\sigma_{\delta f}$ standard deviation. Concerning $\sigma_{\delta f}$, it is equal to $\frac{f_c}{f_{USO}}\Delta f$, with f_{USO} indicating the oscillator frequency. An uncompensated frequency difference among the clocks is responsible for disturbances in the phase of bistatic signals too. In details, δf related error accumulates over (fast) time, thus producing a phase deviation from the ideal one that is generally referred to as phase ramp. The difference between oscillator frequencies is strictly speaking a function of time. However, it changes very slowly over time, in the order of 6 Hz/year [16]. This means that for a simulation, up to several minutes long, the difference between oscillator frequencies can be kept constant. A typical range of values for the difference depends on the type of oscillator that is used. With reference to space qualified Ultra Stable Oscillators (USO) working at 10 MHz and customarily used in monostatic SAR, the difference is just a few Hz [16]. An additional contribution is considered in phase ε_{phase}, that is the phase noise ϕ_{st} affecting SAR oscillators [92]. In other words,

$$\varepsilon_{phase} = 2\pi\delta f + \varphi_{st} \tag{4.5}$$

where φ_{st} is relevant to the carrier frequency and it is computed from the phase noise realizations at the oscillator frequency ϕ_{st} simulated for the entire acquisition as in [95].

4.2.2 Signal noise

For what concerns signal noise, radar equation is used as a reference to simulate the effects of noise in the collected radar data. So, the amount of noise power is estimated according to the standard thermal noise model

$$\sigma_{noise}^2 = k_B F_n B_n T_n \tag{4.6}$$

with k_B Boltzmann's constant, T_n noise temperature, B_n noise bandwidth, and F_n noise figure. The level of noise power is then used to inject noise in both real and imaginary part of the simulated raw signal. In detail, two sequences of random samples extracted from a Gaussian distribution with standard deviation

$$\sigma_{I/Q} = \frac{1}{\sqrt{2}}\sigma_{Noise} \tag{4.7}$$

are added to the pixels of simulated raw data [91]. Simulations assume noise bandwidth coincident to the bandwidth of the Tx signal [96]. Concerning the received signal power, this is simulated as

$$POW_{Rx} = \eta_{loss} \frac{POW_{Tx} G_{Tx} G_{Rx} \lambda^2}{(4\pi)^3 R_{Tx}^2 R_{Rx}^2} \sigma \tag{4.8}$$

with POW_{Rx} the Rx power, η_{loss} loss factor (e.g., including Tx loss, atmospheric loss, and design buffer), σ the radar cross section of the simulated target.

4.3 DSAR processing

Generated raw data are to be processed by both beamforming and SAR focusing algorithms. These algorithms can be applied both in time and frequency domain. DSAR processing chain shows important differences in the two domains. As described in Section 3.2.2, the most important one is that in the frequency domain beamforming is performed before SAR focusing while in the time domain is performed with the focusing. Whatever the case, the basics behind the integration of error sources in the simulation environment are the same. Indeed, SAR focusing, and beamforming must rely on measurements of position, velocity and attitude of the orbiting platforms. Within the simulation environment, the uncertainties in the knowledge of the actual values of position, velocity, and attitude are simulated by modifying the error-free data as generated by the orbit propagation block.

4.3.1 Bistatic SAR focusing

Both time and frequency domain solutions for DSAR processing are implemented in the simulation environment. In this way more flexibility is enabled in terms of the multistatic geometries which can be simulated and processed.

Time Domain focusing

Time domain focusing computes, numerically, the convolution integral representing slow time azimuth compression. The problem can be formulated as follows. The focused image value at fast time/slow time coordinates is computed as [93]

$$M(t_0, \tau_0) = \int_{-T/2}^{T/2} C\left(\frac{R_b(t, \mathbf{P}(t_0, \tau_0))}{c}\right) \exp\left[j \frac{2\pi}{\lambda} R_b(t, \mathbf{P}(t_0, \tau_0))\right] dt \tag{4.9}$$

where M is the focused image, C is the range-compressed one, T is the integration time, $\mathbf{P}(t_0,\tau_0)$ is the position of the target to be mapped on image coordinates (t_0,τ_0), $R_b(t,\mathbf{P}(t_0,\tau_0))$ is the bistatic slant range, at the slow time t of the target located at $\mathbf{P}(t_0,\tau_0)$. It is worth noting that the integral in Eq. (4.9) must be computed within the integration time of the target $\mathbf{P}$ and along the bistatic range line corresponding to the bistatic range history of that target. The numerical implementation of the integral in Eq. (4.9) is performed as illustrated in Figure 28. The fundamental idea is that the integral is replaced by a slow time discrete summation. Specifically, for each slow time instant (meaning for any position and velocity of both Tx and Rx), the expected phase for each pixel of the focused image is calculated and the relevant complex conjugate value is multiplied by the return from the specific cell in the range compressed image line corresponding to that pixel at the considered slow time instant. The application of Eq. (4.9) requires the definition of target positions $\mathbf{P}(t_0,\tau_0)=\mathbf{P}(t(i_F),\tau(j_F))=\mathbf{P}(i_F,j_F)$ to be mapped on image coordinates $(i_{F,}j_F)$. This means that, for each pixel of the focused image, a vector must be computed indicating the position of that pixel, and the relevant location at the current slow time instant in the range compressed image, i.e. $(i_{RC,}j_{RC})$ in Figure 28. A standard georeferencing problem can be solved to compute the unknown location.

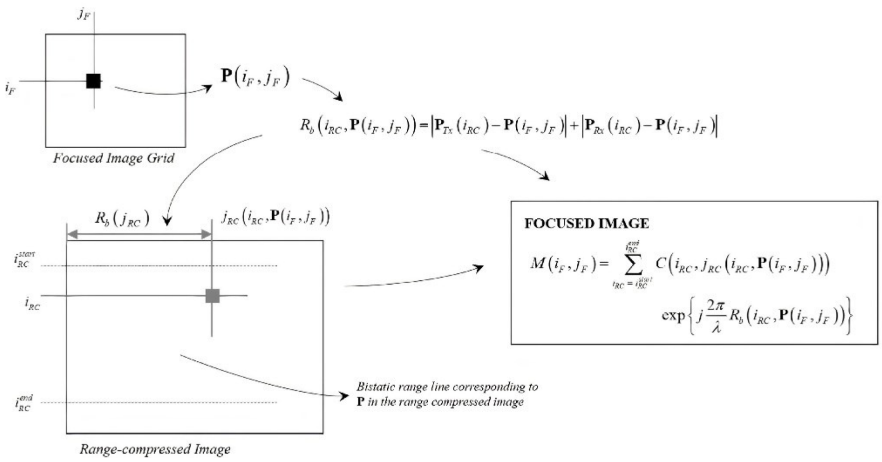

Figure 28 Illustration of the implemented time-domain bistatic SAR focusing algorithm

The generalization of the time domain bistatic SAR focusing to the DSAR case for implementing HRWS imaging must account for a beamforming step. This can be implemented as described in Section 3.2.2. Considering all the available receivers, the relevant terms are successively weighted by an additional complex coefficient coming from the solution of the beamforming problem. The latter can be set, for instance, to suppress the first forward and backward azimuth ambiguity, as in Section 3.2.2, but even more ambiguities can be removed if required, provided that a sufficient number of receivers is available.

Frequency Domain focusing

In the frequency domain, beamforming is performed before SAR focusing and it is aimed at reconstructing an equivalent bistatic or quasi monostatic signal which can be processed by a standard SAR processor, as described in Section 3.2.2. The output of the reconstruction method is then processed by SAR focusing. The selected algorithm for SAR focusing in the frequency domain is a customization of Range Doppler (RD) algorithm to bistatic data. The main steps of a standard monostatic RD algorithm [91] can be applied to bistatic raw data with small adaptations when quasi-stationarity in along-track direction can be assumed [94]. This assumption is made herein, meaning that Tx and Rx velocity vectors must be sufficiently similar to consider raw data to be azimuth invariant within a processing block. According to [94], quasi-stationarity in along-track direction can be assumed for LEO satellites flying in relatively short formations, e.g. with separations in the order of several km. For those bistatic geometries the concept of equivalent or effective velocity can be used to approximate, for each range bin, the bistatic range history by a hyperbolic function. This is very similar to hyperbolic range history approximation used to focus monostatic SAR satellite data (i.e., to account for orbit curvature) [91]. Specifically, the main difference between a RD algorithm for a monostatic spaceborne SAR and a bistatic one (under quasi-stationarity assumption) is that, owing to bistatic geometry, adapted values must be used for some processing parameter (e.g., effective velocity, effective squint angle, Doppler centroid frequency, beam center crossing time, and zero Doppler time). Applicability limits of the developed frequency domain algorithm for bistatic SAR focusing deals with the following two main assumptions: 1) hyperbolic range history, 2) azimuth invariance or slow time stationarity. With specific reference to the second assumption, processing parameters are estimated by georeferencing of a single image line and then, they are used to focus an entire processing block. Since a general bistatic geometry is, by definition, space variant, using parameters estimated in a specific location of the processing block introduce errors when other portions of the processing block are handled. Nonetheless any algorithm that uses Fourier transforms in slow time relies on the assumption of azimuth invariance. As noted in [94], in the case of significant non-stationarity, the azimuth processing blocks must be shortened to avoid image degradation but in this case computational load and processing time can become similar to time-domain processing which is in general more precise. A simple procedure can be used to test the validity of both the above assumptions for an assigned bistatic geometry. Based on the knowledge of positions and velocities of the platforms, for any ground point, the range history can be estimated and the difference between this history and the relevant hyperbolic approximation can be evaluated. If the difference is negligible with respect to the signal wavelength one is allowed to assume a hyperbolic range history. A similar approach can be used to test the validity of azimuth invariance. Namely the size of the processing block must be introduced. A typical choice is 5 synthetic apertures [94]. Then processing parameters, and specifically the effective velocity, can be computed for an image line placed at the center of the processing block. The difference between the true range history at the edges of the processing block and the hyperbolic approximation computed in the middle of the processing block is a measure of the validity of azimuth invariance assumption. Following [94], one can use the standard $\pi/4$ phase error as a measure of the maximum allowed range error: this means that the maximum range error is limited by $\lambda/8$.

4.3.2 Simulation of Error sources

Positioning errors

Positioning errors are introduced by altering actual values of "true" position and velocity vectors as generated by GMAT. All the satellites in the formation are assumed to embark, at least, a Global Navigation Satellite System (GNSS) receiver. The measurements collected by those receivers represent the main input to the determination of satellite position and velocity, either on-board in real-time or on the ground in post-processing. Since a significant amount of position and velocity errors is space-correlated [97], if Tx and Rx are in the same formation working with limited separations (up to a few km), the vast majority of position and velocity errors are shared by all the satellite in the formation. Residual differences exist which can be reasonably assumed to show a random behavior [98]. Concerning this, the common portion of the error is representative of the absolute positioning and velocity errors, whereas the random contribution measures differential GNSS errors [99]-[100]. As a further remark, it is worth noting that, when relatively short time simulations are run, e.g., a few seconds long, for simulating the acquisition of a single data take, common errors among the satellites can be also assumed as time correlated. This is because no significant variations in GNSS satellite geometry occur in short time spans. Hence, simulations of positioning and velocity errors are implemented as a constant error contribution which is common to all the satellites and a random error contribution, which differs among satellites. Such an approach can simulate the cases of both absolute and relative navigation, and either real-time or offline differential GNSS. Specifically, the difference among those working modes can be represented by different values of common and random errors.

Pointing errors

Pointing errors are introduced simulating attitude errors by considering a Φ rotation of the Antenna Reference Frame (*ARF*) about a generic axis $\mathbf{e}$. This rotation axis $\mathbf{e}=[e_1,e_2,e_3]$ is randomly generated in the ideal *ARF*, as well as the Φ angle, which is selected in the [0.01°, 0.1°] range. Hence, a $\mathbf{R}_{ARF\to ARF_{err}}$ rotation matrix can be derived at each time instant for the generic platform of the simulated formation. The general direction cosine matrix from the ideal *ARF* to the perturbed *ARF* (*ARF$_{err}$*) is given by [101]

$$\mathbf{R}_{ARF\to ARF_{err}} = \cos\Phi\mathbf{1} + (1-\cos\Phi)\mathbf{e}\mathbf{e}^T - \sin\Phi\mathbf{E} \tag{4.10}$$

where 1 is the identity matrix and E is expressed as

$$\mathbf{E} = \begin{pmatrix} 0 & -e_3 & e_2 \\ e_3 & 0 & -e_1 \\ -e_2 & e_1 & 0 \end{pmatrix} \tag{4.11}$$

The erroneous knowledge of the satellite attitude entails the presence of some errors in the bistatic SAR focusing. In other words, the raw images, that are generated by exploiting the actual acquisition geometry derived from GMAT data, are processed by reproducing the antenna pointing errors caused by inaccurate information about the satellite attitude. Effectively, this means that the Line-Of-Sight (LOS) from spacecraft to target has to be expressed in the perturbed ARF in order to evaluate both the cone-angle, ϕ, and the azimuth-angle, θ, defining the antenna pattern. Pattern related errors are simulated by altering the antenna gain (G) of transmitting and receiving devices during SAR focusing. The representative difference between the reconstructed and the actual pattern can set in dBs as [102]

$$10\log\left(\frac{G}{G_{actual}}\right) = \Delta G_{dB} \tag{4.12}$$

Therefore, during focusing of bistatic SAR images the antenna gains are multiplied by a factor of $10^{Patt_{err}/10}$, where $Patt_{err}$ is the result of a random extraction from a zero-mean normal distribution characterized by a standard deviation equal to ΔG_{dB}.

4.4 Performance and sensitivity analysis

In this section, the above-introduced errors are included in the simulations to carry out a performance and sensitivity analysis. The effects of the errors on the acquisitions are investigated for DSAR formations aimed both at applications requiring along-track observation geometries, e.g. HRWS, and at applications asking for large cross-track separations, e.g. CRE. The first formation is called herein Safe Along-Track (SAT) formation, which falls in the safe ellipse category as described in Section 3.4.1, while the second formation is defined Long Effective Baseline (LEB) formation, in which satellite trajectories are designed so that the baselines' component normal to the line of sight, or effective baselines, generate a minimum redundancy array geometry. The relevant performance parameters, i.e., IRW, PSLR and ISLR, are estimated for each formation. The analysis is conducted with reference to bistatic SAR focusing and beamforming. It has a two-fold scope: i) understanding of the effect of error sources on the bistatic SAR focusing, ii) assessment of HRWS and CRE feasibility by DSAR when error sources are taken into account.

4.4.1 Bistatic SAR focusing

The performance and sensitivity analysis are performed introducing one by one the errors in the simulation chain and the performance parameters are estimated for the bistatic acquisition characterized by the largest separation from the Tx (i.e. the longest baseline). This is expected to lead to a better understanding of the effect of the single error source on the point target response. Figure 29 shows the normalized signal magnitude for the Rx of SAT formation with the longest baseline. The case with all error sources (Figure 29 right) includes synchronization errors. The effects of the error source on the performance parameters are more evident in Figure 30, which shows the 2D signal magnitude projections along the central peak coordinates. The first outcome is that the central peak and, thus, the resolution is not affected by the errors either in range or azimuth direction. On the contrary, the effect on the side-lobes is an increased asymmetry of the lobes both in range and azimuth direction. Moreover, the PSLR and the ISLR are mostly affected by signal noise. Computed performance parameters are listed in Table 20.

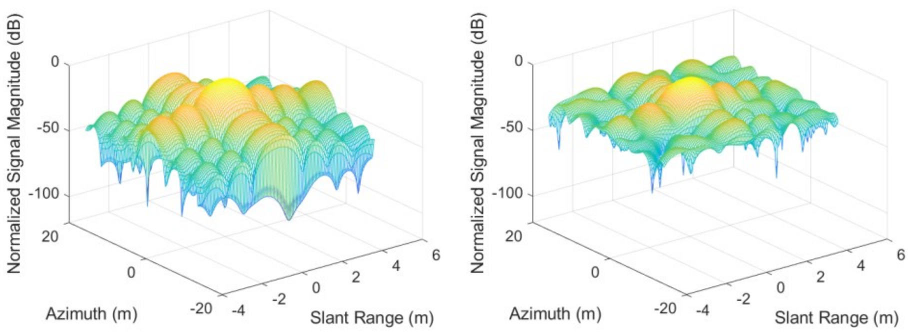

Figure 29 Signal magnitude of bistatic acquisition for the longest baseline Rx of SAT formation: (left) error-free case and (right) effect of error sources.

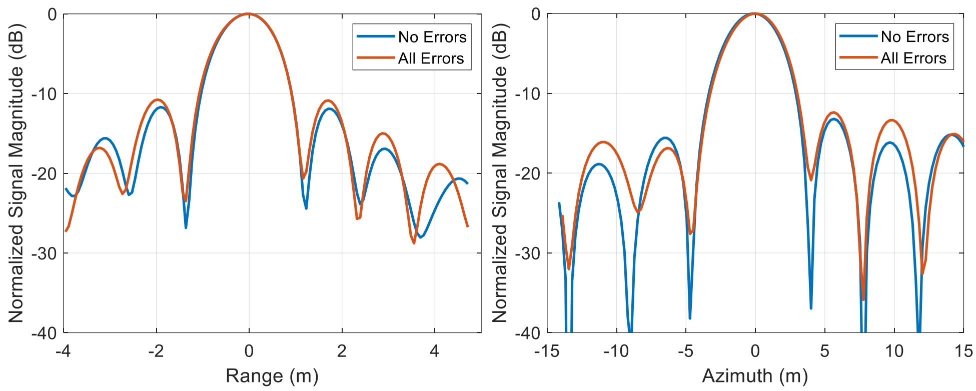

Figure 30 Signal magnitude of bistatic acquisition for the longest baseline Rx of SAT formation along the range (left) and azimuth (right) direction

Table 20 Parameters for the longest baseline Rx of SAT formation

		IRW	PSLR (dB)	ISLR (dB)
No errors	*Range*	1	-11.70	-9.90
	Azimuth	1	-13.20	-10.99
Signal Noise	*Range*	1	-10.38	-9.06
	Azimuth	1	-12.61	-10.08
Positioning	*Range*	1	-11.45	-9.93
	Azimuth	1.2	-13.14	-10.77
Pointing	*Range*	1	-11.70	-9.90
	Azimuth	1	-13.20	-10.99
Antenna Pattern	*Range*	1	-11.70	-9.90
	Azimuth	1	-13.20	-10.99
Synchronization	*Range*	1	-11.70	-9.90
	Azimuth	1	-13.20	-10.99
All Errors	*Range*	1	-10.76	-9.09
	Azimuth	1	-12.38	-9.78

Results dealing with the longest baseline Rx of LEB formation satellite are reported herein. Figure 31 and Figure 32 show the normalized signal magnitude and its 2D projection along the peak coordinates, respectively, both for noise-free case and including error sources. The effect of the signal noise is the most evident one and the degradation of the PSLR and ISLR is significant along either range or azimuth direction, as shown by the computed performance parameters that are listed in Table 21.

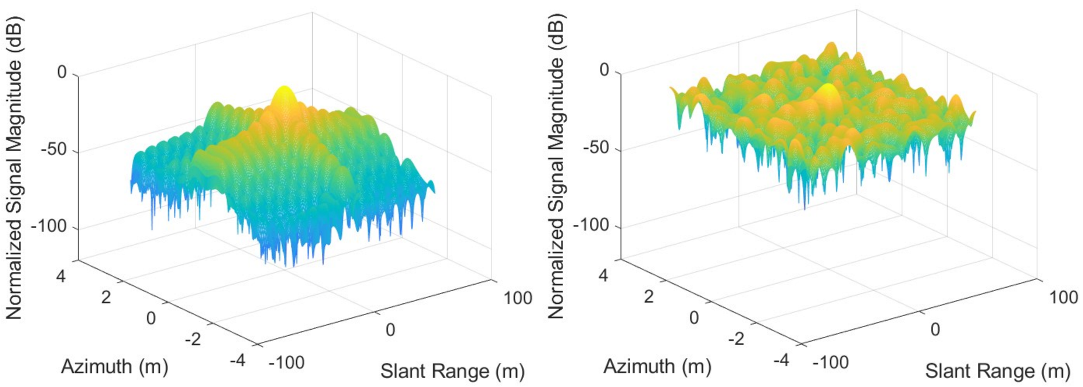

Figure 31 Signal magnitude for the longest baseline RX of LEB formation: (left) error-free case and (right) effect of error sources.

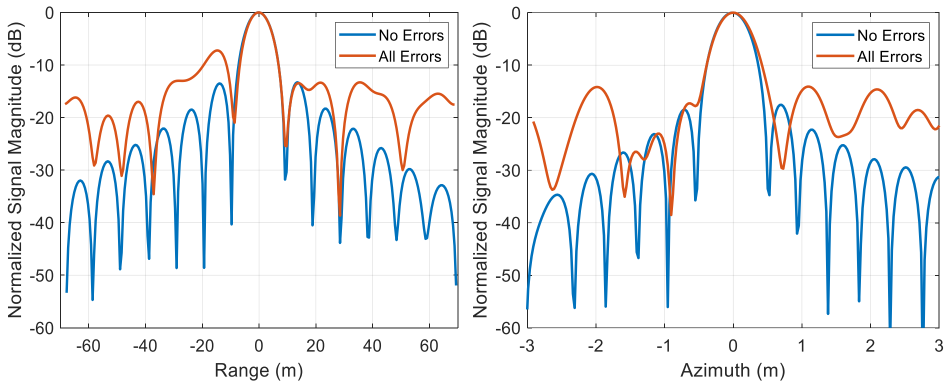

Figure 32 Signal magnitude for the longest baseline Rx of LEB formation along the range (left) and azimuth (right) direction.

Table 21 Parameters for the longest baseline Rx of LEB formation.

		IRW	PSLR (dB)	ISLR (dB)
No errors	*Range*	1	-13.28	-11.08
	Azimuth	1	-18.09	-16.03
All Errors	*Range*	1	-7.58	-4.29
	Azimuth	1	-12.26	-8.52

4.4.2 Beamforming

In the following sections, the applicability of beamforming procedure against error sources is investigated for both HRWS + SNR improvement and CRE. Concerning the former, Figure 33 (left) shows the normalized magnitude of the point target responses. Even if the azimuth ambiguities are partially masked by errors and noise, it is possible to distinguish the right ambiguity (located at about pixel number 1400). Figure 33 right shows the DSAR image resulting from the application of the azimuth beamforming algorithm. The results confirm that DSAR processing allows one to correctly place nulls towards azimuth ambiguities. Furthermore, it is possible to appreciate the achieved SNR improvement. For the sake of quantifying DSAR performance enhancement, both AASR and SNR are computed. AASR is -4.3 dB for the monostatic platform whereas it improves to -10.2 dB for the DSAR. Similarly, SNR improves 21.7 dB to 26.1 dB. SNR improvements is thus about about 4.4 dB.

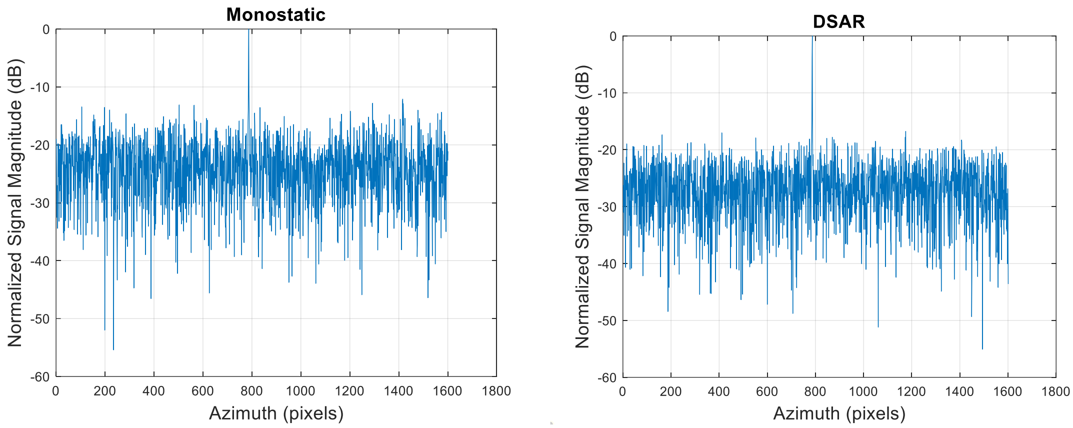

Figure 33 Normalized magnitude of the point target response before and after the azimuth beamforming.

With reference to CRE, Figure 34 shows the normalized signal magnitude of point target responses gathered by each satellite of LEB formation and the related spectra. As expected, the farthest platforms from the transmitter show also the maximum spectral shift. The point target response after the beamforming is shown in Figure 35. The estimation of the IRW allows one to state that range resolution decreases from 8.4 m for the monostatic platform to 4.7 m for the DSAR, which yields a ground range resolution improvement from 18.5 m to 10.2 m. The result agrees with CRE theory.

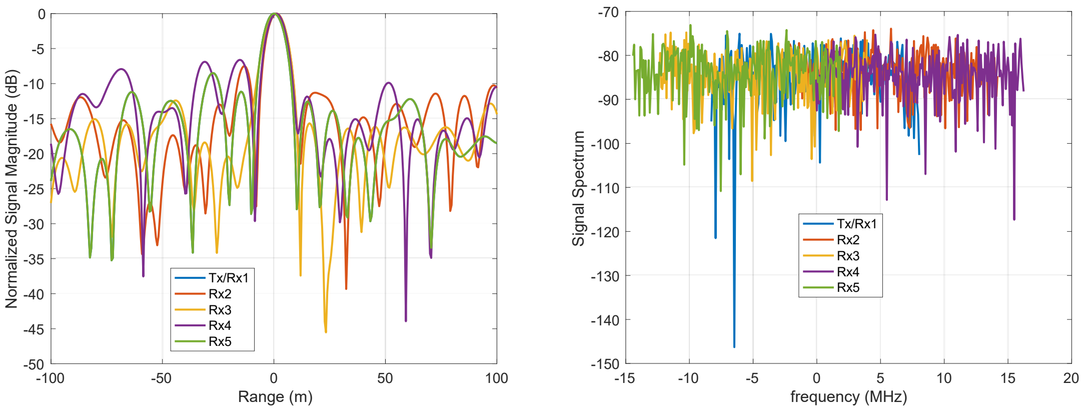

Figure 34 (left) Signal magnitude and (right) spectrum for different satellites of LEB formation.

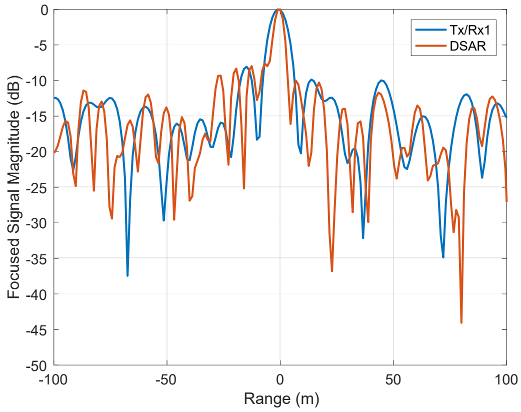

Figure 35 Signal magnitude of LEB formation before and after the beamforming.

4.5 Discussion

The error and sensitivity analysis has provided interesting outcomes regarding the performance of bistatic SAR and DSAR when the effect of error sources is included in the simulation. With reference to SAT formation, the results allow one to conclude that:

- the resolution (IRW) is not affected by error sources.
- the overall imaging performance is kept, even considering error sources.

With reference to LEB formation, the estimation of performance parameters has been carried out introducing all the error sources in the image generation process. The results suggest that

- the resolution (IRW) is not affected by error sources.
- the PSLR is degraded by a few dBs (3-6) both in range and in azimuth.
- the ISLR is degraded by several dBs (7-8) both in range and in azimuth.

The effect of error sources on beamforming algorithms and procedure has been also investigated. Concerning HRWS application, the results confirm that not only the ambiguity suppression is feasible with errors but also that the SNR can be improved, exploiting DSAR features. Similarly, the application of the digital beamforming algorithm for CRE when errors are simulated confirm that the improvement of the range resolution is feasible, since the impact of errors source on IRW is negligible. Ultimately, the sensitivity analysis conducted by the developed simulation environment confirmed that: DSAR can tolerate clock errors leading to phase discrepancies of a few tens degrees; the absolute and relative positioning accuracy achievable by differential GNSS enable DSAR imaging; the required accuracy in pointing, antenna pattern, and coregistration, is in line with well-assessed techniques; performance of spaceborne SAR operations.

5. Design of Small Satellites in FF-SAR perspective

The design of the individual FF-SAR platform is strongly dictated by the need of performing formation flying and SAR operations. Indeed, formation flying has a direct impact on ADCS, propulsion and communication subsystems. SAR operations, instead, demand high pointing capabilities, power, and thermal dissipation. In addition, the use of small satellites limits in a significant way the size, width, and power allowed for each satellite subsystem. This implies a driving trade-off between mission requirements and the current technological capabilities of small satellites.

A systematic analysis about the design of small platforms for performing FF-SAR operations is given in this paragraph. First, mission requirements of the three FF-SAR scenarios described in Section 3.5 are used as input parameters to the design. Then, formation-flying and SAR operations are translated into a specific requirement for the satellite bus. In this way, the most critical subsystems, and the fundamental capabilities they must possess, can be individuated. Once defined, a step-by-step procedure for designing each subsystem is given. Based on this analysis, the suitable satellite class for each mission is defined and, consequently, the proper hardware, satisfying both required performances and stringent requirements imposed by small satellites, can be selected. No assessments have been made at this level regarding the interfaces between the different subsystems and the compatibility between the different components. The goal here is to use the selected instrumentation to have a first estimate of the mass, power, and volume of the various subsystems and, consequently, to build indicative budget tables valid for the single satellite to be used as first design iteration.

5.1 Input parameters

For each scenario discussed in Section 3.5, a preliminary size of satellite subsystems is performed. In this way, the satellite class can be defined, and the proper hardware can be selected. For sake of clarity, the main characteristics of each scenario are recalled herein, in terms of type and number of platforms, satellite configuration, and mission objectives.

Scenario 1

- Semi-active configuration comprising three satellite: a fully active Transmitting-Receiving (Tx/Rx) satellite, i.e., a monostatic SAR platform, flying in formation with two Receiving (Rx) only satellites.
- Three working modes to demonstrate FF-SAR features, namely HRWS, CRE, and SAR tomography
- Suitable formation configurations to match the imaging requirements
- Enhancement of monostatic performance

Scenario 2

- Fully active configuration with four co-flying monostatic SAR platforms
- Single-plane constellation of eight evenly spaced formations
- Single-pass multi-baseline interferometry

Scenario 3

- Cluster of passive receivers flying in in the same orbit of an illuminator of opportunity
- HRWS imaging and SNR improvement
- Matching the illuminator SAR performances with limited platforms by exploiting FF-SAR applications

Design input parameters, for each scenario, are listed in Table 22. It must be pointed out that for the Scenario 1 and Scenario 2, which comprise both active and passive platforms, the SAR parameters are set for designing the active monostatic platform to match the imaging requirements based on the analysis of Section 3.5. For the Scenario 3, instead, the input parameters are relevant to the considered illuminator of opportunity.

Table 22 Design parameters for each scenario

	Parameters	Scenario 1 (Monostatic)	Scenario 2 (Monostatic)	Scenario 3 (Illuminator)
SAR imaging	Resolution	8 x 8 m	1 x 1 m	3 x 3 m
	NESZ	- 24 dB	-18 dB	-13.5 dB
SAR parameters	Antenna size	0.7 x 4.9 m	1 x 2 m	0.7 x 3.4 m
	Chirp bandwidth	100 MHz	100 MHz	80 MHz
	Pulse length	20 μs	20 μs	30 μs
	PRF	3.5 kHz	4.5 kHz	4.5 – 5.1 – 5.4 kHz
	Radar duty cycle	7 %	7 %	7 %
	Incidence angle	15 – 45 °	15 – 45 °	20 – 40 °
	Swath width	30 – 50 km	30 – 50 km	15 – 100 km
	Peak Power	up to 4 kW	2.6 kW	< 1 kW
	Average power	up to 260 W	up to 120 W	up to 100 W
	Data rate	200 Mbps	200 Mbps	500 Mbps
	Orbit duty cycle	5%	5%	2%
	Wavelength	9.6 GHz	9.6 GHz	9.6 GHz
Orbit	Altitude	550 km	528 km	410 km
	Eccentricity	-	-	0.001095
	Inclination	20 °	97 °	97 °

For what concerns the satellite class, the satellites shall be small satellites. In the specific, microsatellites (< 200 kg) are selected for the Scenario 1 and Scenario 2. The Scenario 3 involves the use of passive 12-16U CubeSats. The choice of microsatellites for the first two scenario has been dictated by the need of having fully active capabilities on-board of transmitting/receiving platform, by the mission configuration and requirements, and by the number of FF-SAR features to demonstrate. As a matter of fact, microsatellites great performances suitable for these applications. The use of CubeSats for FF-SAR missions, instead, is more challenging. However, the use of receiving-only platforms and the aim of demonstrating only HRWS and SNR improvements relax the bus requirements and justify the choice.

The aim of the design is to confirm the feasibility to use the selected satellite classes. In the next section, a step-by-step analysis to perform the preliminary design of the three mission scenarios, at subsystem level, is given.

5.2 FF-SAR platform design

The first step for designing FF-SAR platform is the assessment of the specific capabilities the platform must possess. To do this, the fundamental requirements related to formation flying and SAR operations must be defined to stress how they impact on the design of the platform.

Specifically, FF operations demand high degree of coordination among the satellites. For this purpose, a communication architecture is required to exchange formation status information, navigation and payload data via dedicated communication interlinks. Hence, the platform must be provided with Inter Satellite Link (ISL) channels, which has a direct impact on the design of communication subsystem. For formation maintenance and control, each satellite must compute its own absolute navigation state and the relative state with respect to the leader of the formation. Consequently, GPS receivers shall be installed on board each satellite. For executing precise control maneuvers to maintain or change the formation, the platform must be equipped with enough propulsive capabilities. In addition, propulsive capabilities are required also to have an accurate ground-track repeatability for interferometric applications. Indeed, the formation could be required to follow a reference absolute orbit defined with respect to the Earth. This involves orbit corrections by using cold-gas thrusters or electric propulsion.

Precise relative orbit determination is important not only for formation control, but it is an essential task for the generation of high-quality scientific products from distributed payloads. The properly combination of the images acquired by the distributed SAR antennas into a consistent scientific product, in fact, requires accuracy in the baseline knowledge at mm-level. However, since this accuracy can be achieved on ground by post-processing navigation data, it has not a direct impact on bus design. High accuracy pointing during SAR operations, instead, has a direct impact on the type of ADCS hardware to be used. For example, multi-head star sensors shall be used to satisfy the most stringent pointing phases, while sun and magnetic sensors are needed to ensure attitude acquisition, course pointing during data downlink, and sun pointing for electric power management (sun pointing will be used to maximize power input when SAR in not operating, this avoids installing rotating solar arrays). In addition, the platform shall be equipped with reaction wheels to guarantee high accuracy pointing and adequate slewing capability during SAR operations and for target pointing. Magnetic Torquers are needed for attitude initial acquisition and wheel unloading operations. Thermal Control Subsystem (TCS) must be properly sized to provide heat dissipation during SAR operations. In this sense, the radar RF unit could be installed in direct contact with a thermal radiator. For clock synchronization, since autonomous calibration using the monostatic image as a reference is considered, no additional device or hardware is required onboard.

Hence, for the design of FF-SAR platform particular attention must be devoted to the analysis of critical issues related to the electrical power subsystem, the thermal management, the attitude and orbit determination and control, formation maintenance, telecommunication, and data handling. The main requirements are listed in Table 23.

Table 23 Main subsystem requirements

Electric power System
Highly-efficiency, triple-junction thin film solar cells
Body-mounted solar cells and solar cells installed on the rear side of the deployable SAR antenna
Lithium-Ion secondary batteries, with high energy density.
A secondary battery with high discharge rate on board the Tx/Rx satellite to satisfy peak power
Batteries shall provide an energy storage to manage continued energy supply during eclipses and short-term peak power loadings at BOL.
The power distribution and control system shall regulate the distribution of the power loads to each subsystem component.
Propulsion System
The spacecraft shall be equipped with chemical thrusters
The spacecraft shall be injected on the same orbit plane of the illuminator of opportunity (scenario 3)
The spacecraft shall perform a phasing maneuver to reach a given along-track separation (scenario 2)
The spacecraft shall perform the phasing maneuver after detumbling
The spacecraft shall perform attitude maneuvers in order to provide a given thrust direction
The position of the thruster shall minimize plume impingement effect on the payload
Attitude and Control System
Multi-head star sensors to guarantee high-accuracy pointing during SAR operations
Sun and magnetic sensors, to ensure attitude acquisition, course pointing during data downlink, and sun pointing for electric power management (sun pointing will be used to maximize power input when SAR in not operating, this avoids installing rotating solar arrays).
Reaction wheels, to guarantee high-accuracy pointing and adequate slewing capability during SAR operation, for target pointing.
Magnetic Torquers, for attitude initial acquisition and wheel unloading operations.

Thermal control
Radar RF unit is installed in direct contact with a thermal radiator, so to provide heat dissipation during SAR operation.
Communication subsystem
The communication system shall be able to downlink the data collected during SAR operations
The communication system shall be able to downlink the daily acquired mission data in a single passage over the G/S.
The communication shall be performed in X-Band.
The communication system shall guarantee a reliable communication with the ground station for all the phases of the mission
The spacecraft shall be provided with GPS receivers to compute its own absolute navigation state and the relative state with respect to the leader of the formation
Dedicated Inter Satellite Links (ISL) channels are required to exchange navigation and status data.

5.2.1 SAR payload

A typical SAR payload based on small satellites [49] foresees a deployable, honeycomb planar antenna, combined with a very compact radio-frequency equipment. A rough estimation of masses for microsatellites can be found in [49], where a mass of 35 kg and 15 kg are assumed for the antenna and RF equipment, respectively. The SAR instrument mass reduces to about 35 kg for the Rx-only platforms, including both antenna e RF unit mass [49]. Differently, for 12-16 U CubeSat, the total mass of SAR payload including the antenna, can be assumed equal to 2-3 kg [36], with a volume of 1U for RF unit and 3U for the antenna. The high power required by RF unit of a transmitting microsatellite implies a total heat generation of about 800W. Finally, an average power of about 30 W can be selected when the radar is not transmitting for the Rx-only microsatellite [103]. A power of about 5 W is sufficient for the passive CubeSat [36]. This heat generation must be dissipated by the heat management system, which will be detailed in Section 5.2.4.

Table 24 Payload parameters

Parameter	**SCENARIO 1**		**SCENARIO 2**		**SCENARIO 3**
	Tx/Rx	Rx-only	Tx/Rx	Rx-only	Rx-only
SAR antenna mass (kg)	35	24.5	35	24.5	2
RF unit mass (kg)	15	10.5	15	10.5	1
RF power (W)	800	30	800	30	5

5.2.2 Bus

A preliminary estimate of the satellite dry mass and volume can be achieved assuming [104],[105], that the payload mass is 30% of spacecraft dry mass and the average spacecraft density is 79 kg/m3. Based on these data, one can derive the estimates for the Tx/Rx and Rx-only, as listed in *Table 25*, in which the mass of the overall structure of the satellite is estimated as the 25% of the dry mass [105].

Table 25 Preliminary mass and volume estimates for Tx/Rx and Rx-only satellites.

Item	**SCENARIO 1**		**SCENARIO 2**		**SCENARIO 3**
	Tx/Rx	Rx-only	Tx/Rx	Rx-only	Rx-only
Total dry mass (kg)	170	120	170	120	10
Satellite volume (m^3)	2.15	1.52	2.15	1.52	0.12 (12 U)
Mass of structures	42	30	42	30	2.5

5.2.3 Electrical Power Subsystem

Electrical Power Subsystem (EPS) is designed following a standard procedure as in [104], [105]. The battery is sized considering both the peak power requirement for SAR operations and the energy needed for bus operation during the eclipse time. Considering a SAR duty cycle (DC) per orbit and the peak power (P_{peak}) for SAR operation, the total energy required for SAR operations can be estimated as

$$E_{SAR} = P_{peak} \times \frac{DC_{orbit}}{60} \tag{5.1}$$

and the computed values are listed in Table 26.

Table 26 Duty cycle per orbit, peak power, and total energy required for SAR operations

	Scenario 1	**Scenario 2**	**Scenario 3**
Duty cycle	5 minutes	20 minutes	2 minutes
Peak power	4 kW	2.6 kW	30 W
E_{SAR}	333 Wh	867 Wh	2.5 Wh

The computation of the energy required for bus operation is performed assuming the average power bus requirement and the maximum eclipse time. For Scenario 1, since the orbit plane inclination is 20°, the instantaneous eclipse duration is very close to the maximum eclipse time

$$T_{ecl} = \frac{\sin^{-1}\left(\frac{R_e}{R_e + h}\right)}{\pi} P_k \cong 36\, min \tag{5.2}$$

where P_k is the Keplerian period (about 100 minutes), R_e is the Earth's radius and h is the satellite altitude.

For the Scenario 2 and Scenario 3, instead, the given orbit is sun-synchronous with an altitude of 410 km and 528 km, respectively. Hence, the maximum eclipse duration can be estimated as the 10% of the Keplerian period, i.e., about 10 minutes. The energy required for bus operations is then estimated as

$$E_{bus} = P_{ecl} \times \frac{T_{ecl}}{60} \tag{5.3}$$

where P_{ecl} is total average power required in eclipse, including the payload average power when SAR is not transmitting, thus $P_{ecl} = P_{bus} + P_{noTx}$. The satellite average power bus, P_{bus}, is the difference between the total average power requirement of the satellite and the average power required for SAR operations

$$P_{bus} = P_t - P_{pl} \tag{5.4}$$

where the average power required for payload is

$$P_{pl} = \frac{(P_{peak} \times DC_{radar}) \cdot DC_{orbit} + P_{noTX} \cdot (P_k - DC_{orbit})}{P_k} \tag{5.5}$$

in which DC_{radar} is the radar duty cycle, P_{noTX} is the average SAR power when the transmitter is turned off, and P_k is the Keplerian period. The payload power is between the 40% and 80% (i.e., x ~ 0.4-0.8) of the total power.

$$P_t = \frac{P_{pl}}{x} \tag{5.6}$$

Conservatively, x equals to 0.4 can be assumed for all the scenarios. Hence, the total required energy will be

$$E_b = E_{SAR} + E_{bus} \tag{5.7}$$

This energy must be restored into the battery during the sunlight phase. For the computation of the total required capacity, the Depth of Discharge (DOD) must be considered, according to the battery technology and the lifetime. Thus, the total energy to be stored in the battery is

$$E_{B,tot} = \frac{E_B}{DOD} \tag{5.8}$$

Finally, the required capacity is estimated as

$$C_b = \frac{E_{B,tot}}{V_d} \tag{5.9}$$

where V_d is the bus voltage, assumed to be equal, as typical, to 28 V for Scenario 1 and Scenario 2, and as 5 V for Scenario 3. Considering the input values of Table 22 related to each scenario, the used technology and the lifetime defined in Table 27, the relevant results for battery sizing reported in Table 27 are obtained.

Table 27 Relevant results for battery sizing

Item	**Scenario 1**	**Scenario 2**	**Scenario 3**
Total required energy (Wh), $E_b = E_{bus} + E_{SAR}$	1309	886	3.2
Battery-to-load power transfer efficiency	0.85	0.85	0.95
Technology for the battery design	Lithium-Ion	Lithium-Ion	Lithium-Ion
Lifetime	1 year	3 years	1 year
Depth-of-Discharge (DOD)	35%	25%	65%
Total energy to be stored in the battery (Wh), $E_{B,tot}$	3740	4173	5.80
Required capacity (Wh/V), C_b	133	151	0.21

Concerning the solar array design, the total energy required to the solar array can be computed using the following equation [104], [105]

$$P_{sa} = \frac{1}{T_d}\left[\frac{1}{X_b}\left(\frac{P_{ecl}T_{ecl}}{X_n}\right)\right] + \frac{P_d}{X_d} \tag{5.10}$$

where T_d is the minimum daylight time; X_d and X_b are the solar array-to-loads and solar array-to-battery power transfer efficiencies, respectively; P_d is the average power required in sunlight. The solar array area is defined by the number and density of solar cells, which can be estimated as

$$N_c = P_{sa} / P_c \tag{5.11}$$

where P_c is the ideal power output of a single cell adjusted to EOL (End-of-Life) operational conditions. The ideal power P_L represents the solar-cell laboratory performance and it can be computed as

$$P_L = SA\eta \tag{5.12}$$

where S is the solar constant (~1353 W/m^2 outside of the atmosphere), η is the cell efficiency at the reference temperature and A is the solar cell area. The real value of the power (P_c) required to the solar array is, clearly, influenced by all the losses occurring in the generation process, as shown in Eq. (5.13)

$$P_c = P_L(\eta_{rad}\eta_{uv}\eta_{cy}\eta_{ad}\eta_{con}\eta_t) \tag{5.13}$$

where

η_{uv}, power loss due to UV radiation

η_{cy}, power loss due to thermal cycling

η_{ad}, power loss due to assembly and design

η_{cont}, power loss due to contamination from all sources

η_{rad}, power loss due to radiation damage

η_t, power adjustment for operating temperature

The area of the solar array, A_{sa}, can be estimated as the ratio of the number of cells and the value of the density of solar cells. Finally, the total mass of solar array can be computed as the sum of the mass of the solar array, assuming typical values of density, and the mass of the power control electronics and of harness (estimated as 30% of the total mass [104]).

Table 28 shows results of the preliminary sizing of the solar array for each scenario, assuming typical values for all the relevant losses.

Table 28 Preliminary sizing of solar array

Item	**Scenario 1**	**Scenario 2**	**Scenario 3**
Minimum daylight time (minutes), T_d	74	90	90
Solar array-to-loads power transfer efficiency, X_d	0.80	0.80	0.80
Solar array-to-battery power transfer efficiency, X_b	0.85	0.85	0.85
Eclipse Power Requirement (W)	505	818	2.96
Daylight Power Requirement (W)	75	107	9.71
Total Power Requirement (W), P_{sa}	580	925	12.6
Solar array estimated area (m2), A_{sa}	3.38	5.4	0.12

Table 29 lists the battery and solar array sizing for the passive satellite of Scenario 1 and Scenario 2.

Table 29 EPS budget for the passive satellite

Item	**Scenario 1**	**Scenario 2**
Li-Ion Battery Mass (kg)	1.20	1.60
Solar Array Area (m^2)	0.72	0.89

The EPS sizing, in terms of computed mass budgets, will be given in Section 5.3 where the specific hardware for battery and solar array will be defined.

5.2.4 Thermal Control

To provide heat dissipation during SAR operations, the Thermal Control Subsystem (TCS) can be conceived with the radar RF unit installed in direct contact with a thermal radiator.

The preliminary sizing of the radiator is typically performed to estimate the heat rejection Q_w, that is the waste heat rejected by the radiator in watts, if the radiator of a given area A_R operates at a given equilibrium temperature T, or, conversely, to compute the radiator surface needed to reach a given equilibrium temperature. The following thermal balance equation can be used [104]

$$\alpha_s S\cos\theta + \frac{Q_W}{A_R} - \sigma\varepsilon_{IR}T^4 = 0 \tag{5.14}$$

where S is the solar constant, α_s is the solar absorptivity, θ is the angle between the surface normal and the solar vector, σ is the Stefan-Boltzmann constant, $5{,}67\times10^{-8}W/(m^2K^4)$.

If SAR operations are assumed to be performed during eclipse time, the radiator surface can be computed as:

$$A_R = \frac{Q_w}{\sigma\varepsilon\mathrm{T}^4} \tag{5.15}$$

Assuming, as reference, a total heat generation of 800 W for the transmitting microsatellites of Scenario 1 and Scenario 2, and 30 W for the passive nanosatellite of Scenario 3 and using typical optical properties of space radiators (i.e., absorbance 0.2 and emissivity 0.8), the surface of radiator needed to keep the temperature of radiator within a limiting temperature of 50 ° can be computed. In general, the overall mass of the thermal control system is typically in the range 2-5% of the dry mass [105]. Table 30 resumes the computed values for each scenario.

Table 30 Results of preliminary sizing of thermal control

Item	**Scenario 1**		**Scenario 2**		**Scenario 3**
	Tx/Rx	**Rx-only**	**Tx/Rx**	**Rx-only**	
Surface of radiator m^2, X_d	1.6	0.06	1.6	0.06	0.01
Mass of the thermal control (kg)	8.5	2.4	8.5	0.06	0.50

5.2.5 Attitude Control System

The attitude control requirements can be expressed in terms of torque and angular impulse capability of the satellite.

The torque capability must be computed after transient events (such as satellite separation) and during maneuvers and nominal conditions (no transients). The former can be computed using the following simplified equation [105]

$$T_q = \frac{1}{2}\omega_T{}^2\left(\frac{I}{\theta_{\max}}\right) \tag{5.16}$$

where ω_T is the tip-off angular rate, I is the spacecraft moment of inertia, and $\theta_{\max}$ is the maximum desired attitude rotation. Concerning the attitude control in nominal conditions and during maneuvers, the torque can be estimated as

$$T_q = I\frac{\Delta\theta}{2\Delta t^2} \tag{5.17}$$

where $\Delta\theta$ represents a change in the orientation in a prefixed time interval Δt. The angular impulse capability can be obtained using the simplified equation as in [105]:

$$h = I\omega_{man} \tag{5.18}$$

where h is the angular momentum capability and ω_{man} is the angular velocity during the attitude manoeuvre. Of course, an equal and opposite angular momentum is required to stop the manoeuvre. For the Scenario 1 and Scenario 2, the moments of inertia are computed by using a simplified satellite model, i.e., cube-shaped main body plus planar surfaces for antenna and solar arrays, as shown in Figure 36.

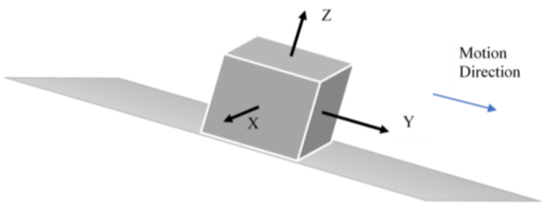

Figure 36 Cube-shaped satellite used as reference for the inertia properties determination

For the Scenario 3, instead, a parallelepiped of mass of 10 kg and dimensions of 30x20x20cm is taken as reference for the inertia properties determination. Inertia moments for the three scenarios are listed in Table 31.

Table 31 Inertia properties

Item	Scenario 1	Scenario 2	Scenario 3
Inertia moment (x-axis), kgm^2	111	111	0.65
Inertia moment (y-axis), kgm^2	23	23	0.65
Inertia moment (z-axis), kgm^2	102	102	0.40

To determine the required on-board attitude control capability, this procedure has been applied:

- The transient torque capability is computed by imposing a tip-off rate of 0.1°/s and a maximum angular excursion of 10°, considering the maximum inertia moment for conservativeness.
- The manoeuvre torque capability is instead computed assuming a 20° change in the attitude with an angular rate of 0.1°/s for the manoeuvre.
- The angular momentum capability is estimated by computing the angular impulse required for manoeuvring the spacecraft around the roll axis and considering a 0.1 °/s rate.

Table 32 is a summary of control capabilities estimated values.

Table 32 Control capabilities

Item	Scenario 1	Scenario 2	Scenario 3
Transient Torque capability (Nm)	10^{-3}	10^{-3}	$5\ 10^{-6}$
Maneuver Torque capability (Nm)	10^{-3}	10^{-3}	$5\ 10^{-6}$
Angular momentum capability (Nms)	0.2	0.2	$11\ 10^{-3}$

Finally, mass and power budgets for Attitude control system (ADCS) can be performed assuming reference hardware fulfilling the control requirements, as described in Section 5.3.

5.2.6 Propulsion system

Propulsion system is sized considering the total ΔV for orbit control. The orbit control can be absolute or relative. Absolute orbit control is required to enable the satellites to stay within a fixed tube around a predefined Earth-fixed reference orbit. This ensures high ground-track repeatability and similar data-take conditions.

On the other hand, relative orbit control is required for formation acquisition, maintenance, and reconfiguration. The only scenario requiring ground-track repeatability for interferometric applications is the Scenario 2. Indeed, the satellite system of Scenario 2 shall provide single-pass multi-baseline interferometry capability requiring high ground-track repeatability for interferometric acquisitions. For the other scenarios, instead, relative orbit control is sufficient.

Hence, the sizing parameter for the propulsion system is the total ΔV required for absolute and/or relative orbit control maneuvering, that determines the mass of the propellant, see Eq.(5.19). To this mass, the mass of thrusters, tank and additional hardware must be added.

The propellant mass can be estimated considering the total ΔV and the specific impulse, using the rocket equation (g is the gravity acceleration and m_{sat} is the satellite total mass)

$$m_p = m_{sat}\left(1 - e^{-\frac{\Delta V}{I_{sp} g}}\right) \qquad (5.19)$$

For formation acquisition, maintenance and reconfiguration maneuvers, a total ΔV of about 100 m/s and a specific impulse of 235 s, based on PRISMA mission example [15], can be taken as reference for the Scenario 1 and Scenario 2. For the Scenario 3, the CanX-4&5 mission [40], can be assumed as reference, with a total ΔV of about 18 m/s and a specific impulse of 45s. Table 33 resumes all the assumed values.

Table 33 ΔV for relative orbit control and specific impulse

Item	**Scenario 1**	**Scenario 2**	**Scenario 3**
ΔV for relative orbit control, m/s	100	100	18
Specific impulse, s	235	235	45

For absolute control orbit, considering that the system of Scenario 2 is flying in a sun-synchronous repeat orbit at 528 km altitude, the most important disturbance forces acting on the satellite is the atmospheric drag. Neglecting any variation in the inclination of the orbit, the effect of the atmospheric drag is a semimajor axis decay, that, in combination with Earth rotation, causes a change in the ground-track. So, to ensure ground-track repeatability, this effect must be considered to compute the required ΔV for the correction maneuvers.

Specifically, the following equation can be taken as reference for a rough estimate of the total ΔV

$$\Delta V_{tot} = \Delta V_{man} N_m \tag{5.20}$$

where ΔV_{man} is the ΔV for a single maneuver, and N_m is the total number of maneuvers during all the lifetimes given by

$$N_m = \frac{l_t}{\tau_m} \tag{5.21}$$

with l_t being the lifetime and τ_m being the period between two successive maneuvers. The time interval τ_m can be computed as [106]

$$\tau_m = -\frac{2\Delta a}{\frac{da}{dt}} \tag{5.22}$$

where Δa is the variation of the semi-major axis with respect to its nominal value for which corresponds a radial component of space error in orbit [106], E_R, of

$$E_R = \Delta a + r\Delta e_x \cos(u) + r\Delta e_y \sin(u) \tag{5.23}$$

with r being the norm of position vector, Δe_x and Δe_y are the component of variation in the eccentricity, respectively. Specifically, E_R corresponds to the maximum allowed deviation of the satellite from the reference orbit, that defines the radius of the control orbital "tube". Based on TerraSAR-X example [106], it is imposed a radius for the control tube of 250 m. Assuming no changes in Δe, and imposing E_R equals to 250 m, Δa can be estimated as 250 m. The semi-major axis decay rate, assumed to be constant, is given by

$$\frac{da}{dt} = -\rho \mathrm{B}\sqrt{\mu a} \tag{5.24}$$

where B is the ballistic coefficient, ρ is the atmospheric density, and μ = 398600.4415 km^3/s^2. Based on mass and volume estimates, (see Section 5.2.2) a ballistic coefficient of 0.022 m^2/kg can be obtained; applying orbit characteristics, listed in Table 22, a semi-major axis decay rate of about 10 m/day, and consequently, from Equation (5.24), a value for τ_m of about 50 days.

Finally, for a 3-years lifetime mission, a total number of maneuvers, N_m, of 22 is obtained. Using a rough estimate of 1 m/s for the ΔV_{man}, computed as in [107], a total ΔV for absolute control orbit of about 30 m/s is obtained. Thus, the total ΔV for both absolute and relative orbit control for the Scenario 2 is 130 m/s. With equation (5.19), the mass of the propellant system for the three scenarios can be computed, as indicated in Table 34.

Table 34 Mass of propellant

Item	**Scenario 1**	**Scenario 2**	**Scenario 3**
Mass of propellant (kg), m_p	7	9	0.4

The mass of the tank can be conservatively estimated as about 50% of the propellant mass, i.e. about 3.5 kg and 4.5 kg for Tx/Rx satellites of Scenario 1 and Scenario 2, and 0.2 kg for the passive platform of Scenario 3. Adding 2 kg and 0.5 kg for additional hardware (lines, valves, and thermal control hardware) for Scenario 1-2 and Scenario 3, respectively, the computed estimates of propulsion system mass are listed in Table 35.

Table 35 Mass of propulsion system

Item	**Scenario 1**	**Scenario 2**	**Scenario 3**
Mass of propulsion system (kg)	12.5	15.5	1.1

Finally, the estimates for the Rx-only satellites of Scenario 1 and Scenario 2 are resumed in Table 36.

Table 36 Mass of propellant for Rx-only satellites

Item	**Scenario 1**	**Scenario 2**
Mass of propellant (kg), m_p	4	6
Mass of propulsion system (kg)	6	11

5.2.7 Telecommunication and Data Handling

To exchange navigation and status data, dedicated Inter Satellite Links (ISL) channels are required, which typically exploits UHF or S-band. ISL is a key technology for formation flying applications, that must face the challenges reported in Table 37.

Table 37 ISL challenges in FF-SAR system

Item	**Description**
Availability	In highly dynamic formation flying scenarios ISL has to be permanently available.
Latency	For real-time critical operations, such as manoeuvring and relative positioning, ISLs need to provide low latency communications.
Reliability	ILS must be robust to hardware failures and ensure very low Bit Error Rates (BER)
Synchronization	Synchronization among the satellites is crucial to ensure that the platforms can coordinate and cooperate. In this concern, LEO missions may rely on absolute time references provided by external GNSS systems (e.g., GPS, Galileo) and ISLs could make possible to share clock information between the platforms.

For what concerns data handling, the main critical aspect is related to the high data volume collected during SAR operations. The procedure described in [91] is used to compute data volume and data rate. Considering the swath width, W_g, and the incidence angle η, the required minimum slant range width is approximately

$$W_s \approx W_g \sin\eta \tag{5.25}$$

The corresponding data sampling window is

$$\tau_w = 2 \cdot \frac{W_s}{c} \tag{5.26}$$

The number of samples per range line can be determined as

$$N_s = f_s \cdot t_w \tag{5.27}$$

in which f_s is the sampling frequency computed as $f_s = 1.2\,B$, with B being the bandwidth of the transmitted pulse. The number of bits for each sample can be computed by considering the quantization factor, n_{bit}, as

$$N_{bitsample} = N_{sample} \cdot n_{bit} \tag{5.28}$$

The required data rate will be

$$datarate = N_{bitsample} \cdot PRF \tag{5.29}$$

while the data volume is

$$datavolume = dutycycle \cdot PRF \cdot N_{bitsample} \tag{5.30}$$

Table 38 resumes the computed data rate and data volume for each scenario.

Table 38 Estimates for data rate and data volume of each scenario

Parameter	**Scenario 1**	**Scenario 2**	**Scenario 3**
PRF (kHz)	3.5	4.5	1.8
Swathwidth (km)	35	50	100
Incidence angle (deg)	30	45	40
Bandwidth (MHz)	100	100	80
Duty Cycle per orbit (%)	5	20	2
Data volume - per orbit (Gb)	7	2	0.8
Data rate (Mbps)	200	108	56

5.3 Hardware selection

Based on the required performances defined by the former analysis, a market analysis has been performed for identifying hardware instrumentation and components for each satellite subsystem. The selected hardware components are present in missions that have already flown successfully or are in the development phase. As stated before, no assessments have been made at this level regarding the interfaces between the different subsystems and the compatibility between the different components.

SAR payload

For the Scenario 1 and Scenario 2, involving micro satellites, the small SAR system compatible with 100 kg class satellite described in [49] is assumed as reference. This system consists of a deployable passive, honeycomb planar antenna, and a Radio Frequency (RF) equipment, based on commercial solid state Gallium Nitride High Electron Mobility Transistors (GaN HEMT) power amplifiers, installed within the satellite main body. As outlined in the previous sections, the overall mass of this system, on-board the Tx/Rx satellite, is estimated to be around 45 kg. Instead, SAR instrument mass reduces to about 32 kg on board the receiving-only satellite. For the Scenario 3, involving passive CubeSat platforms, the SAR specifications of CIRES mini-radar payload [36] have been taken as reference. The radar fits within 1.5U volume and consists of three modules: 1) power amplifier; 2) radar transceiver (TX/RX); and 3) high speed processor and recorder (see Figure 37). The peak power demand is about 600 W in the Tx mode, with an average power requirement of 60 W and 10% of duty cycle. In the Rx mode, the radar requires an average power of 5W.

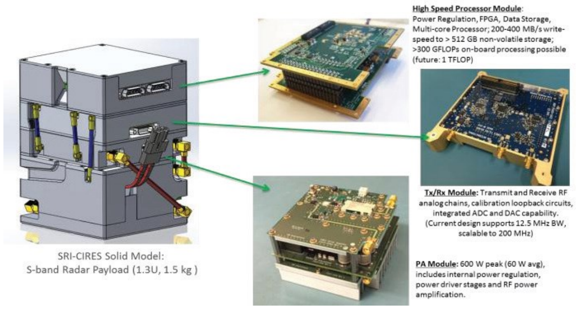

Figure 37 SAR CIRES-payload [36]

Electrical Power Subsystem

The preliminary sizing of battery performed in Section 5.2.3 has resulted in a total energy to be stored in the battery of

- Scenario 1: 3740 Wh
- Scenario 2: 4173 Wh
- Scenario 3: 5.80 Wh

For the Scenario 1 and Scenario 2, the Saft Li-ion cells [108] can be taken as reference (see Figure 38). The battery has specific energy of 165 Wh/kg, high energy efficiency of 97% for reducing the charge power, high-level of modularity and configurability, and strong compatibilities for small satellite applications.

Figure 38 Saft Li-Ion battery [108]

For the Scenario 3, one GomSpace Nanopower BP4 38Wh battery [109] (see Figure 39) could be used to accommodate the power requirements during eclipse phases and SAR operations. This battery weights 270 g with physical dimension of 93 x 87 x 23 mm (i.e. about 0,2 U).

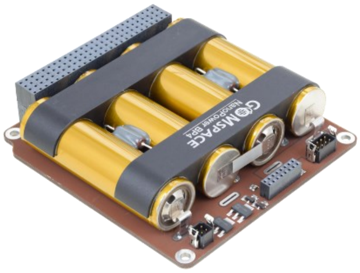

Figure 39 GomSpace Nanopower BP4 [109]

Table 39 resumes the computed masses of the battery for the three scenarios.

Table 39 Battery masses

Battery Mass (kg)	**Value**
Scenario 1	22.6
Scenario 2	25
Scenario 3	0.27

For what concerns solar array technology, for the Scenario 1 and 2, it is assumed a solution based on Honeycomb with Carbon Fiber Reinforced Polymer with a density of 2 kg/m^2. Recalling the computed estimated solar array area (see Table 28), i.e., 3.38 m^2 for Scenario 1 and 5.2 m^2 for Scenario 2, the solar array masses are 6.76 kg and 10.4 kg, respectively. To this mass, the mass of the power control electronics and of harness, estimated as 30% of the solar array mass, must be added. The total mass is thus, 8.79 kg for Scenario 1 and 13.52 kg for Scenario 2. For the Scenario 3, the selected solar cells are the Azurspace 3G30C [110], with a 30% efficiency, an area of 30 m^2, and an average weight of 50 mg/cm^2. Considering the estimated solar array area of 0.12 m^2, a mass of 300 g can be obtained. The final estimates for the EPS sizing are given in Table 40.

Table 40 Final budgets for EPS sizing

Item	**Scenario 1**	**Scenario 2**	**Scenario 3**
Li-Ion Battery mass (kg)	22.6	25	0.27
Solar Array Mass (kg)	8.79	13.52	0.3
Electronics, Harness (kg)	2.02	3.12	-
Total Mass (kg)	31.39	38	0.57

Finally, Table 41 lists the EPS sizing for the passive satellite of Scenario 1 and Scenario 2.

Table 41 EPS budgets for the passive satellite

Item	**Scenario 1**	**Scenario 2**
Li-Ion Battery Mass (kg)	1.20	1.60
Solar Array Mass (kg)	0.81	1.78
Electronics, Harness (kg)	0.62	1.01
Total Mass (kg)	2.68	5.28

Attitude Determination and Control System

For the Scenario 1 and Scenario 2, as example of candidate technological solutions, the following space-qualified hardware components have been selected, satisfying both the estimated attitude control requirements listed in Table 32, as well as the attitude determination requirements:

- High-accuracy during SAR operation by star-sensors, as the star-tracker ST-200 [111] manufactured by Berlin Space Technology, with an accuracy of 10 arcseconds, a mass of 0.05 kg, and a power consumption of 0.22 W.
- Attitude acquisition and sun pointing by sun and magnetic sensors, as the ones manufactured by Sitael [113], with an accuracy up to 0.01°, a mass of 0.24 kg, and power of 0.05 W.
- High accuracy pointing and adequate slewing capability for target pointing by reaction wheels, as the ones designed and manufactured by Blue Canyon Tech [112], with a Max.Torque of 0.025 Nm and Max. angular momentum of 0.5 Nms. The mass and power are 2.25 kg and 9 W, respectively.
- Initial acquisition of attitude and wheel unloading operations by magnetic torquers, as the SSTL MTR-5, with a mass of 1.5 kg and power of 1.5 W.

For the Scenario 3, the integrated unit XACT-50 [114] (Figure 40) can be assumed as reference for the ADCS. Manufactured by Blue Canyon Tech. company, this unit consumes 12 W in nominal operation with very precise attitude knowledge, providing pointing accuracy of 0.007°, momentum capacity of 50 nMms, satisfying the requirement listed in Table 32, and a slew rate of 10 deg/s. Designed specifically for CubeSat applications, the unit fits in about 1U volume, with a mass of 1.23 kg.

Figure 40 X-ACT 50 integrated ADCS module [114]

Hence, ADCS mass and power budgets for each scenario are obtained and listed in Table 42.

Table 42 ADCS mass and power budgets

Item	Scenario 1	Scenario 2	Scenario 3
ADCS total mass (kg)	5.6	5.6	1.23
ADCS total power (W)	18	18	12

Propulsion system

As stated before, for the Scenario 1 and Scenario 2, the propulsion system of the PRISMA mission [15] is taken as reference. In the PRISMA mission, the chief satellite is equipped with the HPGP (High Performance Green Propulsion) propulsion system (see Figure 41), an environmentally friendly and non-toxic chemical propulsion system (using a green propellent, as AND-based LMP-103S, Ammonium Dinitramide) developed by ECAPS [115], equipped with two 1N thrusters, 5.6 kg of propellant and delivering a total ΔV of 60 m/s.

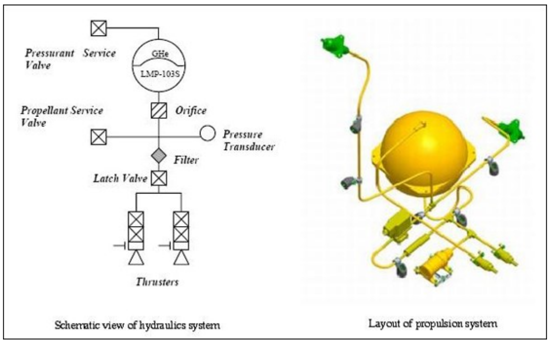

Figure 41 HPGP propulsion system [115]

For what concern the Scenario 3, the reference propulsion system is the Canadian Nanosatellite Advanced Propulsion System (CNAPS) [42], which had provided the two CanX-4&5 satellites with propulsive capabilities for orbit acquisition, station keeping, formation control and reconfiguration. CNAPS is a liquid cold-gas thruster system capable of delivering a total ΔV of approximately 18 m/s while consuming only 0.25 W of power, with a volume of 2U. Figure 42 gives a representation of the CNAPS. The propulsion system uses liquid hexafluoride as propellant, stowed in two tanks of 260g with four thrusters to provide a specific impulse of 45 s.

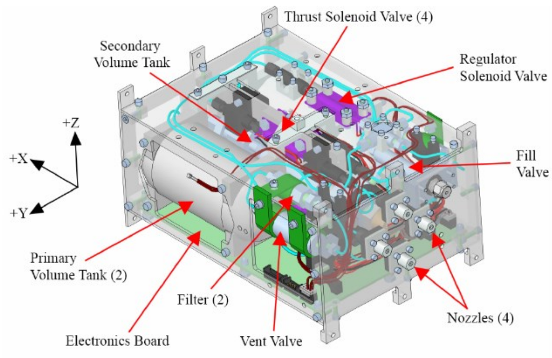

Figure 42 CNAPS propulsion system [42]

Telecommunication

As inter-satellite communication system and data downlink terminal, the S-Link system [116], composed of a S-band transceiver developed for micro and nanosatellites, is assumed for Scenario 1 and Scenario 2. For such equipment, it is possible to conservatively assume 1-kg mass and 10-W peak power consumption. The technical characteristics of S-Link system are reported in Table 43.

Table 43 S-Link technical characteristics [116]

Item	**Value**
S-band operation	2025-2300 MHz
Data rate Sat2Groun	0.6 – 4.0 Mbps
Data rate Ground2Sat	30 – 200 kbps
Data rate Sat2Sat	27 – 150 kbps
Operational mode	TDD – semi-duplex
Power consumption	3 – 4.5 W/ 8-12 W
DC supply voltage	7 – 18 V
Volume	65 x 65 x 137 mm^3

To satisfy the data rate requirement listed in Table 38 for transmitting the payload data to the ground station, the Surrey-manufactured X-band transmitter and data recorder [117] is taken as reference (Table 44) for the mass and power bus estimations.

Table 44 Power and mass of X-Band transmitter and data recorder

Item	Power	Mass
X-Band transmitter	55 W	4 kg
Data recorder	5 W – 15 W	1 kg

Such equipment is completed by an antenna and the related pointing mechanism, with a weight of 2.7 kg and a power consumption of 3.4 W. So, the overall downlink unit has a mass of 8.4 kg and a power consumption of about 80 W.

Finally, the embarked flight computer is the one typically used in LEO missions. It is a high-performance low-cost single board computer with mass 1.5 kg, power consumption 10 W, size 306x167x30 mm, that can support several protocols (e.g., MIL-STD-1563, SpaceWire, CAN-SU) [118].

For the ground and intersatellite links of Scenario 3, one can select the NanoCom-SDR (Figure 43) developed by GomSpace [119]. This is a space qualified software defined radio (SDR) equipped with Tx/Rx channels, a mass of about 300 g and power consumption of 4 W. The system can accommodate high data rate in S-band and kilometric intersatellite communications. In recent times, indeed, there is a trend followed by CubeSat developers to use software defined radio (SDR) [120]. This technology represents a great setting for small platforms, relying on simple RF electronics and efficient software with low power consumption. SDRs use Field Programmable Gate Arrays (FPGA) to enable multiple bands and modulation schemes, with high flexibility and without significant change to hardware. Moreover, they can be programmed in flight directly from the ground [120]. Table 45 resumed the NanoCom-SDR characteristics. To ensure high relative position knowledge accuracy, the spacecraft must be equipped with GPS receivers, as the ones manufactured by NewSpace Systems [121].

Figure 43 NanoCom-SDR [119]

These sensors can accommodate high position and velocity accuracy requirements, as well as accurate determination of orbital position [121].

Table 45 NanoCom-SDR and NewSpace GPS characteristics

Item	NanoCom-SDR	NewSpace GPS
Mass	300 g	110 g
Volume	0.3 U	0.1 U
Power	4 W	3 W
Performances	Data rate: up to 225 Mbps	Relative positioning (1-sigma): <1 cm

5.4 Budget tables

Based on the former analysis, the mass budgets for the Scenario 1 and Scenario 2 listed in Table 46 and Table 47 confirm the feasibility to use satellite in the class of microsatellites (under 200 kg).

Table 46 Mass budgets of Scenario 1

Subsystem	Tx/Rx	Rx-only
Electrical Power System	10-22	3
Attitude & Orbit control	5	5
Propulsion (with propellant)	11-13	9-11
Telemetry & Command	1	1
On-board Data Handling	3-8	3-8
Thermal Control System	2-5	2-5
Structure	15-20	10-14
Bus Total	47-74	33-46
SAR	45	32
Total Wet Mass	92-119	65-78
Estimated Range	90-120	60-80

Table 47 Mass budget of Scenario 2

Subsystem	Tx/Rx	Rx-only
Electrical Power System	43	6
Attitude & Orbit control	5	5
Propulsion (with propellant)	17.5	13
Telemetry & Command	1	1
On-board Data Handling	10	10
Thermal Control System	9	6
Structure	42	30
Bus Total	140	80
SAR	45	32
Total Wet Mass	170	114

The feasibility to use a CubeSat platform for the mission of Scenario 3 has been confirmed by mass, power, and volume budgets listed in Table 48.

Table 48 Final budget for Scenario 3

Subsystem	Mass (kg)	Power	Volume (U)
Structure	2.6		
Electrical Power System	1-1.3	1-1.3	1
Attitude & Orbit control	1.2-1.5	12-15	1
Thermal Control System	0.5-0.65	10-13	1
On-Board Computer	0.1-0.13	1-1.3	0.1
Communications	0.5-0.65	7-9.1	0.5
Antenna	2.5-3.2	-	3
Propulsion (wet)	1.5-2	5-6.5	2
SAR payload	1-1.3	5-6.5	1.5
Total Wet Mass	10.3-13	41-53	9-12 U

6. Spacecraft Modularity

Traditional approach for spacecraft design is highly dependent on the specific mission. If on one hand, this approach allows to optimize the platform to perform the tasks required from the mission, on the other hand, the time for the actual implementation of the space program, as well as, the production costs and general engineering complexities, tend to be very significant. This reduces the possibilities for small-medium companies and university consortia to start and finish their space programs, independently. A potential reversal of this trend was offered by the introduction of the CubeSat concept, which represented a revolution in the world of satellites. This concept, in fact, had introduced practical and innovative solutions for the creation of compact, economical, and flexible platforms. Being based on commercial-off-the-shelf (COTS) components, CubeSats are affordable for a wider audience of developers. Nevertheless, the techniques for the integration and the assembly of the various elementary units, known as CubeSat 1U units, are still based on the same design approach of larger conventional satellites. The different CubeSat components are, in fact, interfaced, controlled, and assembled in an integrated satellite system through relationships between functions and physical components very complex; the design is highly customized for the specific mission, with consequent difficulty in replacing a component without significant hardware and software modifications to the platform; the design logic is mainly sequential, with a strong interdependence between the different components. This approach makes it possible to achieve the maximum performance obtainable from platforms naturally characterized by modest performances, but it makes also the CubeSat a product of fine craftsmanship, a kind of "Swiss watch", designed ad-hoc for a single mission.

To make a substantial change and going beyond the CubeSat concept, a brand-new approach for satellite design must be introduced. In this sense, spacecraft modularity represents the most promising concept for revolutionizing the way a satellite is produced and developed. A modular platform can be obtained by quickly integrating and assembling a set of flexible and reusable basic modules, also called building blocks, into a single system using standardized interfaces based on universal protocols. Updates and modifications to the platform can be easily operated by replacing a single module with no major hardware/software changes needed. Already existing designs can be applied to different contexts for multiple missions, resulting in a significant decrease in the duration of the entire production cycle. Indeed, timeframes of several years of traditional space program can be reduced to few months. Non-recurring engineering (NRE), i.e., the one-time costs to research, design, develop and test a new product, can be dramatically cut. Finally, the overall complexity of the system can be lowered by decoupling the functionality of the single module from that of the overall system.

In this chapter, an overview of spacecraft modularity is given. The main differences between modular and traditional platforms are pointed out describing the philosophy behind the modular approach for spacecraft design. The plug-and-play (PnP) satellites are then introduced with an in-depth description of the Space Plug-and-Play Approach (SPA), a well-assessed plug-and-play model including a set of conventions to rapid integrate a platform, e.g. standard interfaces, self-description by Electronic DataSheets (EDS) embedded within the components, automatic discovery of a component when plugged into system, the use of middleware software, standardized and reusable modules. Finally, some examples of real SPA applications are briefly described.

6.1 Bus architecture

There are three main types of architectures available for the bus of a small satellite [122]:

- Traditional bus
- Common bus
- Modular bus

Traditional architecture is, today, the most widely used architecture to produce a satellite at any scale, including micro and nano satellites. It offers the best performances, the possibility of optimizing costs in the short-term, and a fine tuning of the platform with respect to the specifications required by the mission in question. It is characterized by complex interfaces and low levels of commonality, adaptability and reconfigurability of the systems. For these reasons, a platform based on traditional bus si a *one-of-a-kind* platform, developed ad-hoc for a single mission [122].

The architecture based on a common bus represents an integrated architecture used "with eyes closed" several times in different missions. If this allows to minimize development costs and times, the changes allowed to the platform between different missions are minimal and, consequently, the family of compatible missions is very limited.

The modular architecture is a bus built by assembling a set of basic modules, flexible and easily integrated with each other, thanks to the use of standard interfaces and little or no interdependence between the different components. This enables to obtain different final products using common modules for different applications and multiple missions.

Table 49 summarizes the characteristics of the three types of architecture.

Table 49 Main characteristics of traditional, common, and modular buses.

Parameter	**Traditional bus**	**Common bus**	**Modular bus**
Fixed costs	High	High	Mid
Initial costs	High	High	High
Long-term costs	High	High	Low
Complexity	High	High	High
Flexibility	Low	Low	High
Scale of optimization	System	System	Module

6.2 Modular approach

Modularity is not limited to the integration of a set of basic modules in a single system. It defines also a series of design rules and universal standards, aimed at creating common mechanical, electrical, thermal and software interfaces, through which assembling the different modules in a single system with simple and repeatable operations [123]. Unlike a traditional platform, where optimization focuses on the integrated system, in a modular architecture the weight of optimization is shifted on the individual component or module, which can be thus developed and tested independently from the other components. Each module (in a spacecraft represent a subsystem, as attitude control, communications, and power), is then classified as a common or independent module, depending on the specific function it can perform in the satellite. Common module can be used in all cases the required functions and performances are compatible with the characteristics of the module itself. It can be easily updated and/or replaced with other modules performing the same function, suitably scaled to meet the requirements of mission. Independent modules, instead, are modules which are non-dependent by other modules, as payload. The key elements of a modular platform are summarized in Table 50.

Table 50 Key elements of modular platform

Parameter	**Description**
Commonality	High level of hardware/software commonality for supporting different missions by using the same modules
Standard interfaces	Universal standards to be able to interface the different modules easily, minimizing the need for ad-hoc changes
Functional indipendence	Separation between different specific functions, one-to-one relationships between components and functions, ability to independently test each subsystem in a process based on a parallel logic

Despite all the potential advantages, the main limitations of modularity are

- Cost to achieve modularity: the initial implementation of the concept and the creation of a completely modular architecture require high initial investments.
- Quality of implementation: to reap all the benefits, high level of modularity implementation is required at each stage of the project.

The real advantage of using a modular approach comes with the possibility of using each module, in a flexible and simple way, many times in heterogeneous contexts. Being able to reapply the same design in different missions, the interval between the start of the platform design and its effective launch can be significantly reduced.

6.3 Plug-and-Play platforms

Plug-and-play satellites (PnP satellites) [124] are modular platforms in which the interfaces are exclusively based on open-source plug-and-play standards [125]. The basic logic is very similar to the one used in desktop computers [126].

The lack of a standard between the interfaces of the different subsystems in traditional satellites is, in fact, one of the main factors making the integration of a heterogeneous satellite system particularly complex. The plug-and-play approach defines a complete hardware/software model for the construction of a modular architecture [127]. The main features, as well as the key elements and fundamental operations to be performed in order to implement a plug-and-play architecture, are described in the following paragraphs.

6.3.1 Modular plug-and-play architecture

A plug-and-play architecture essentially represents an integrated network. Each component of the network is connected to a central data processing unit which can detect and recognize the single connected device, interconnecting all the modular components of the network [127]-[128]. Hence, each component can be treated as a black box that, once plugged into network, is interconnected to the other blocks, naturally carrying out its native function. The replacement or the use of the same block on a different platform can be performed in plug-and-play fashion, by defined and standardized interfaces and protocols, without the need to intervene several times on the platform by modifying the overall system. The main characteristics of a plug-and-play modular network are summarized in Table 51.

Table 51 Main characteristics of plug-and-play modular network

Characteristic	**Description**
Single-point interface connection	Use of a single connection point for power, data, and synchronization
Self-describing Self-Organizing Self-Discovery	The system must be able to dynamically configure and / or reconfigure itself when a component is added or disconnected (even in the event of a malfunction). Each component must automatically provide its "digital identity", in order to be easily recognizable when interrogated and to be visible within the network.
Communication through standard messages	Use of predefined messages for system / system, system / components and components / components communications.
Non-topological system	Functional independence of the component from the position in which it is connected
Abstraction from the specific component (sensor, actuator, etc.) used	Each component must be able to be treated as a black box, which, once plugged, is interconnected to the other blocks, naturally carrying out its native function.

The key elements of a plug-and-play network are

- Software middleware: central software acting as an intermediary between the various applications or hardware devices present in the network.
- Electronic datasheet: provides a complete description of the generic modular component.
- Hardware/software interface: bridge connection between the component and the rest of the modular network. It allows the device to interface with the physical port to which it is connected. The component datasheet is embedded within it.
- Modular devices/applications: hardware devices (reaction wheels, propulsion units, sensors, etc.) or software applications (control algorithms, telemetry, etc.), compatible with plug-and-play standards, performing the traditional functions of satellite bus.

Software middleware is the central element of a plug-and-play architecture. In order to guarantee modularity, this element must be able to self-configure and automatically identify each component connected to the network. If a component is disconnected, either voluntarily or accidentally (due to a malfunction, for example), the software must be able to reconfigure itself to include the missing component in the network. Specific logical address must be assigned to each component for uniquely identified it within the network. Another fundamental property of the central software is networking, i.e., the ability to create an integrated and dynamic network in which each component becomes visible and reachable by the others. In this regard, the software receives and stores the datasheet of each component within a single archive, manages any data requests, and connects every point of the network. End-to-end connectivity between two components is therefore possible thanks to the intermediation of the central software: a data consumer makes a request for data to the middleware which can detect the components as data provider compatible with the request of the data consumer. The middleware sends a list of components available at the time of the request to the consumer component. To manage and control each connected component, the software must include management software applications, creating a link and data transmission/reception layer between the controlled component and the rest of the network. Table 52 summarizes the fundamental services the middleware must offer to achieve plug-and-play modularity.

Table 52 Middleware services

Service	Function
Assignment of logical addresses	Assign a specific address to each component
Archive and management of electronic datasheets	Storage the datasheet of each component, understand the instructions contained therein managing any requests for a component
Management and control software	Management of the component, allows the exchange of data between the component and the system and vice versa.

The electronic datasheet (EDS) is a digital description of the component in which all the information necessary to describe the component are incorporated. Specifically, this includes:

- Requests (services and / or data) of the specific component
- Responses of the specific component to any requests
- Control schemes
- I/O and related associated messages
- A universal vocabulary of terms, names, units of measure, formats, variables

The hardware/software interface creates a communication between the physical component and the central data processing software. Native outputs of each canonical device of the satellite bus (data from a sensor, for example) are transmitted according to the specific electronic description contained in the datasheet and incorporated into the interface itself. To make the component compatible with plug-and-play standards, the interface must be able to perform the following operations:

- Store and transmit the datasheet
- Enable component-system, system-component communications
- Monitor the component status
- Power supply

Finally, modular device/application represents any hardware/software component that has been made compatible with the plug-and-play standard.

6.3.2 Space Plug-and-Play Approach (SPA)

As part of the "Operational Responsive Space (ORS) [129] study aimed to make space programs faster and more reactive, the Air Force Research Laboratory (AFRL) proposed the approach known as Space Plug-and-Play Approach (SPA) [130]. The main elements of a modular architecture previously described, assume the following specific nomenclature within the SPA model [131]:

- Extended Transducer Electronic Data Sheet (XTEDS) is the electronic datasheet fully describing each SPA component
- Applique Sensor Interface Module (ASIM) represents the hardware/software interface
- SPA Service Manager (SSM) is the software middleware

The capabilities and characteristics of SPA components are described in an integrated XML document called Extended Transducer Electronic Data Sheet (xTEDS), an extension of the IEEE 1451 TEDS [51] standard. The document includes both basic information provided by the component manufacturer, calibration data, an input/output description, and any request for component data [132]. As part of the self-discovery process, each component transmits its xTEDS to the SSM, which collects and stores all the information contained in the xTEDS. In this way, each component can transmit any data requests to the SSM which is able to dynamically identify compatible components within the network. Figure 44 shows a portion of the xTEDS code.

```
<DataMsg msgRate="1" msgArrival="PERIODIC" name="Temperature_Reading" id="1">
  <Variable units="counts" scaleUnits="seconds" scaleFactor="0.0001" name="SubS"
     kind ="subSeconds" dataType="UINT32"/>
  <Variable units="s" name="Time" kind="time" dataType ="UINT32" />
  <Variable name="Temperature" kind="temperature" id="1" dataType="FLOAT32"
     accuracy="0.1" />
</DataMsg>
<CommandMsg name="SetLEDs" id="10" description="Set LED's To Bits 0,1,2">
  <Variable name="LED" kind="status" dataType="UINT08" />
</CommandMsg>
```

Figure 44 Example of xTEDS [132]

Any component, for which the XTEDS register is available, can be connected to a SPA network through an interface called Applique Sensor Interface Module (ASIM) [133]. The ASIM creates a connection between the physical component and the SSM software, transmitting the native outputs of each canonical device of the satellite bus, according to the specific electronic description contained in the XTEDS document and incorporated into the interface itself. The ASIM, moreover, oversees the conversion of specific data of the device into xTEDS messages and vice versa, the monitoring of the state of the component, and performing synchronization operations through an internal oscillator. The SPA Service Manager (SSM) represents the software middleware of a SPA system, including a set of software components that offer the basic services for the rapid integration of a satellite bus [133]. The basic services offered by the SSM are listed in Table 53. In a SPA system each of this service is performed by a specific element, as indicated in Table 53.

Table 53 Basic services of SSM

Service	**Element**
Assignment of logical addresses	Central Address Service (CAS)
Storage and management of electronic data sheets	LookUp Service (LS)
Management and control software	Subnet Manager (SM-X)

SPA network is based on a layered or stratified architecture, in which each layer provides a service for the upper layer and receives a service from a lower layer [131]. There are five principal levels: physical layer, that defines the standards for physical interconnections, the data link layer that enables communication between the component and the SPA system, the network layer that identifies and registers each component, the transport layer that creates connections between different points of the network, the application layer that allows the exchange of data between different components, and the performance of the native functions of each component.

The physical layer is made up of physical ports, called SPA-X subnet, connecting the hardware devices. The main tasks of a SPA-X subnet are: i) detecting the connected component, ii) receiving and sending messages. The X indicates the type of technology used as a communication standard. SPA currently supports the following technological interfaces [134]:

- SPA-1: based on the I2C standard, it is the simplest interface that requires less power but offers the lowest performance in terms of transmission speed

- SPA-U: based on the USB standard, it supports up to 12 Mbps in transmission and it is the widely used interface in SPA systems
- SPA-S: based on the SpaceWire standard, it can support up to 600 Mbps in transmission and can be used in combination with SPA-U interfaces thanks to an open architecture
- SPA-L: Based on an optical transmission standard, it supports transmission speeds up to 40 Gbps

The type of interface to be used must be selected taking into consideration the data transmission speed and bandwidth requirements of the component to be connected, but also the power demand of the interface used (see Figure 45). A satellite bus is made up of subsystems that require different performances and, consequently, it is difficult for a single type of interface to always satisfy the compromise between transmission speed and required power. Consequently, in a SPA network there are usually several interfaces working at the same time [131].

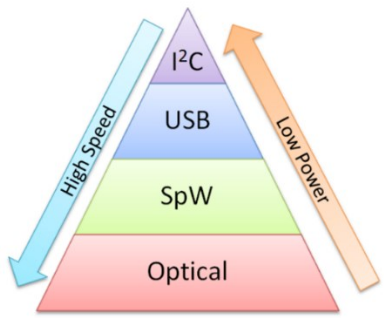

Figure 45 Bandwidth and power requirements trade-off [134]

Each SPA-X subnet has a related software component called SPA-X subnet manager (SM-X). This represents the management and control software element within the software middleware. The set of SM-X defines the data link layer, responsible for identifying the components connected to the subnet and routing data between the different elements of the network. The tasks of an SM-X are: i) identification of the component connected to the specific SPA-X Subnet for which the SM-X is the manager, ii) creation of a connection between the component and the network, iii) verification of the operating status of the component, iv) sending the component xTEDS and any messages and/or requests. The network layer is responsible for creating the SPA network, integrating each subnet into a single network. It provides the functions of i) logical addressing, i.e., assigning a specific logical address to each component, and ii) message routing, through which messages are transmitted over the network. Specifically, the logical addressing phase is coordinated by the Central Address Service (CAS). Precisely, CAS represents the fundamental service the middleware must be able to offer to ensure the operation of a plug-and -play. In a SPA network, the CAS assigns to each SM-X a 2-bit address, called SPA logical address (see Figure 46).

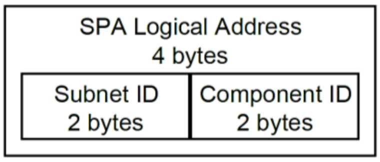

Figure 46 SPA Logical Address [131]

The Subnet Manager assigns, independently from the CAS, a 2-bit SPA Logical Address to each component connected in the Subnet of its competence. The purpose of the transport layer, instead, is to create end-to-end connectivity between the various SPA components. In this layer, the Lookup Service (LS) performs the registration of each component, when requested by the relative SM-X, and the storage of its xTEDS. The Lookup Service is a critical component in the SPA architecture, in charge of storaging all xTEDS registers, managing any component requests for data contained within the xTEDS code. It allows, for example, to identify a device or application that can provide the data requested by another component of the network, putting them in communication. Finally, the application layer is the upper layer in which each component performs its specific activities and functions.

The life cycle of a SPA component, when it is connected, can be summarized as follows: the component is discovered, a logical address assigning, xTEDS registration in the LookUp Service, data requesting to the SSM, subscribing to a particular data provider, and finally can perform the functions for which it is designed. Figure 47 shows an example of the architecture of a SPA network at the subsystem level, which envisages a certain number of nodes connected to each other. The nodes can be of three types: (1) endpoints, which correspond to the different subsystems of the bus; (2) multi-ported, which act as a router to create larger networks; (3) control, which act as hosts, i.e., the devices on which the SPA process control software [135] is installed.

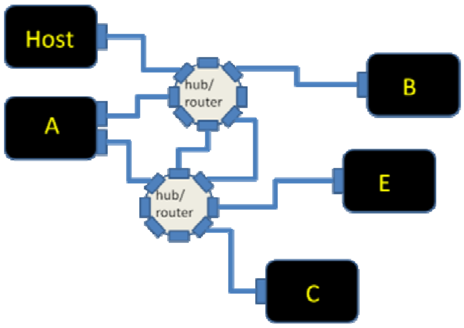

Figure 47 SPA network at subsystem level [135]

6.3.3 PnP CubeSat

The most promising technological solution for the large-scale implementation of the plug-and-play concept is the implementation of SPA technology for CubeSat design and development, i.e., Plug-and- Play CubeSat (PnP CubeSat) [136]-[137]. In addition of being compact, economical, and flexible, CubeSats have an inherently level of modularity platforms. Indeed, those platforms can be built with multiple stacks of 1U core units. Nevertheless, the platform design, as well as the integration and assembly of the different modules does not follow a modular approach, as described in the previous paragraphs, is still based on traditional philosophy. For example, the different modules are not designed to be interchanged and reused. A way to introduce plug-and-play modularity in CubeSats was proposed in [136], with the so-called nano-SPA concept, which is a plug-and-play architecture compatible with nano platforms. Specifically, it has been introduced the nano-modular format (NMF), consisting of a standard-sized face, 70 x 70 x 12.5 mm (Figure 48, left), designed to accommodate various SPA components. Like the denomination used for CubeSats (1U, 2U, 3U), the NMF faces are named 1 x 1 NMF, 1 x 2 NMF and so on. The dimensions are such that by assembling 6 x 1 NMF faces, a standard-sized 1U CubeSat is obtained (Figure 48, right).

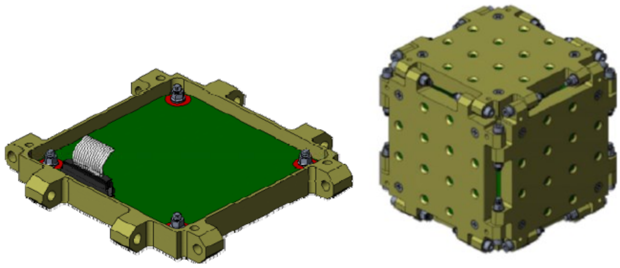

Figure 48 Nano Modular Format. Interior panel (left), 6 x 1 NMF faces realizing 1U CubeSat (right) [136]

A 1 x 2 NMF face can be used to create, for example, the long side of a 2U CubeSat, just as with a 1 x 3 NMF faces, it is possible to create a 3U CubeSat. Each NMF panel can be developed as an independent nano module, integrating, and assembling the different SPA components that make up the satellite bus individually, and then be connected to the other NMF panels in plug-and-play mode.

6.3.4 SPA examples

The SPA concept has been successfully applied in the construction of some fully modular satellites, including

- PnPSat
- QuadSat-PnP
- Trailbrazer

The PnPSat-1 and PnPSat-2 satellites (Figure 49) [54]-[55] are modular microsatellites, weighing around 180 kg, designed and developed using only SPA components, with SPA-U and SPA-S interfaces.

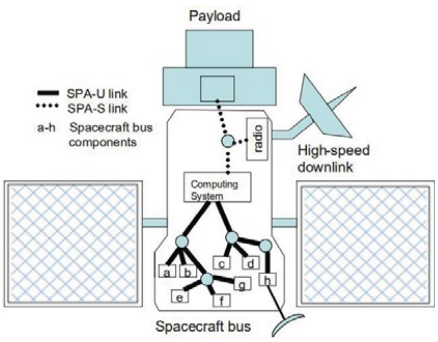

Figure 49 PnP Satellite

The architecture of each PnPSat can be divided into three parts (Figure 50):

- External case, which also constitutes the satellite structure, on which the various SPA components, the electric grid and the thermal control system are fixed
- Components of the satellite bus (software for autonomous flight, on-board computer, GNC modules and communications, etc.)
- Payload to perform a specific mission

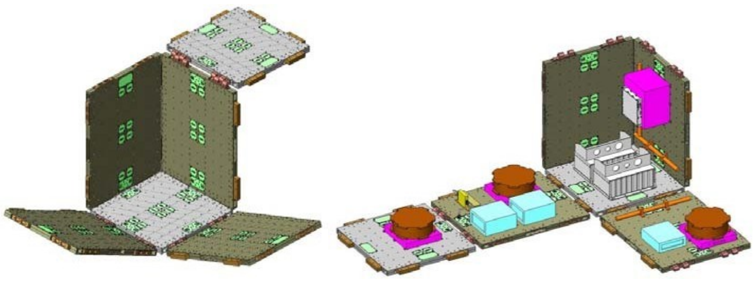

Figure 50 PnP Sat – External structure (left) and integrated satellite subsystems (right) [54]

QuadSat-PnP-1 (QSP-1) [138] represents the first nano-satellite made entirely with SPA plug-and-play components and interfaces, a model for future modular nano satellites. The QSP-1 architecture includes four "drawers", called trays, arranged one on top of the other like "pizza boxes" (see Figure 51). Four fixed solar panels are mounted on the structure, while the four trays contain the typical components of a spacecraft. The trays are made of aluminum, mechanically and electrically connected to each other, and divided as follows: (1) power tray, which contains the electrical power subsystem, the batteries and the OBDH system; (2) payload tray, in which a certain number of AIS receivers are housed; (3) communication tray, containing transmitters and receivers in S-band, L-band and UHF; (4) PnP tray, containing miniaturized components for power conversion, interfaces and SPA modules.

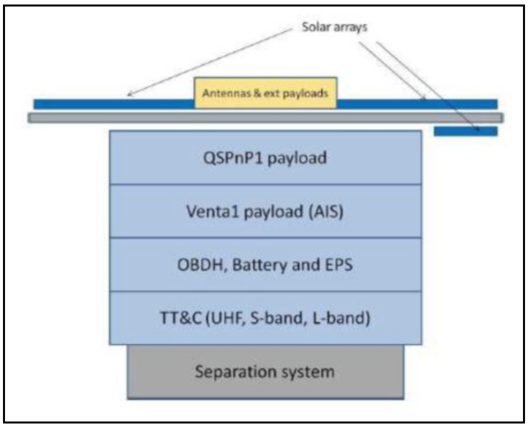

Figure 51 QSP-1 trays [138]

Trailbrazer (Figure 52) [139] is a CubeSat 1U built entirely with COTS components re-adapted to be compatible with the SPA standard and thus form a modular CubeSat based on a PnP network. The goal of the Trailbrazer mission was to demonstrate the possibility of converting COTS components into compatible SPA devices and to test their reliability and robustness in a space environment.

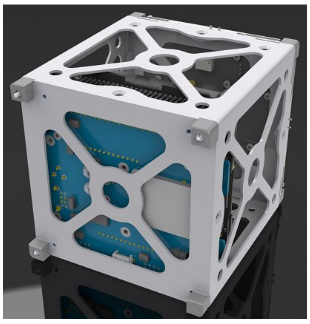

Figure 52 Trailbrazer 1U CubeSat [139]

Each component was equipped with SPA-U and SPA-S ASIM adapters. The structural envelope is made of standard size 1U 8051 aluminums with space for deployable antenna systems. The electric power system is made by Clyde space, and includes a 20Wh battery, six high efficiency solar cells, with dimensions compatible with a CubeSat 1U. The C&DH system, developed by Pumpkin, includes a motherboard and a pluggable processor, in which the SSM control software, for managing the SPA network, is inserted. A PMASS (Passive Magnetic Attitude Stabilization System) magnetic stabilizer is used to control the attitude of the satellite using the Earth's magnetic field, while an Astrodey Helium 100 radio and an ISIS deployable antenna make up the communications system.

6.4 Discussion

The SPA technology represented a great conceptual and technological advancement for the standardization of structural platforms, interfaces, communication protocols, and hardware components in spacecraft design. Anyhow, at present, SPA cannot be still considered a universal accepted standard. Indeed, SPA interfaces have not been certified yet by MIL or ECSS standards. Moreover, the space traditional industry seems to be unopened to adapt substantial changes in the use of new protocols and standards. That is why the future development trend of SPA technology could be completely different on the solutions proposed so far and described in the former sections. However, the fundamental SPA concepts SPA remains valuable for driving the transition of spacecraft design from a hardware-centric design to a data-centric one. These concepts are taken as reference guide for designing a modular attitude estimation software described in the next paragraph.

7. Modular Attitude Determination

The modularization of ADCS can be roughly defined as the problem to make the ADCS independent of any specific requirements dictated by the application in question. Instead, a modular ADCS must be able to fulfil the whole ADCS functionality for an entire set of heterogeneous missions.

In this chapter, a potential solution for the modular attitude estimation problem is discussed. The focus is mainly on the algorithmic side of the problem. The aim is to maximize the reusability by abstracting the estimation filter from the actual configuration of the sensor suite used in a particular mission. To this aim, filter equations have been parametrized to enable the use of the same algorithm in different mission contexts only by changing some parameters.

7.1 Modularization of ADCS

Different concepts must be considered to cope with the problem in question. First, the level and the type of modularization to be obtained. Basically, the principal ways to modularize the ADCS can be categorized into fully modularization at component level, partial modularization at subsystem level, cellularization, and combinations of these [64]. Each mode involves different architectures and requirements, with both advantages and disadvantages. A fully modularization, for example, means to treat each single ADCS component as an individual “black-boxed” module which is used in combination with other modules to perform standard ADCS functions. Each physical component is modularized by dedicated interfaces and connected with the rest of network by using standard messages and communications. The ADCS fractioning at component level results in great number of degrees of freedom, in terms of type, number and spatial locations of used hardware; in addition, this modularity enables the capability to meet mission requirements by adding or changing sensors and actuators to have higher performance [64]. However, the high-level of modularization to achieve coupled with the increased number of electrical and mechanical connections of the additional sensors and actuators make this type of modularization hard to realize. Moreover, the distribution of individual modules among different positions inside the platform may increase the delay between sensor measurements and the actuation of control laws.

Modularizing the ADCS at subsystem level, instead, implies that all the ADCS components are embedded in the same integrated unit. In this case, only the integrated module must be provided with standardized interface to be aggregated with other subsystem modules. This relaxes the general complexity of the system. Indeed, since the data to be processed come from a single fixed point of the network, the time delay is reduced, and the control software for data handling can be made simpler. In addition, the single connection point enables to significantly limit the mass overhead of cables, connectors, and interfaces. Clearly, the drawback of this type of modularity is a smaller flexibility. The designer, in fact, can select the whole integrated ADCS box with the hardware configuration fulfilling the specific mission requirements, but a selective modification of single ADCS element is not more possible.

Finally, the cellularization is based on a different philosophy for modularizing a space platform [140]. Each satellite subsystem is broken down into a fully-function cellular unit, very small in size and with limited performance. A certain number of these cellular units, performing the same function in the satellite bus, can be combined to obtain the required performance. Since many modules perform the same function, a failure of an individual module can be tolerated better or repaired faster, and the overall reliability of the system is increased. The design of a single cell is simplified by the reduced size of the module, and it can be applied for a wide number of different modules belonging to the same class. In this way, the entire system results less complex and more responsive with respect to a traditional system. Cellularization is mainly targeted to develop cellular reconfigurable spacecraft (CRS) [141], which are space platforms conceived to be easy to be reconfigured in orbit. CRS enables selective replacement of failed modules, platform adaptation to new mission tasks and requirements and fully automatization of assembly procedures. All these operations can be performed directly on orbit without the human intervention. Despite the powerful potentialities of this modularization technique, the complexity for realizing modular ADCS is further increased with respect to the other types of modularity. Indeed, the fully automatic reconfiguration of the modules is reflected on changing sensor, actuator, and system parameters. Sensor biases and misalignment factors, as well as inertia properties of the platform, could change when a module is dismissed or moved to different platform locations. Hence, an online estimation of these parameters is needed [64]. This, obviously, increases the general level of ADCS software complexity.

The second aspect for designing modular ADCS is the underlying network structure. The structure can be based on Application Programme Interface (API), network protocol level and middleware software. In this sense, the most viable option is the use of layered architecture based on a middleware software [64]. This structure, indeed, offers the possibility to create self-configuring and self-discovering network through publishing-subscribing operations. Strictly speaking, when plugged into the network, each component, or a whole integrated module, automatically provides its electronic data sheet through the embedded software running on the standardized interface. For an ADCS application, the standardized EDS must contain every information required to fully characterize the specific sensor or actuator. Thus, for a system where the modularization is made at component level, each sensor must provide the type of measurements (i.e., vector or line-of-sight measurements, quaternions), the data type and measurement unit, time model, scale factors and sensor biases etc., while actuator must send type and length of actuation, specific dimensions etc. The output messages must be based on a defined ontology in order to enable universal standardization [142]. On the contrary, for a modularization at subsystem level, a single electronic data sheet, providing fully description of all the integrated component in the ADCS box, can be sufficient.

The third aspect, probably the most important one, is the ADCS software. Generally speaking, the development of flight software can be considered as the most challenging and time-consuming task in the whole satellite design chain. For each satellite project, indeed, software must be tested, validated, and adapted to the requirements. Changing software codes, as well as writing new documentation, redefining design patterns, performing validation and testing again, developing a new architecture from mission to mission, are the leading causes for design complications, long development cycles, and high costs. The ADCS software, moreover, is in general the most complex and articulated part of the entire on-board flight software and thus the problem becomes particular evident for this subsystem. Hence, the need of modularizing the ADCS arises to save time and to lower the general complexity of the design. Two key features are essential for modular ADCS software: partitioning and reusability. A functional partitioning of the software, indeed, allows to break down the traditional ADCS algorithms, usually contained in a monolithic block, in many basic modules performing a single specific function, which can be easily activated or deactivated when necessary, depending on mission goals. In this way, the entire, complex, monolithic, one-designed traditional ADCS software becomes a combination of elementary building blocks, quickly reconfigurable and rearrangeable with minimal effort. Consequently, the reusability of the software results significantly increased for a variety of different mission settings, and this can help to save time and cost. According to *NASA Earth Science Data Systems – Software Reuse Working Group* there are different characteristics determining the reuse maturity of a software [143]. The level of reusability is quantified by the Reuse Readiness Levels (RRL), which spans from RRL 1, no reusability, to RRL 9, proven reusability [143]. The RRL is defined on the base of nine topic areas: Documentation, Portability, Extensibility, Portability, Intellectual Property Issues, Standards Compliance, Support, Validation/Testing, Modularity [143]. In the ambit of ADCS algorithms, the most prominent characteristics are extensibility and modularity. Extensibility enables to extend software functionality and the range of applications by adding or modifying new functions without changing the source code. In the ADCS software, this ability allows to accommodate different mission settings by modifying the value of specific parameters but using the same equations, and to incorporate easily new ADCS modalities. Modularity, instead, is targeted to maximize the separation of software in distinct modules, performing specific functions.

Another aspect the modular ADCS is dependent on is how sensor feedback and control algorithms are processed. In short, ADCS algorithms can run on module, global, or local level [64]. If the ADCS components are distributed among separated individual modules, each containing specific actuator or sensor, several instances of the algorithm can run on the dedicated module to control only the hardware available inside. In a centralized architecture, instead, the sensor suite sends the feedback to the central OBC which runs the algorithm using global system model and global controller. On the contrary, decentralized control architecture involves that all the ADCS algorithms run locally on the stand-alone module.

7.2 Methodology

With the above concepts in mind, a modular ADCS software has been designed to be implemented on board of Earth-pointing spacecraft in FF-SAR perspective. Platforms in the class of 12U CubeSat have been selected on the base of the preliminary design conducted in Section 5 and summarized in the final budgets of Table 48. A modularization at subsystem level has been selected, and consequently, stand-alone integrated ADCS boxes are considered to perform fully ADCS functioning. This choice was supported either by the relative high degree of simplicity of this type of modularization and by the number of integrated ADCS units already available on the market as COTS components for CubeSat applications (this number is continuously increasing). The software was designed to maximize flexibility and ease of applicability to different missions without a priori-knowledge of the actual configuration. The aim is to allow the user to choose the desired ADCS box only on the base of mission settings, pointing accuracy and control requirements, without further modifications of ADCS algorithms and no need of new testing and validation phases. This implies that software extensibility must be maximized to enable the use of software in "as is" conditions. To ensure the automatic discovery of sensors and actuators available in the box, a centralized middleware software is considered. All the mission specific parameters, instead, are contained in a dynamic database module, which is easy-to-edit from mission to mission. Finally, a partitioning of ADCS software at module level, where each module is subdivided into elementary sub-modules, is assumed to enable selectively switch among available software modules, activating or deactivating them when necessary.

The ADCS design problem can be formulated as follow. Assuming several reference missions with different determination and control accuracy requirements, the modular ADCS software must be able to fulfil complete ADCS functioning using always the same generic and reusable algorithms. Consequently, both the estimation of the spacecraft current state, at any desired time epoch, and the control to the desired state, must be performed with no prior information on the sensor and actuator set used in the specific mission. In this sense, ADCS algorithms must be "blinded" to the source of the information to be processed: attitude determination algorithms being only user of sensor solutions and not an integral part of the sensor itself, and attitude control algorithms implementing generic and adaptable control laws. Hence, the design must be targeted to maximize both the decomposition of the software in basic modules and the parametrization of equations. Since different boxes could be characterized by different hardware configurations, ADCS equations must be written without any dependencies on the type and number of sensors and actuators. The only hardware-dependent terms must be specific parameters (e.g., standard deviations of sensor measurement noise, diameter of reaction wheels, inertia properties) which can be easily tailored into the software and modified from mission to mission. Hence, standard ADCS models have been analyzed for identifying which parts of the model are directly dependent on the configuration and, once defined, generalized versions have been proposed to enable reusability. In practice, traditional ADCS models have already an intrinsic level of modularity. Indeed, a typical ADCS software developed in MATLAB/Simulink is very likely to be composed by several distinct modules as orbit propagator, ephemeris models, attitude estimation and control blocks, which have distinct functions. However, even if the software architecture is modular, the modularity here is applied only at structural level and not at a functional level. Indeed, algorithm modules are coded with a specific task in mind with low levels of parametrization; consequently, they may be not reusable if the task changes. Of course, same algorithms can be still used for different missions but only if strong similarities exist. In the next paragraph, a description of the proposed simulation architecture is given, highlighting non-modular parts of the used ADCS models with a mathematical description about the solutions proposed for modularizing them.

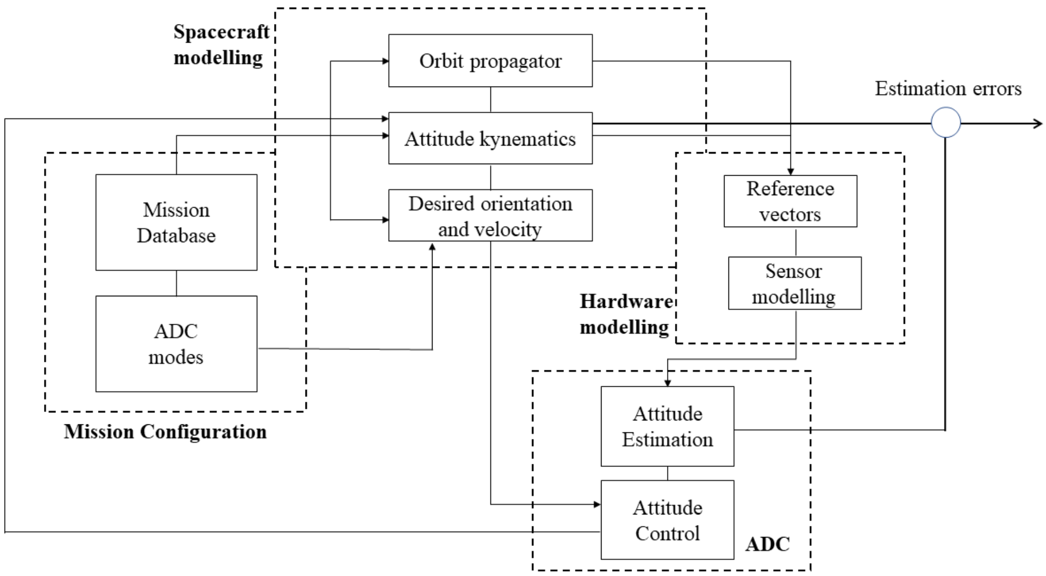

Figure 53 Simulator architecture

7.3 Generic and Reusable ADCS software

A simulator has been developed to test the validity of the proposed generic ADCS software. The simulation architecture is shown in Figure 53. Software decomposition is made in successive layered levels. First, there are groups of modules organized in cluster according to the common function. Each cluster comprises several modules to operate specific functions. Then, the modules are partitioned again into elementary sub-modules carrying out one specific task. There are four main clusters: spacecraft modelling, mission configuration, hardware modelling, and Attitude Determination Control (ADC) cluster. The mission configuration cluster is used to adapt the software for the desired setting. In this cluster, there is a mission database module where all parameters related to the specific mission and platform can be inserted, an ADCS modes module to switch among the required mode from mission to mission, or mission phases, and to activate/deactivate specific software modules. The spacecraft modelling cluster oversees the simulation of the satellite dynamics. This cluster is composed by an orbit module, used to propagate the orbit, an attitude dynamic module which propagates the attitude dynamics and kinematics, and a desired orientation and velocity module generating desired spacecraft state and reference motion. The hardware modelling cluster comprises an ephemeris model module to compute reference vectors in the inertial frame, a sensor modelling module to produce sensor measurements, and an actuator modelling module to simulate actuators. Finally, the ADC cluster performs the estimation of the spacecraft state with the attitude estimation module and the control by means of the attitude control module which implements a quaternion feedback controller.

7.3.1 Mission configuration

The Mission Database Module is an easy-to-edit block where the user can tailor all the parameters specific to the mission. The editable file is partitioned in four main sections: orbit, in which the user can set initial position and velocity of the platform, and the initial orbital parameters; platform, where the mass and inertial properties of the used platform, as well as spatial location of the ADCS box module, can be defined; mission, which is the section for characterizing the specific mission including the expected initial time epoch and the lifetime as well as the modes of ADCS.

The ADCS modes module is the controller ensuring the proper activation of the correct modules and sub-modules for the given mission configuration. Since the focus of this work is on modular attitude estimation for Earth-pointing spacecraft, only three nominal ADCS modes, as shown in Figure 54 have been considered: inertially pointing, nadir pointing and target pointing. If the selected mode is the inertially pointing, the ADCS modes module activates the attitude for regulation block, inside the Desired Orientation and Velocity module, and consequently the regulation feedback controller inside the Attitude Control module. The latter block performs a regulation control for driving an inertially pointing spacecraft to some fixed location while the angular velocity must go to zero. If the selected mode is nadir pointing and/or target pointing, the ADCS modes activates the attitude for tracking block and the corresponding tracking controller (see Figure 55). The attitude tracking can be used to control nadir and target pointing spacecraft to a desired time-varying attitude.

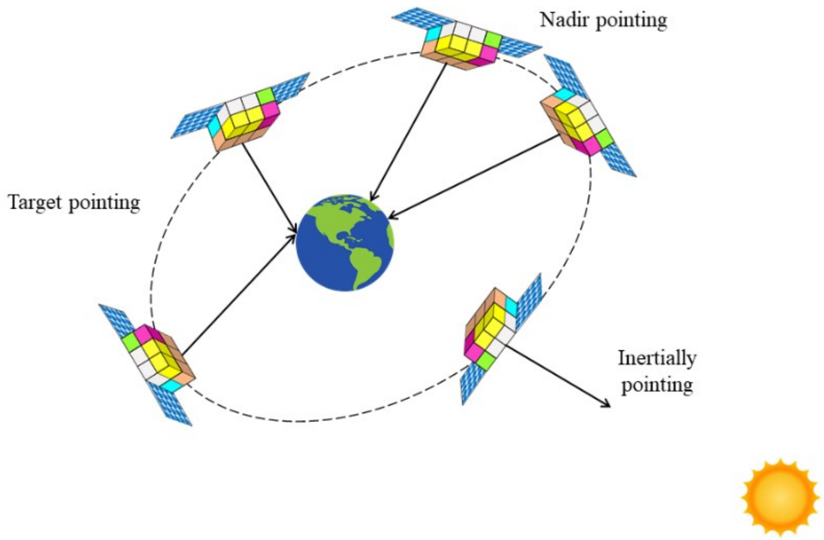

Figure 54 ADCS modes: inertial pointing, nadir pointing, target pointing

7.3.2 Spacecraft modelling

The Orbit propagator module oversees propagating the orbit on the base of input conditions defined by user based on a simple orbit propagator. The outputs of this block are orbit position and velocity vectors in the ECI frame, then converted from ECI into Latitude, Longitude, and Altitude (LLA) for reference vector computation by the ephemeris module.

The propagation is based on the computation of the Inverse Kepler Equation to find the value of the true anomaly given the mean anomaly and the eccentricity of the orbit.

$$\nu = \mathrm{M} + \left(2e - \frac{1}{4}e^3\right)\sin\mathrm{M} + \frac{5}{4}e^2\sin 2\mathrm{M} + \frac{13}{12}e^3\sin 3\mathrm{M} + \mathrm{O}\left(e^4\right) \tag{7.1}$$

Once computed, the radial distance can be determined

$$r = \frac{a\left(1-e^2\right)}{1+\cos\nu} \tag{7.2}$$

The true anomaly and the radial distance are used to compute the x-y positions in the orbit plane

$$\begin{aligned} x_{orb} &= r\cdot\cos\nu \\ y_{orb} &= r\cdot\sin\nu \end{aligned} \tag{7.3}$$

which can be then used to compute the x-y-z positions in the ECI frame by using the argument of periapsis, w, the longitude of the ascending node, Ω, and the orbit inclination, i, defined by the user in the mission database block, as follow

$$\begin{aligned} x_{ECI} &= x_{orb}\cdot\left(\cos w\cos\Omega - \sin w\cos i\sin\Omega\right) - y_{orb}\cdot\left(\sin w\cos\Omega - \cos w\cos i\sin\Omega\right) \\ y_{ECI} &= x_{orb}\cdot\left(\cos w\sin\Omega - \sin w\cos i\cos\Omega\right) + y_{orb}\cdot\left(\cos w\cos i\cos\Omega - \sin w\sin i\right) \\ z_{ECI} &= x_{orb}\cdot\left(\sin w\sin i\right) + y_{orb}\cdot\left(\cos w\sin i\right) \end{aligned} \tag{7.4}$$

The derivation of the position vector produces the velocity vector and, finally, the transformation from ECI to LLA is performed.

The Attitude Dynamics module gives as output the commanded quaternion, $\mathbf{q}_c$, for each simulation step. The block takes in input the commanded angular velocity, $\boldsymbol{\omega}_c$, which comes from the quaternion feedback controller, and computes the commanded quaternion by integrating the quaternion kinematic equation as

$$\begin{bmatrix} \dot{q}_1 \\ \dot{q}_2 \\ \dot{q}_3 \\ \dot{q}_4 \end{bmatrix} = \frac{1}{2} \begin{bmatrix} q_4 & -q_3 & q_2 & q_1 \\ q_3 & q_4 & -q_1 & q_2 \\ -q_2 & q_1 & q_4 & q_3 \\ -q_1 & -q_2 & -q_3 & q_4 \end{bmatrix} \begin{bmatrix} \omega_1 \\ \omega_2 \\ \omega_3 \\ 0 \end{bmatrix} = \frac{1}{2} Q \begin{bmatrix} \omega_1 \\ \omega_2 \\ \omega_3 \\ 0 \end{bmatrix} \tag{7.5}$$

The desired orientation and velocity module produces the desired quaternion, $\mathbf{q}_{\text{des}}$, and the desired angular velocity, $\boldsymbol{\omega}_{\text{des}}$. This module is subdivided into three elementary sub-modules: attitude for regulation, attitude for tracking, and attitude error, as shown in Figure 55. The first two blocks are activated/deactivated by the ADCS modes module according to the required ADCS task. The attitude for regulation block outputs the desired fixed quaternion while the desired angular velocity is zero.

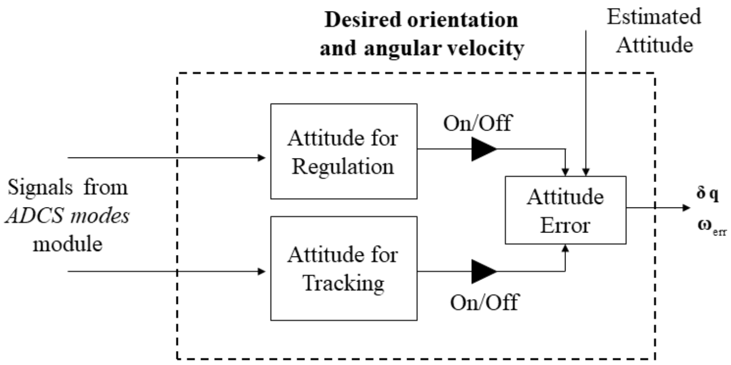

Figure 55 Desired orientation and angular velocity

The attitude for tracking block, instead, takes the desired direction cosine matrix, DCM_{des}, the satellite ECI position vector, $\vec{r}_{ECI}$, and the orbit angular momentum, $\mathbf{h}$, to compute the desired quaternion, $\mathbf{q}_{\text{des}}$, as

$$\begin{aligned} q_4 &= \frac{1}{2}\sqrt{\left(1+\text{tr}\left(\text{DCM}_{\text{des}}\right)\right)} \\ \mathbf{q}_v &= \frac{1}{4q_4} \begin{bmatrix} \text{DCM}_{23}\text{-DCM}_{32} \\ \text{DCM}_{31}\text{-DCM}_{13} \\ \text{DCM}_{12}\text{-DCM}_{21} \end{bmatrix}, q_4 \neq 0 \end{aligned} \tag{7.6}$$

and the desired angular velocity in the orbit frame, $\boldsymbol{\omega}_{\text{des,orb}}$, which is then converted in the body frame using the DCM derived from the actual body quaternion. The outputs of the former blocks go directly to the attitude error block which computes the error quaternion $\boldsymbol{\delta q}$ and the error angular velocity

$$\begin{aligned}&\boldsymbol{\delta q} \equiv \begin{bmatrix} \boldsymbol{\delta q}_{1:3} \\ \delta q_4 \end{bmatrix} = \mathbf{q}_{\mathrm{des}} \otimes \mathbf{q}_{\mathrm{est}}^{\mathbf{-1}} \\ &\boldsymbol{\omega}_{\mathrm{err}} = \boldsymbol{\omega}_{\mathrm{body}} - \boldsymbol{\omega}_{\mathrm{des}}\end{aligned} \tag{7.7}$$

which are inputted to the Attitude Control module for controlling the attitude to the desired one.

7.3.3 Hardware modelling

The hardware modelling cluster comprises the modules: reference vectors, sensor, and actuator. The reference vectors module produces reference vectors in the inertial frame at spacecraft LLA positions. These vectors are needed to extract attitude information from the corresponding sensed vectors in the body frame. There are three sub-modules inside this block, each one is used for a particular type of sensor (Sun sensor, Magnetometer, Earth sensor) that could be used in a particular mission (see Figure 56).

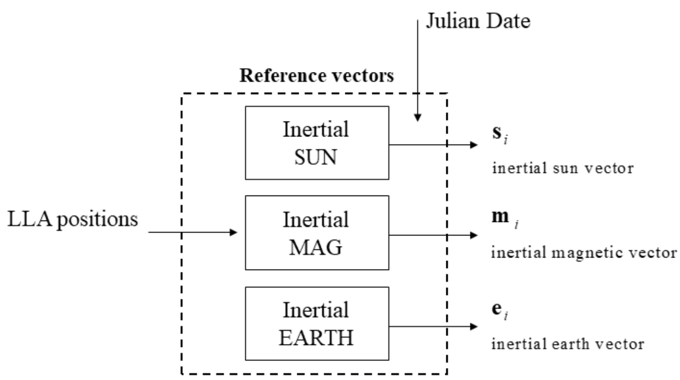

Figure 56 Reference vectors module

The first estimates the inertial Sun vector by taking the Julian Date of the current simulation time to calculate the number of days with respect to the J2000 epoch:

$$n = JD - 2451545.0 \tag{7.8}$$

Then the mean longitude, L, and mean anomaly, g, of the Sun are calculated as

$$L = 280.46 + 0.985674 \cdot n$$
$$g = 357.528 + 0.9856003 \cdot n \tag{7.9}$$

With these values, the ecliptic longitude, e, and obliquity, λ, can be derived

$$e = 23.439 + 0.0000004 \cdot \mathrm{n};$$
$$\lambda = \mathrm{L} + 1.915 \cdot \sin g + 0.020 \cdot \sin 2g \tag{7.10}$$

for estimating the ECI vector position, $\mathbf{S}_i$, of the Sun

$$x_i = R\cos\lambda$$
$$y_i = R\cos e \sin\lambda \tag{7.11}$$
$$z_i = R\sin e$$

Where R is the distance from Sun to Earth

$$R = 1.00014 - 0.01671 \cdot \cos g - 0.00014 \cos 2g \tag{7.12}$$

The second sub-module outputs the Earth's magnetic field at the desired LLA locations and time using the International Geomagnetic Reference Field 13 (IGRF-13) block available in MATLAB/Simulink. The last sub-module, instead, uses the Matlab WGS 84 Gravity model block to estimate the Earth's gravity. It is worth nothing that we assume the reference vectors as noise-free vectors for the entire time of simulation.

The sensor module, instead, simulates vector and quaternion measurements by adding noise to the true values taken from the attitude dynamic and the reference vector modules. The noise is added as normally Gaussian distributed signal with zero mean and variance equals to the standard deviation of the sensor. Specifically, the measured sun vector in body frame is simulated as

$$\mathbf{S}_b = R_i^b(\mathbf{q})\mathbf{S}_i + w \tag{7.13}$$

where $R_i^b(\mathbf{q})$ is the rotation matrix from the inertial frame to the body frame, $\mathbf{S}_i$ the inertial sun vector, and w is the additive noise. Similarly, the measured magnetic field in the body frame is simulated as

$$\mathbf{B}_b = R_i^b(\mathbf{q})\mathbf{B}_i + w \tag{7.14}$$

with a clear meaning of the symbols. The measured quaternion from star sensor is produced, instead, by adding to the actual quaternion a Gaussian random noise with variance depending on the used star tracker. The model for the simulation of the gyroscope is based on [144]. This model adds noise to the actual angular velocity obtained from the integration of the attitude dynamic equations to compute the measured angular velocity and the bias as follow

$$\begin{aligned} \bar{\boldsymbol{\omega}} &= \boldsymbol{\omega} + \xi_{sf} + \xi_{ma} + \eta_v \\ \dot{\beta} &= \eta_u \end{aligned} \tag{7.15}$$

where $\boldsymbol{\omega}$ is the actual angular velocity, ξ_{sf} and ξ_{ma} are gyro scale factor and misalignment errors, respectively, η_v is the Angular Random Walk (ARW) and η_u is the Rate Random Walk (RRW). Sensor parameters are defined in the mission database module by the user and then inputted to the modules. Since we assume a non-physical controller, the actuator module has not been considered in this work.

7.3.4 ADC cluster

The attitude estimation module and the attitude control module are part of the Attitude Determination Control (ADC) cluster.

The first module performs attitude estimation by using a generic multiplicative Extended Kalman Filter (MEKF) [145]. As well known, the MEKF uses as true quaternion the product of error quaternion, $\boldsymbol{\delta}\mathbf{q}$, and the estimate, $\hat{\mathbf{q}}$

$$\mathbf{q}^{true} = \boldsymbol{\delta}\mathbf{q}(\delta\theta) \otimes \hat{\mathbf{q}} \tag{7.16}$$

where $\delta\boldsymbol{\theta}$ is the three-component attitude error in the error state vector defined as

$$\Delta\mathbf{x} \equiv [\delta\theta \quad \delta\beta] \tag{7.17}$$

in which $\delta\beta$ is the error on the bias vector, $\boldsymbol{\beta}^{true} = \hat{\boldsymbol{\beta}} + \delta\boldsymbol{\beta}$, to be estimated. The estimation process involves the iteration of four steps: initialization, propagation, measurement update, and attitude update. The initialization step defines the initial state vector and the error covariance matrix. The propagation step propagates the state vector and the error covariance matrix to the next time step. The measurement update step uses measurements from the sensors to update the error state vector. The attitude update step updates the attitude quaternion and bias vectors. An analysis of each of these steps is given to point out what parts of the filter are not already abstracted from the actual application.

Initialization

The initialization procedure is a crucial step for ensuring reliable filter estimation. Bad initialization parameters always mean poor filter performance. Hence, filter tuning operations are performed, targeted to adjust initial filter parameters to achieve the best estimation performance. In a standard design, manual optimization is typically performed during the test phase of filter design. In this case, filter parameters are tuned and readjusted until the required performance is achieved. In a modular application, ad hoc modifications to the design of filter, as well as filter optimization based on trial-and-error test phase are not allowed. Consequently, tuning must be performed one-time to enhance the robustness of the filter for the largest number of the cases. Assuming that all the sensors are calibrated, and the variance of measurements is known, a rough initialization of the error covariance matrix can be obtained by using the Farrenkopf's equation [145]

$$P_0 = \Delta t^{1/4} \sigma_n^{1/2} \left(\sigma_v^2 + 2\sigma_u \sigma_v \Delta t^{1/2} \right)^{1/4} \tag{7.18}$$

where σ_n is the square root of the sum of variance of the used sensors, σ_u^2 and σ_v^2 are the variance associated to the ARW and RRW of the gyroscope, respectively, and Δt is the filter time. From Eq. (7.18) one can see that the Farrenkopf model for error covariance is highly parametrized, depending only on sensor parameters.

Propagation

The MEKF propagates both the attitude quaternion and the covariance of the error state vector. The discrete model for the propagation of the quaternion kinematics can be written as

$$\hat{\mathbf{q}}_{k+1}^{-} = \bar{\Omega}\left(\hat{\omega}_k^{+}\right) \hat{\mathbf{q}}_k^{+} \tag{7.19}$$

with

$$\bar{\Omega}\left(\hat{\omega}_k^+\right) = \begin{bmatrix} I_{3x3}\cos\left(0.5\left\|\hat{\omega}_k^+\right\|\Delta t\right) - \left[\hat{\Psi}_k^+ \times\right] & \hat{\Psi}_k^+ \\ -\hat{\Psi}_k^+ & \cos\left(0.5\left\|\hat{\omega}_k^+\right\|\Delta t\right) \end{bmatrix} \tag{7.20}$$

and

$$\hat{\Psi}_k^+ \equiv \frac{\sin\left(0.5\left\|\hat{\omega}_k^+\right\|\Delta t\right)\hat{\omega}_k^+}{\left\|\hat{\omega}_k^+\right\|} \tag{7.21}$$

where the post-update estimate of angular velocity is given by $\hat{\omega}_k^+ = \tilde{\omega} - \hat{\beta}_k^+$, i.e., by subtracting the angular velocity, $\tilde{\omega}$, provided by inertial sensors, and the post-update bias model, computed as $\hat{\beta}_k^+ = \hat{\beta}_k^-$. The discrete model for the covariance propagation, instead, can be written as

$$P_{k+1}^- = \Phi_k P_k^+ \Phi_k^T + G_k Q_k G_k^T \tag{7.22}$$

in which the expressions for Φ_k and G_k can be found in [145]. The estimated process noise covariance matrix, Q_k, is

$$Q_k = \begin{bmatrix} \left(\sigma_v^2\Delta t + \frac{1}{3}\sigma_u^2\Delta t^3\right)I_{3x3} & -\left(\frac{1}{2}\sigma_u^2\Delta t^2\right)I_{3x3} \\ -\left(\frac{1}{2}\sigma_u^2\Delta t^2\right)I_{3x3} & \left(\sigma_u^2\Delta t\right)I_{3x3} \end{bmatrix} \tag{7.23}$$

From Eq.(7.19) to (7.23), it is clear that the propagation step has already a high level of parametrization which allows to accommodate different configurations.

Measurement update

The propagated error state vector is updated by using sensor measurements to correct the prediction values. To incorporate sensors in the Kalman Filter, the innovation process model and the measurement sensitivity matrix must be written for each type of sensors used in the actual sensor suite. Both the measurement matrix and the innovation process models are, in general, different for vector sensors and quaternion sensors. Quaternion sensors provide sensor data directly as quaternions while vector sensors as vectors in the body frame. In traditional applications, star sensors can be both quaternion and vector sensors. However, to use star tracker as vector sensors, e.g., using body vector observations with respect to the stars. the computer containing the catalogued stars must be accessible. This is not more possible for modular applications, where all the sensors must be treated as “black-boxes”. Hence, star sensors are assumed to be only as quaternion sensors in this work. In this case, the measurement innovation process can be written as

$$\nu_{star} = \mathbf{q}_{meas} - \hat{\mathbf{q}} \tag{7.24}$$

while the measurement matrix will be

$$\mathbf{H} = \begin{bmatrix} I_{3x3} & 0_{3x3} \end{bmatrix} \tag{7.25}$$

The standard innovation for magnetometer sensor would be

$$\nu_{mag} = \mathbf{B}^{meas} - \overline{\mathbf{B}}^{b} \tag{7.26}$$

where $\overline{\mathbf{B}}^{b}$ is the predicted magnetic field computed by (7.14). The measurement matrix can be written as [145]

$$\mathbf{H} = \begin{bmatrix} \frac{\partial R_i^b(\hat{\mathbf{q}})}{\partial q_1}\mathbf{B}^i & \frac{\partial R_i^b(\hat{\mathbf{q}})}{\partial q_2}\mathbf{B}^i & \frac{\partial R_i^b(\hat{\mathbf{q}})}{\partial q_3}\mathbf{B}^i & 0_{3x3} \end{bmatrix} \tag{7.27}$$

which is obtained by linearizing the magnetic field around $\hat{\mathbf{q}}$. Since they are both vector sensors, the sun sensor can be treated very similarly to the magnetometer. The innovation process is

$$\nu_{sun} = \mathbf{S}^{meas} - \overline{\mathbf{S}}^{b} \tag{7.28}$$

and the measurement matrix

$$R = \text{diag}\left[\sigma^2{}_1 I_{3x3} \;\; \sigma^2{}_2 I_{3x3} \;\; \ldots \;\; \sigma^2{}_n I_{3x3}\right] \tag{7.29}$$

where σ_i is the noise variance of the i-th sensor measurement. The Kalman gain can be computed as

$$K = P_k^- H^T \left(H P_k^- H^T + R \right)^{-1} \tag{7.30}$$

and the update for covariance matrix

$$P_k^+ = \left(I_{3x3} - K_k H \right) P_k^- (I_{3x3} - K_k H)^T + K_k R K_k^T \tag{7.31}$$

Finally, the error state vector update follows

$$\Delta \mathbf{x}^{innovation} = K_k \Delta \mathbf{x} \tag{7.32}$$

Thus, the calculation of the sensitivity matrix, the Kalman gain, and the update of covariance matrix depends on which type of measurement has been used. As a consequence, the filter designer must know a-priori which sensors have been used in the specific mission to write the right expressions for each case. This, obviously, removes the possibility to reuse the same algorithm without further modifications. To enable the reusability of the filter in "as is" condition, instead of using vector measurements directly in the Kalman Filter, a quaternion estimator algorithm can be used to produce a quaternion measurement from the vector observations.

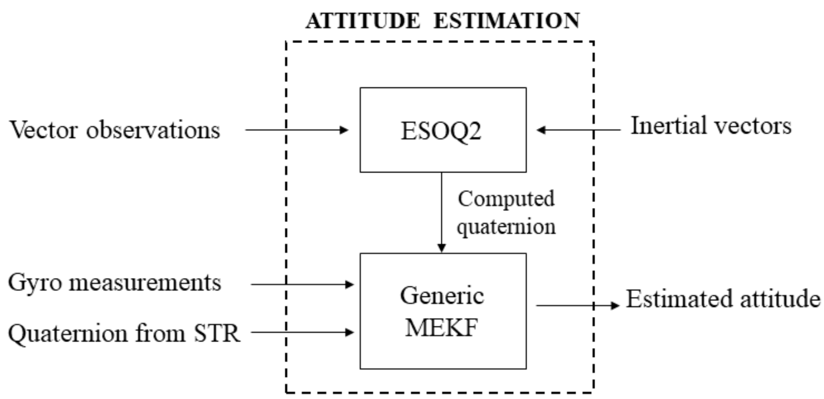

Figure 57 Attitude Estimation module

As depicted in Figure 57, vector sensors providing measurements as three-component fields (e.g., Earth's magnetic and gravity fields, sun vector) are fused with correspondent inertial vectors by using the ESOQ2 algorithm [145] to produce a computed quaternion. The computed quaternion is then inputted into the generic KF where it is fused again with quaternion measurements provided by star sensors, when available. Angular rate measurements from gyroscope are inputted to the KF for propagating filter equations. Hence, the filter has been designed to accept measurements only in the form of quaternion to be completely parametrized and sensor independent. In this way, the expressions for the innovation model, measurement matrix, Kalman gain and covariance updating, are always the same, no matter what type of measurement is used. It must be pointed out that the use of estimated quaternion instead of vector measurements as input to the Kalman Filter is a technique already used. Indeed, using computed quaternion in the Kalman Filter makes the measurement equation linear and relaxes the computational burden. Anyway, this technique has never be used for parametrizing filter equations with the intent to make them as more reusable as possible.

Another inherent problem for modular attitude estimation could be the sensor fusion of multi-rate sensors. The standard MEKF, indeed, must have all the measurements available to update the state vector. To overcome this problem, we use the Murrell's version of the Multiplicative Extended Filter Kalman (MMEKF) [145]. This filter, in fact, represents a natural solution for merging multiple sensor solutions produced at different rates. Indeed, by using the superposition principle, this filter uses one measurement at a time to update covariance matrix and state vector instead of all available measurements at once, as in the standard MEKF. The next advantage of this technique is the computational load reduced with respect to standard MEKF, which is valuable for an on-board implementation on limited small platforms. Instead of calculating a gain matrix that requires an inverse of a 3n x 3n matrix, only a 3 x 3 matrix inverse is required n times with Murrell's version. Figure 58 summarizes the MMEKF algorithm.

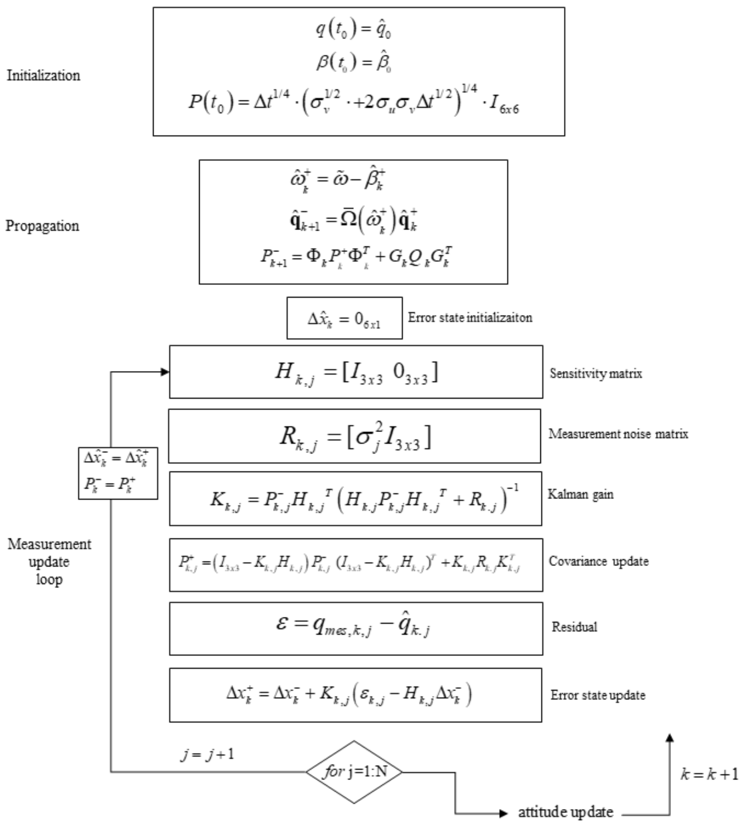

Figure 58 MMEKF algorithm

Attitude update

Finally, the attitude update equations for quaternion and bias estimations can be formulated as

$$\begin{aligned} \hat{q}_k^+ &= \hat{q}_k^- + 0.5\Xi(\hat{q}_k^-)\delta\theta \\ \hat{\beta}_k &= \hat{\beta}_k^- + \delta\beta \end{aligned} \tag{7.33}$$

where $\delta\theta$ and $\delta\beta$ are the updated values of the estimated error state vector and

$$\Xi(\mathbf{q}) = \begin{bmatrix} q_4 I_{3x3} + [\rho\times] \\ -\rho^T \end{bmatrix} \tag{7.34}$$

Attitude control module

A generic quaternion-feedback controller based on a simple PD control law is used to perform both the regulation of the attitude to a fixed inertially pointing attitude and for the tracking of time-varying attitude for earth-pointing modalities. It must be pointed out that the control module here is ideal and not referenced to specific hardware. This means that the physical actuation of control laws by actuators is ignored, and the control gains are set manually. Obviously, a simple and generic PD control law is not suitable for all type of actuator. However, this is enough for testing the modular attitude estimation in different pointing conditions. The quaternion-feedback controller is assumed in its simplest form as [145]

$$\mathbf{L} = -k_p \delta \mathbf{q}_{1:3} - k_d \boldsymbol{\omega} \tag{7.35}$$

where k_p and k_d are constant control gains and $\delta\mathbf{q}$ is the error quaternion.

7.4 Applications to different mission configurations

To test the reusability of the developed software in "as is" condition, three different test cases with low to high pointing accuracy requirements are taken in consideration. The test cases involve different pointing modalities to test the capability of software to adapt for different mission tasks. All these modes use a quaternion feedback controller to control the error quaternion and the angular rate. Inertial pointing will point the satellite towards an arbitrary fixed inertial attitude, which in this case is the Sun. In the nadir pointing mode, the satellite points its instruments towards the Earth's center, while in target pointing mode the boresight of payload is oriented towards a specific position on Earth. Different integrated ADCS boxes, with a specific hardware configuration required to meet specific requirements, are considered. In this way, the effects of hardware variations from case to case can be analyzed. Table 54 lists pointing modalities and the required accuracies for each test case.

Table 54 Ponting modalities and required accuracy for each test case

Test Case	Pointing Modality	Accuracy
# 1	Inertial pointing	5°
# 2	Nadir pointing	0.5 °
# 3	Target pointing	0.005 °

All missions are based on the same 12U CubeSat platform, with a mass of 10 kg but with different form factors. Indeed, the 12 x 1U cubes are arranged in different ways to have different inertia properties. Moreover, the ADCS module is placed in three different positions with respect to the center of the mass. This allows to test the capability of the software to cope with different physical configurations and spatial locations of the ADCS unit. Straightforwardness, the CG is located at (0,0,0) and the mass distribution is considered uniform. Table 55 reports specifications for the three reference platforms. Considering the CG of the ADCS units located at the center of the module, ADCS box 1 is placed with the respect to the spacecraft CG at (-5cm, 5cm, -10cm), while the ADCS box 2 is located at (+15cm, 0, -10cm) and, finally, the ADCS box 3 at (-5 cm, 0, -5cm).

Table 55 Platform form factors and overall characteristics

Form factor	**Mass**	**Dimensions**	**Inertia properties**
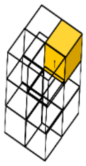 CASE 1: 6U x 2	10 kg	H = 30 cm D = 20 cm W = 20 cm	$I_{xx} = 0.65$ $I_{yy} = 0.65$ $I_{zz} = 0.40$
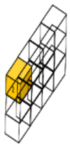 CASE 2: 3U x 4	10 kg	H = 30 cm D = 10 cm W = 40 cm	$I_{xx} = 0.65$ $I_{yy} = 0.85$ $I_{zz} = 1.25$
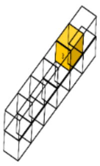 CASE 3: 2U x 6	10 kg	H = 60 cm D = 10 cm W =20 cm	$I_{xx} = 0.25$ $I_{yy} = 1.85$ $I_{zz} = 2.00$

For what concerns the hardware configuration of the ADCS boxes, the selection is based on mission requirements and available components on the CubeSat market. Moreover, the configurations involve different set of type of sensors to the test the capability of the algorithm to be abstracted from the used hardware. Specifically, the first ADCS box includes:

- Gyroscope
- 1 x Sun Sensor
- 1 x Magnetometer

As reference for the gyroscope, the ADIS16405 gyroscope [146] manufactured by ANALOG DEVICES with a sample rate of 330 Hz, an Angular Random Walk (ARW) of 2 deg/√h and Bias Instability of 0.007 deg/s is taken as reference; as Sun Sensor, the NSS CubeSat Sun Sensor [147] manufactured by NewSpace with an accuracy of 1 deg; as magnetometer, the ADIS16405 Magnetometer [146] manufactured by ANALOG DEVICES with a resolution of 125 nT corresponding to an accuracy of 0.2 deg, limited mass and power of 16g and 0.35W.

The second ADCS box, instead, includes:

- Gyroscope
- 1 x Sun Sensor
- 1 x Magnetometer
- 1 x Star Tracker

As reference for the gyroscope, the STIM277H Multi-Axis Gyro Module [148] manufactured by SENSONOR with a sample rate of 2000 Hz, an Angular Random Walk (ARW) of 0.15 deg/√h and Bias Instability of 0.003 deg/s; as Sun Sensor, the NSS Fine Sun Sensor [149] manufactured by NewSpace with an accuracy of 0.1 deg; as magnetometer, the NSS Magnetometer [150] manufactured by NewSpace with an accuracy of 80nT (0.08°) and an update rate of 18 Hz; as Star Tracker, the CubeStar [151] manufactured by CubeSpace, with a medium-accuracy of 0.06°, low-power and 55 g of mass, with an update rate of 1 Hz.

Finally, the third ADCS box is equipped with:

- Gyroscope
- 1 x Sun Sensor

- 1 x Magnetometer
- 2 x Star Tracker

as reference for the gyroscope, the STIM277H Multi-Axis Gyro Module [148] manufactured by SENSONOR with an update of 2000 samples/s, , an Angular Random Walk (ARW) of 0.15 deg/√h and Bias Instability of 0.003 deg/s; as references for the star sensors, the arcsec Sagitta Star Tracker [152] manufactured by Sagitta, with an accuracy of 10 arcseconds, 255 g of mass and a coverage of 99% of night sky, and the Nano Star Tracker ST-1 [153] manufactured by NanoAvionics with an observation accuracy of 8 arcseconds, 108 g of mass and data update rate of 5 Hz.

Table 56 resumes the hardware configuration of each case.

Table 56 Hardware configuration for each test case

Case	**Hardware configuration**			
	GYRO	SUN	MAG	STR
1	1 x ADIS16405	1 x NSSC	1 x ADIS16405	-
2	1 x STIM277H	1 x NSSF	1 x NSS Magnetometer	1 x CubeStar
3	1 x STIM277H	1 x NSSF	1 x NSS Magnetometer	1 x arcsec Sagitta 1 x Nano ST-1

7.4.1 Sun Pointing Mode

In the Sun Pointing mode, the solar arrays are pointing to the Sun while the attitude is inertially fixed. Specifically, the spacecraft is desired to point with the y-axis towards the Sun while the x-axis is along the direction of orbital velocity vector. The z-axis completes the right-handed coordinate frame. Figure 59 gives a pictorial representation of Sun pointing mode where $\hat{a}_1$ is the unit vector of the x-axis (roll), $\hat{a}_2$ is the unit vector of the y-axis (pitch) and $\hat{a}_3$ is the unit vector of the z-axis (yaw).

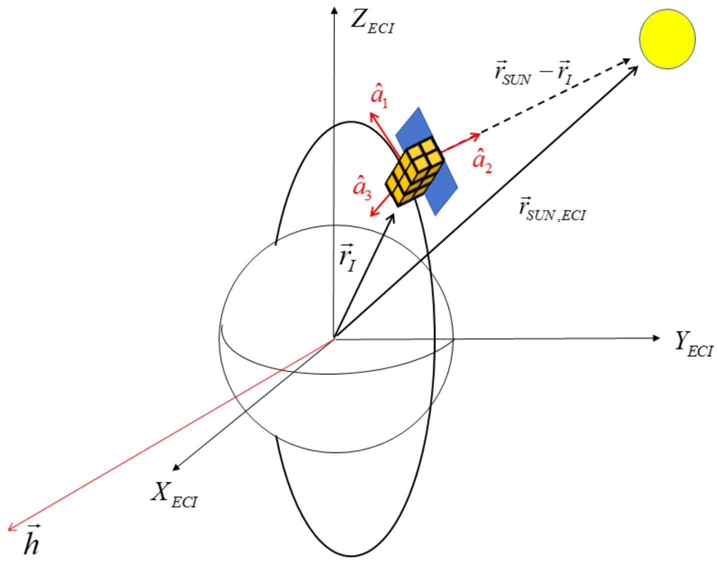

Figure 59 Sun Pointing mode

The representation of these vectors in the inertial frame will be

$$
\begin{aligned}
\hat{a}_1 &= \frac{\vec{v}}{\|\vec{v}\|} \\
\hat{a}_2 &= \frac{(\vec{r}_{sun} - \vec{r}_I)}{\|(\vec{r}_{sun} - \vec{r}_I)\|} \\
\hat{a}_3 &= \hat{a}_1 \times \hat{a}_2
\end{aligned}
\tag{7.36}
$$

while the desired spinning rate is given as

$$\vec{\omega}_{des} = [0\ 0\ 0] \tag{7.37}$$

7.4.2 Nadir Pointing Mode

In the Nadir Pointing mode, the desired attitude coincides with the orientation of Local Vertical-Local Horizontal (LVLH) frame. Hence, the $\hat{a}_3$ axis points towards the Earth's center in the nadir direction, the $\hat{a}_2$ is opposite to the angular momentum vector of the orbit, and the $\hat{a}_1$ axis completes the right-handed triad (see Figure 60).

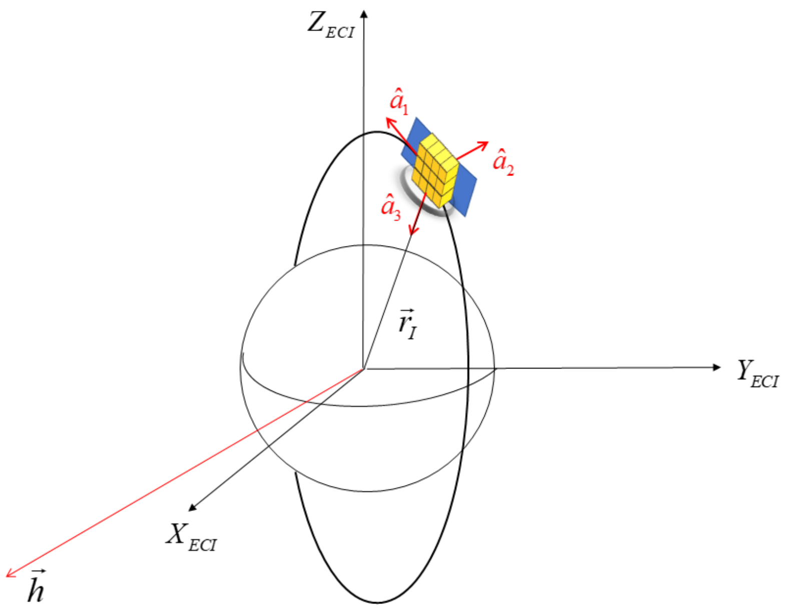

Figure 60 Nadir Pointing mode

The representation of the desired attitude in the Nadir Pointing Mode is

$$\hat{a}_1 = \hat{a}_2 \times \hat{a}_3$$
$$\hat{a}_2 = \frac{-\vec{h}}{\left\|\vec{h}\right\|} \tag{7.38}$$
$$\hat{a}_3 = \frac{-\vec{r}_I}{\left\|\vec{r}_I\right\|}$$

and the desired angular velocity

$$\vec{\omega}_{des} = [0 \ -\frac{\left\|\vec{h}\right\|}{\left\|\vec{r}_I\right\|^2} \ 0] \tag{7.39}$$

7.4.3 Target Pointing Mode

In this modality, the spacecraft axis where the instrument payload is located is pointed to a specific location on the Earth surface defined by a vector $\vec{p}_I$ (see Figure 61). The mathematical formulas for this mode are

$$
\begin{aligned}
\hat{a}_1 &= \hat{a}_2 \times \hat{a}_3 \\
\hat{a}_2 &= \frac{(\vec{p}_I - \vec{r}_I) \times \vec{v}}{\left\| (\vec{p}_I - \vec{r}_I) \times \vec{v} \right\|} \\
\hat{a}_3 &= \frac{\vec{p}_I - \vec{r}_I}{\left\| \vec{p}_I - \vec{r}_I \right\|}
\end{aligned}
\tag{7.40}
$$

and the desired angular velocity

$$
\vec{\omega}_{des} = [0 \ \text{-} \frac{(\vec{p}_I - \vec{r}_I) \times \vec{v}}{\left\| (\vec{p}_I - \vec{r}_I) \times \vec{v} \right\|^2} \ 0]
\tag{7.41}
$$

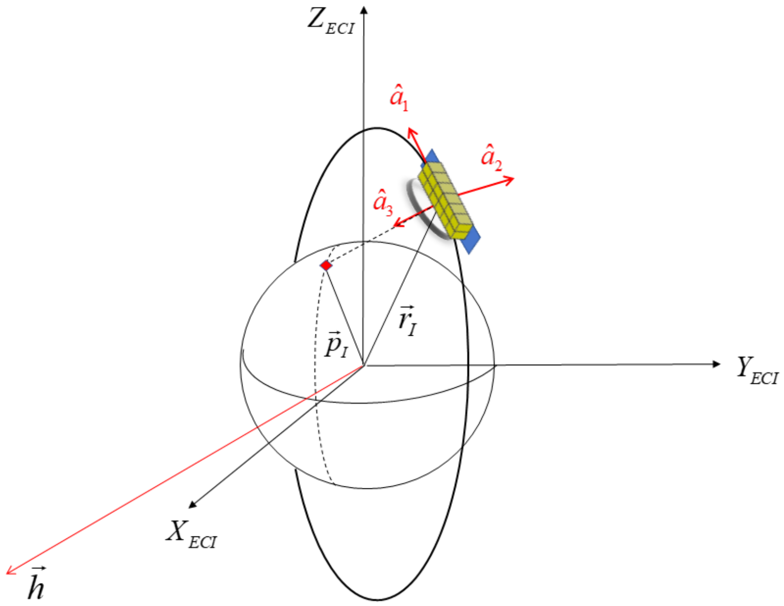

Figure 61 Target Pointing mode

7.5 Numerical examples

Numerical examples to test the estimation software over the above-described test cases are given in this section. For each case, the satellite is initialized according to the specific attitude required by the mission. Since no disturbance forces are considered, the control actions are performed only to command the spacecraft attitude to the desired one. The satellites are placed in a Sun Synchronous Orbit (SSO) with an altitude of 410 km, an eccentricity of 0.0011 and an inclination of 97 degrees. The remain satellite orbital parameters are listed in Table 57.

Table 57 Orbital parameters

Parameters	**Value**	**Unit**
Semimajor axis	678810	m
Eccentricity	0.0011	-
Longitude of ascending node	0	[°]
Orbit inclination	97	[°]
Argument of perigee	0	[°]
Mean anomaly	0	[°]
Orbital period	5560	s

During each simulation, the specific configuration of the simulated ADCS box is replicated activating only the corresponding set of sensors. To assess the fulfilment of the attitude errors requirements, the estimated values are compared to the actual values derived by integrating the attitude dynamic equations.

7.5.1 Test Case 1

In this numerical example, the spacecraft is maneuvered to point the solar panel face toward the Sun, while the actual angular velocity is driven to zero. The actual sensor configuration comprises two attitude sensors, namely sun sensor and magnetometer, and one inertial sensor, i.e., a gyroscope. The required attitude accuracy is 5° on each axis. The simulation time is equal to the orbital period of 5560 seconds. All the simulation parameters for the test case 1 are listed in Table 58.

Table 58 Simulation parameters of test case 1

Parameters		Values	Unit
Initial value	Initial attitude	[0; 0; 0]	[°]
	Initial attitude estimation	[0; 0; 0]	[°]
	Initial angular velocity	[0; 0.063; 0]	[°/s]
Sensors	Sun-Sensor accuracy	1	[°]
	Magnetometer resolution	125	[nT]
	Sample Frequency, Sun	15	[Hz]
	Sample Frequency, Mag	15	[Hz]
	Angular Random Walk	2	[°/√h]
	Gyro Bias Random Walk	0.007	[°/s]

Figure 62 compares the desired attitude, shown on the left, and the actual attitude commanded by the quaternion feedback controller. The error quaternion between the estimated attitude and the desired attitude is used to control the actual attitude to desired one. Since the physical actuation of control laws is neglected, the control errors are not shown.

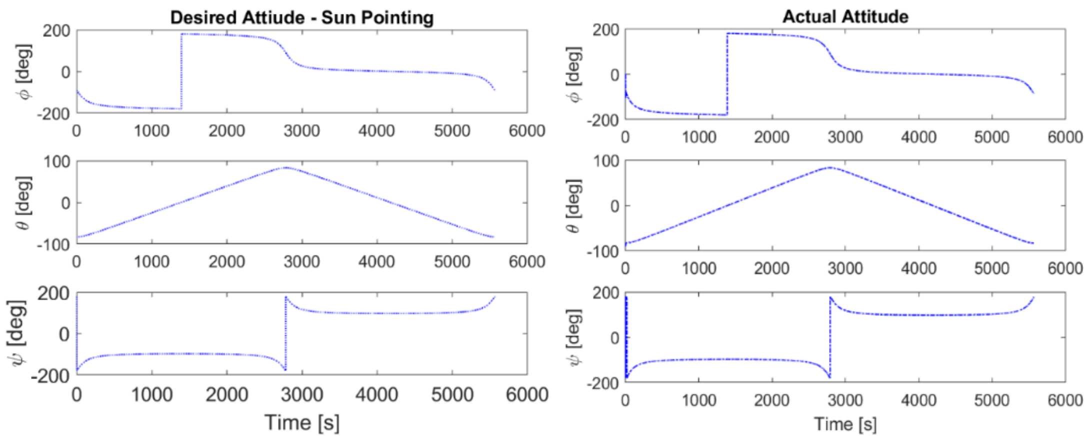

Figure 62 Comparison between the desired Sun Pointing attitude and actual attitude

The attitude is estimated by using vector measurements from sun sensor and magnetometer combined with the ESOQ2 algorithm to produce a quaternion measurement, then inputted to the Kalman filter. Using the ESOQ2 quaternion as quaternion measurement in the filter allows to use a generic and linear equation for the innovation model as

$$v_{case1} = \mathbf{q}_{esoq2} - \hat{\mathbf{q}} \tag{7.42}$$

where $\mathbf{q}_{esoq2}$ is the output quaternion of ESOQ2 algorithm. Estimation performances are shown in Figure 63 in terms of error Euler angles.

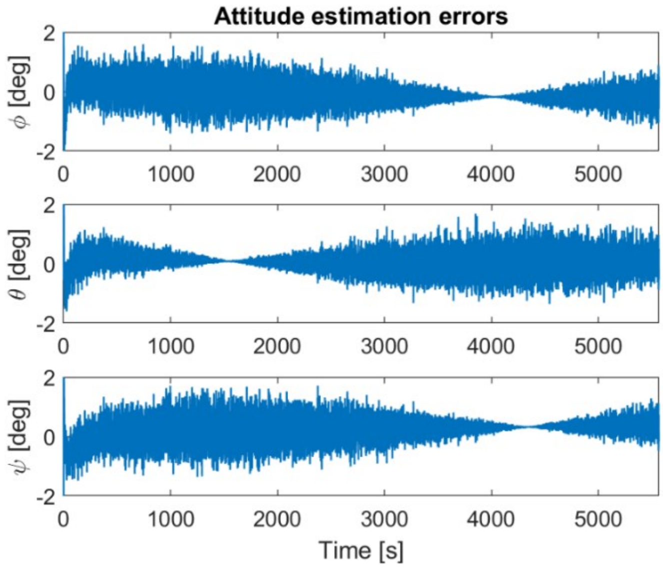

Figure 63 Attitude estimation errors of test case 1

From Figure 63, it can be seen that the fusion of ESOQ2 quaternion in the Kalman Filter exploiting only sun sensor and magnetometer measurements gives an estimation error of $\pm 2°$ which is within the required range of $\pm 5°$.

7.5.2 Test Case 2

In this numerical example, the spacecraft is oriented as the Local-Vertical Local-Horizontal (LVLH) frame, so the Z-axis is nadir pointing, the Y axis is normal to orbital plane and X completes the right-handed coordinate frame. With no acting disturbance torques, the spacecraft has a constant angular velocity equal in magnitude to the orbital mean motion. The required accuracy is 0.5° on each axis. The actual sensor configuration comprises two vector sensors, sun sensor and magnetometer, one star tracker and one gyroscope. All the simulation parameters for the test case 2 are listed in Table 59.

Table 59 Simulation parameters of test case 2

Parameters		Values	Unit
Initial value	Initial attitude	[0; 0; 0]	[°]
	Initial attitude estimation	[0; 0; 0]	[°]
	Initial angular velocity	[0; 0.063; 0]	[°/s]
Sensors	Sun-Sensor accuracy	0.1	[°]
	Magnetometer resolution	80	[nT]
	Star Tracker accuracy	0.06	[°]
	Sample Frequency, Sun	15	[Hz]
	Sample Frequency, Mag	15	[Hz]
	Sample Frequency, STR	1	[Hz]
	Angular Random Walk	0.15	[°/√h]
	Gyro Bias Random Walk	0.003	[°/s]

Figure 64 shows the desired attitude and the actual attitude, where one can see that the actual attitude is in good agreement with the desired one.

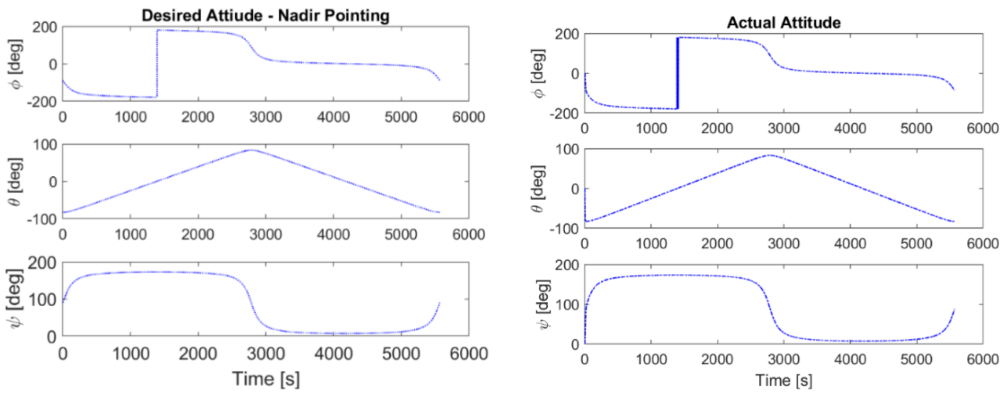

Figure 64 Comparison between the desired Nadir Pointing attitude and the actual attitude

In this case, as input to the filter we used the quaternion from ESOQ2, and the quaternion measured from star-tracker. Thus, the innovation model can be written as

$$v_{case2} = \begin{bmatrix} \mathbf{q}_{star} \\ \mathbf{q}_{esoq2} \end{bmatrix} - \begin{bmatrix} \hat{\mathbf{q}} \\ \hat{\mathbf{q}} \end{bmatrix} \tag{7.43}$$

The attitude estimation errors shown in Figure 65 confirms the fulfilment of the attitude requirements of $\pm 0.5°$.

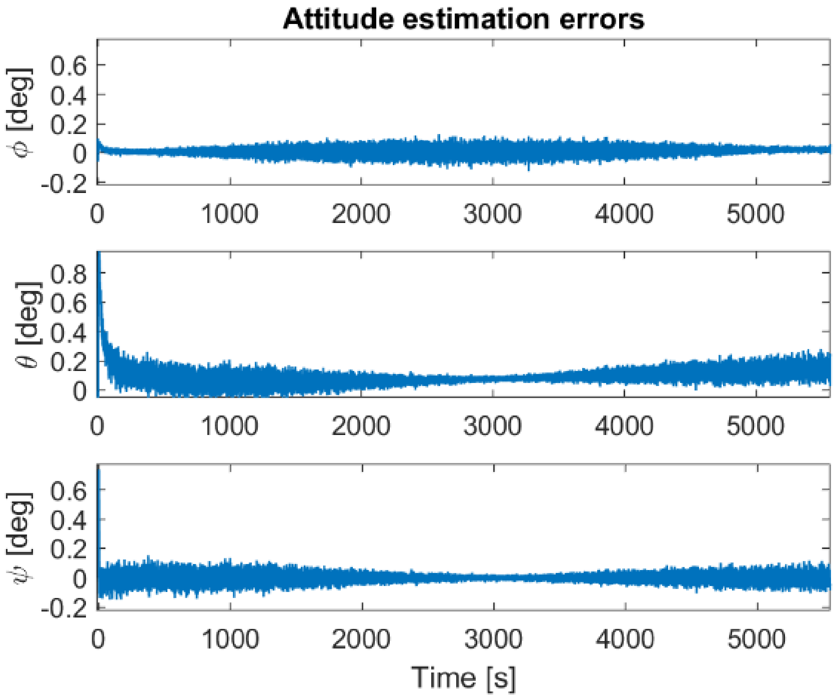

Figure 65 Attitude estimation errors of test case 2

7.5.3 Test Case 3

In test case 3, the spacecraft is controlled to point the payload boresight axis towards a specific target on the Earth, defined by a specific vector in ECEF frame. The required accuracy is 0.005° on the yaw-axis, which is the axis where the payload is located. The sensor configuration comprises a sun sensor, a magnetometer, two star-trackers and one gyroscope. All the simulation parameters for the test case 3 are listed in Table 60.

Table 60 Simulation parameters of test case 3

Parameters		Values	Unit
Initial value	Initial attitude	[0; 0; 0]	[°]
	Initial attitude estimation	[0; 0; 0]	[°]
	Initial angular velocity	[0; 0.063; 0]	[°/s]
Sensors	Sun-Sensor accuracy	0.1	[°]
	Magnetometer resolution	80	[nT]
	Star Tracker 1 accuracy	0.003	[°]
	Star Tracker 2 accuracy	0.002	[°]
	Sample Frequency, SUN	15	[Hz]
	Sample Frequency, MAG	15	[Hz]
	Sample Frequency, STR1	5	[Hz]
	Sample Frequency, STR2	5	[Hz]
	Angular Random Walk	0.15	[°/√h]
	Gyro Bias Random Walk	0.003	[°/s]

For target-pointing mode, a visibility flag between the spacecraft and target location is computed to provide an indication when attitude control should direct the spacecraft to point at the target. When the spacecraft exits the horizon, the payload face should continue pointing towards the earth surface to minimize orientation recovery when the target returns to view. A constant pointing location (when target is invisible) is the nadir, as it is independent of the spacecraft orbital position. Hence, the actual attitude must be commanded to the target attitude, when the visibility flag is met, and to the nadir attitude during the remain orbit period, as shown in Figure 66.

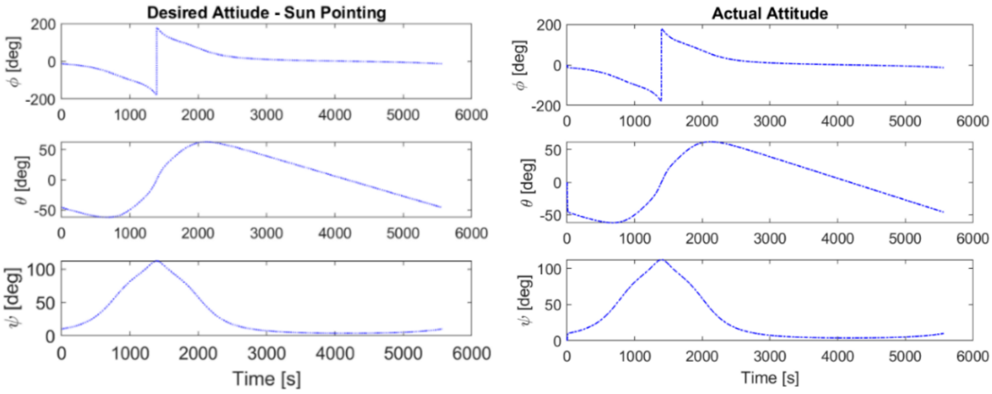

Figure 66 Comparison between the desired pointing attitude and the actual attitude

Utilizing the computed quaternion and the two measured quaternions from star sensors, the innovation model can be written as

$$\nu_{case3} = \begin{bmatrix} \mathbf{q}_{star1} \\ \mathbf{q}_{star2} \\ \mathbf{q}_{esoq2} \end{bmatrix} - \begin{bmatrix} \hat{\mathbf{q}} \\ \hat{\mathbf{q}} \\ \hat{\mathbf{q}} \end{bmatrix} \tag{7.44}$$

The tight attitude requirements of 0.005° are satisfied by fusing the measurements from the high-resolution star trackers, as shown in Figure 67.

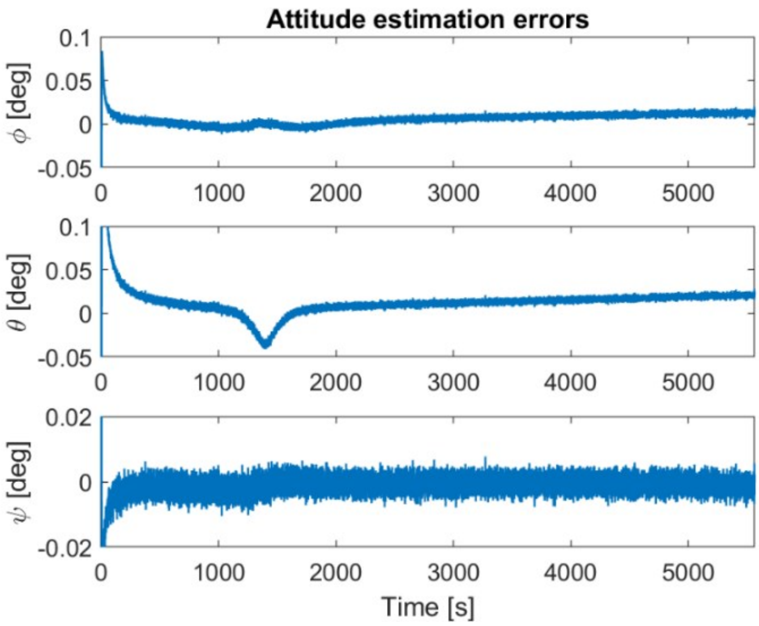

Figure 67 Attitude estimation errors of the test case 3

Conclusions

In this thesis, key aspects relevant to the design of Formation Flying Synthetic Aperture Radar (FF-SAR) mission have been characterized at both system, subsystem, and product level. From simulation results, the statement can be made that FF-SAR missions based on cluster of small satellites can achieve adequate performance to be considered for space demonstration and real-world applications. The conclusions about design solutions for modular attitude estimation were mainly conceptual. Indeed, a perfect modular platform has been assumed in this thesis ignoring technical issues arising with the plug-and-play modularity, as well as hardware and timing issues. Planned activities are intended to include these elements in the future analysis.

Specifically, for what concerns the design of FF-SAR mission, three scenarios have been individuated to demonstrate FF-SAR concept in different contexts.
The first scenario is based on a semi-active configuration comprising a fully active Transmitting-Receiving (Tx/Rx) satellite, i.e., a monostatic SAR platform, flying in formation with two Receiving (Rx) only satellites. Three working modes have been simulated for testing FF-SAR techniques, namely High-Resolution Wide-Swath (HRWS), Coherent Resolution Enhancement (CRE), and SAR tomography. Formation-flying design, instead, was performed to define feasible formation-flying configurations obtain passively safe and stable trajectories which fulfil distributed payload requirements for each assigned working mode. Simulation analysis confirmed the capability of the formation to enhance the performance of an equivalent monolithic SAR mission by exploiting FF-SAR techniques. Specifically, the monostatic platform has been designed to achieve 8m x 8m resolution on ground, with -24 dB Noise Equivalent Sigma Zero (NESZ), from an orbit altitude of 550 km, and 20° inclination. Working with three satellites with dominant along-track separations (up to 200m), HRWS imaging can be tested to cover a wider swath without range ambiguities and to suppress azimuth ambiguities by digital beamforming in azimuth. Simulation results confirm that the resolution improves from 8 m x 8 m of the single monostatic configuration to 8m x 4m. The second working mode has been used to demonstrate improvement in the ground-range resolution, by means of CRE technique. In detail, the satellites are displaced in

the formation with dominant cross-track/ vertical separations (up to 1km). In this way, the long cross-track separation can be used to widen the signal bandwidth to guarantee the desired ground range resolution. In particular, an effective baseline of about 1.5 km must be used to achieve less than 6 m ground range resolution. Finally, the working mode 3 assumes the monostatic SAR image of the Tx/Rx satellite and the two bistatic SAR images are coherently combined for SAR tomography. Specifically, SAR tomography processes multi-baseline acquisitions to calculate the complex reflectivity function for a scene including two-point targets located at -60 m and -20 m along the elevation direction.

The second scenario includes a satellite system for enabling single-pass multi-baseline interferometry. The design of constellation and formation design has resulted in a single-plane constellation of 8 evenly spaced formations, each composed by 4 platforms. This system ensures a daily revisit time, the same resolution of an equivalent monostatic SAR, i.e., 1m x 1m, but with a larger non-ambiguous swath width of 50 km, working at PRF halved with respect to the Nyquist frequency and 2.6 kW peak power, which is the half value of required power for the equivalent monostatic platform. The need for of 1 mm accuracy in the vertical displacement, is instead matched by the exploitation additional samples of the interferometric signal, acquired at different spatial positions, i.e. Multi-Baseline SAR interferometry through a multiplatform system.

The third scenario involves a cluster of passive receivers flying in in the same orbit of an illuminator of opportunity for matching the illuminator SAR performances with limited platforms by exploiting HRWS imaging and SNR improvement. Simulation analysis provided an estimate of three passive satellites as the minimum number of platforms that guarantees the achievement of an SNR like that of the monostatic SAR chosen as illuminator, the possibility of expanding the swath through HRWS and the ability to experimentally test different observation techniques.

In Section 4, a dedicated DSAR simulation environment has been described with a two-fold scope: i) understanding of the effect of error sources on the bistatic SAR focusing; ii) assessment of HRWS and CRE feasibility by DSAR when errors sources are taken into account. The simulator exploits NASA's General Mission Analysis Tool (GMAT) for generating high-fidelity trajectories for each DSAR satellite, and on an ad-hoc developed signal simulator able to deliver the raw data collected by each receiver. The simulation environment has been also completed by DSAR processing features, that is bistatic SAR focusing and beamforming, to combine raw data of each satellite into higher performance images. DSAR performance analysis has enabled the estimation of the main imaging parameters (geometric/radiometric resolution, ambiguity to noise ratio, integrated side-lobe ratio, peak to side-lobe ratio) with reference to realistic satellite paths. The most significant error sources have been identified and the models required to include the relevant effects in the simulation environment have been extensively discussed. DSAR error sources include radar synchronization errors, position and pointing errors, co-registration errors, antenna pattern errors and signal noise. Attention has been paid to the analysis of radar synchronization issues. The results of the error and sensitivity analysis performed that the resolution (IRW) achievable by FF-SAR is not affected by error sources, and the overall imaging performance is kept, even considering error sources. The investigation on the effect of error sources on beamforming algorithms and procedure, instead, suggests that not only the ambiguity suppression is feasible with errors but also that the SNR can be improved, exploiting DSAR features. Similarly, the application of the digital beamforming algorithm for CRE when errors are simulated confirm that the improvement of the range resolution is feasible, since the impact of errors source on IRW is negligible

Critical aspects related to satellite budgets of each analyzed scenario are outlined up to subsystem level, including electrical power subsystem, formation maintenance, telecommunication, and data handling. Mass budgets, for the Scenario 1, indicate that the total mass is about 100 kg for the Tx/Rx satellite and less than 80 kg for Rx-only. For the Scenario 2, instead, the total mass of Tx/Rx satellite is 170 kg and 114 kg for the passive platforms. Hence the results are in line with the use of microsatellites. A preliminary dimensioning of the passive platform to be used in the mission of Scenario 3 has been also performed. The sizing was based on a market survey related to hardware for CubeSat, available and/or in an advanced development phase. The class of nanosatellites capable of meeting the mission requirements has been individuated as 9-12 U CubeSat with a mass of about 10-13 kg and an average power of about 50 W.

In the Section 7.3, a generic version of the Murrell's Multiplicative Extended Kalman Filter (MMEKF) has been proposed for attitude estimation in a modular fashion. To test the reusability of the developed software in "as is" condition, three different test cases with low to high pointing accuracy requirements have been taken in consideration. The test cases involve different pointing modalities to test the capability of software to adapt for different mission tasks. Different integrated ADCS boxes, with a specific hardware configuration required to meet specific requirements, are considered. In this way, the effects of hardware variations from case to case have been analyzed. Hence, the same filter without any modifications have been uses to perform attitude estimation for different test cases with different pointing modalities, required accuracies and different spacecraft and hardware configuration. Simulation results shown that the attitude pointing requirements are satisfied for each test case.

Bibliography

[1] M. D'Errico, Distributed Space Missions for Earth System Monitoring. Publisher: Springer, Space Technology Library, vol. 31, New York, NY, USA, 2013; https://doi:10.1007/978-1-4614-4541-8.

[2] T. Wekerle, F. Pessoa, J. Bezerra, L. Vergueiro, L. Gonzaga. Status and Trends of Smallsats and Their Launch Vehicles. *Journal of Aerospace Technology and Management*, **2017**, 9, 269-286; DOI: 10.5028/jatm.v9i3.853.

[3] K. B. Clark, C. Y. Baldwin. Design Rules. Vol. 1: The Power of Modularity. *MIT Press*, **2000,** 1, https://doi.org/10.7551/mitpress/2366.001.0001.

[4] A. Renga, M. D. Graziano, A. Moccia. Formation Flying SAR: analysis of imaging performance by Array Theory. *IEEE Transactions on Aerospace and Electronic Systems*, **2020,** 57, 1480-1497; DOI: 10.1109/TAES.2020.3043526.

[5] M. Grasso, A. Renga, G. Fasano, M.D. Graziano, M. Grassi, A. Moccia. Design of an end-to-end demonstration mission of a Formation-Flying Synthetic Aperture Radar (FF-SAR) based on microsatellites. *Advances in Space Research*, **2020**, 67, 3909-3923; https://doi.org/10.1016/j.asr.2020.05.051.

[6] M. D. Graziano, A. Renga, M. Grasso, A. Moccia, PRF Selection in Formation-Flying SAR: Experimental Verification on Sentinel-1 Monostatic Repeat-Pass Data. *Remote Sens*, **2020**, 12 (29); https://doi.org/10.3390/rs12010029.

[7] A. Renga, M. D. Graziano, M. Grasso, A. Moccia. Evaluation of design parameters for formation flying SAR. *European Conference on Synthetic Aperture Radar, EUSAR Proceedings,* **2021,** 961-964.

[8] M. Grasso, A. Renga, G. Fasano, M.D. Graziano, M. Grassi, A. Moccia. Precursor of a formation-flying synthetic aperture radar (FF-SAR) based on a cluster of CubeSats. *71st International Astronautical Congress*, Virtual Online, 2020, 12-14 October.

[9] J. Bouwmeester et al. Survey of worldwide pico- and nano-satellites missions, distributions and subsystem technology. *Acta Astronautica*, **2010**, 67 (7-8), 854-862; https://doi.org/10.1016/j.actaastro.2010.06.004.

[10] J. Esper. Modular, adaptive, reconfigurable systems: technology for sustainable, reliable, effective, and affordable space exploration. *AIP Conference Proceedings*, **2005**, 746, 1033–1043; DOI: 10.1063/1.1867227.

[11] A. Renga, M. D. Graziano, M. Grasso, A. Moccia. Timing and Design Issues in Formation Flying Distributed SAR. *IEEE Radar Conference Proceedings*, Italy, Florence, September 2020; 10.1109/RadarConf2043947.2020.9266603.

[12] D. Selva, D. Krejci. A survey and assessment of the capabilities of Cubesats for Earth Observations. *Acta Astronautica*, **2012**, 74, 50-68; https://doi.org/10.1016/j.actaastro.2011.12.014.

[13] Q. Young. Modular Platform Architecture for Small Satellites: Evaluating Applicability and Strategic Issues. *19th Annual AIAA/USU Conference on Small Satellites*, USA, Logan, 2005.

[14] M. Kirschner, F.H. Massmann, M. Steinhoff. GRACE, in: Distributed Space Missions for Earth System Monitoring. 547–574. https://doi.org/10.1007/978-1-4614-4541-8_19.

[15] S. D'Amico, P. Bodin, M. Delpech, R. Noteborn. PRISMA, in: Distributed Space Missions for Earth System Monitoring. 599–637. https://doi.org/10.1007/978-1-4614-4541-8_21.

[16] G. Krieger, A. Moreira, H. Fiedler, I. Hajnsek, M.Werner, M. Younis, M. Zink. TanDEM-X: A satellite formation for high-resolution SAR interferometry. *IEEE Transactions on Geoscience and Remote Sensing*, **2007**, 3317–3340; https://doi.org/10.1109/TGRS.2007.900693.

[17] G. Krieger and A. Moreira. Multistatic SAR satellite formations: potentials and challenges. *IEEE International Geoscience and Remote Sensing Symposium Proceedings,* IGARSS, Korea (South), Seoul, 2005, 2680-2684; DOI: 10.1109/IGARSS.2005.1525618.

[18] D. Massonnet. Capabilities and limitations of the interferometric cartwheel. *IEEE Trans. Geosci. Remote Sens.*, **2001**, 39, (3), 506–520; DOI: 10.1109/36.911109.

[19] M. Martin, M. J. Stallard. Distributed Satellite Missions and Technologies - The TechSat 21 Program. *AIAA Space Technology Conference and Exposition*, AIAA 99-4479, September, 1999; https://doi.org/10.2514/6.1999-4479.

[20] A. Moccia, G. Rufino, M. D'Errico, G. Alberti, G. Salzillo. BiSSAT: a bistatic SAR for Earth observation. *IEEE International Geoscience and Remote Sensing Symposium (IGARSS) Proceedings*, **2002**, 5, 2628-2630; DOI: 10.1109/IGARSS.2002.1026723.

[21] N. Gebert, B. G. Domínguez, M. W. J. Davidson, M. D. Marin and P. Silvestrin, SAOCOM-CS - A passive companion to SAOCOM for single-pass L-band interferometry. *EUSAR Proceedings*, **2014**, 1-4.

[22] A. Giraldez. SAOCOM-1 Argentina L-band SAR mission overview. *Coastal and Marine Applications of SAR Symp. Proceeding,* **2003**.

[23] H. Rott, P. Lopez-Dekker, S. Solberg, L. Ulander, T. Nagler, G. Krieger, P. Prats, M. Rodriguez, M. Zonno, A. Moreira. SESAME: A single-pass interferometric SEntinel-1 companion SAR mission for monitoring GEO-and biosphere dynamics. *IEEE International Geoscience and Remote Sensing Symposium (IGARSS) Proceedings*, **2017,** 107–110; https://doi.org/10.1109/IGARSS.2017.8126905

[24] P. López-Dekker, H. Rott, P. Prats-Iraola, B. Chapron, K. Scipal, E. D. Witte, Harmony: an Earth Explorer 10 Mission Candidate to Observe Land, Ice, and Ocean Surface Dynamics, *IGARSS 2019 - IEEE International Geoscience and Remote Sensing Symposium*, 2019, pp. 8381-8384, doi: 10.1109/IGARSS.2019.8897983.

[25] G. Krieger, M. Zonno, M. Rodriguez-Cassola, P. Lopez-Dekker, J. Mittermayer, M. Younis, S. Huber, M. Villano, F.Q. De Almeida, P. Prats-Iraola, A. Moreira. MirrorSAR: A fractionated space radar for bistatic, multistatic and high-resolution wide-swath SAR imaging. *Int. Geosci. Remote Sens. Symp.*, **2017**, 149–152. https://doi.org/10.1109/IGARSS.2017.8126916.

[26] H. Helvajian and S. W. Janson. Small Satellites: Past Present and Future, El Segundo, CA, USA:AIAA, 2009.

[27] H. Heidt, J. Puig-Suari, A. Moore, S. Nakasuka, R. Twiggs. CubeSat: A new generation of picosatellite for education and industry low-cost space experimentation, *AIAA/USU Conference on Small Satellites*, **2000**, Logan, UT, USA, 11–26 September.

[28] J. Puig-Suari, R. Coelho, S. Williams. CubeSat design specification Rev. 12, The CubeSat program Cal. Poly SLO, 2009

[29] A. Poghosyan, A. Golkar. CubeSat evolution: Analyzing CubeSat capabilities for conducting science missions. *Progress in Aerospace Sciences*, **2017**, 88, 59–83; https://doi.org/10.1016/j.paerosci.2016.11.002

[30] A. Toorian, K. Diaz, S. Lee. The CubeSat Approach to Space Access. IEEE Aerospace Conference, Big Sky, MT, USA, 2008, 1–8 March; DOI: 10.1109/AERO.2008.4526293

[31] E. Peral et al., Radar Technologies for Earth Remote Sensing from CubeSat Platforms, *Proceedings of the IEEE,* **2018***,* 106 (3), 404 –418; DOI: 10.1109/JPROC.2018.2793179

[32] S. Bandyopadhyay, G. P. Subramanian, R. Foust, D. Morgan. A Review of Impending Small Satellite Formation Flying Missions. *53rd AIAA Aerospace Sciences Meeting Proceedings*, Kissimmee, FL, USA, **2015**, 5–9 January; DOI: 10.2514/6.2015-1623.

[33] S. Bandyopadhyay, R. Foust, G. P. Subramanian, S.J. Chung, F. Hadaegh. Review of Formation Flying and Constellation Missions Using Nanosatellites. *Journal of Spacecraft and Rockets,* **2016**, 53, 567-578; DOI: 10.2514/1.A33291.

[34] E. Peral et al. Raincube, a Ka-band precipitation radar in a 6U CubeSat. *31st AIAA/USU Conf. Small Satellite Proceedings,* Logan, UT, USA, **2017**, 5–10 August; DOI: 10.1109/IGARSS.2018.8519194

[35] N. Chahat, R. Hodges, J. Sauder, M. Thomson, E. Peral, Y. Rahmat-Samii. CubeSat Deployable Ka-Band Mesh Reflector Antenna Development for Earth Science Missions. *IEEE Transactions on Antennas and Propagation*, **2016**, 64(6), 2083-2093; DOI: 10.1109/TAP.2016.2546306.

[36] L. Wye and S. Lee. SRI CubeSat imaging radar for earth science (SRI-CIRES). *Earth Sci. Technol. Forum, Annapolis*, MD, USA, 2016, 14 June.

[37] P. A. Warren, J. W. Steinbeck, R. J. Minelli, C. Mueller. Large, deployable S-band antenna for a 6U CubeSat. *31th AIAA/USU Conf. Small Satellites Proceedings*, Logan, UT, USA, 5 – 10 August.

[38] T. L. Hoffman. GRAIL: Gravity Mapping the Moon. *IEEE Proceeding Aerospace Conference*, Big Sky, MT, USA, **2009**, 7-14 March; DOI: 10.1109/AERO.2009.4839327

[39] Tapley B. GRACE - Gravity Recovery and Climate Experiment, 2 March 2011, http://solarsystem.nasa.gov/scitech/display.cfm?ST_ID=186 (accessed 9.07.2020)

[40] N. Orr, J. Eyer, B. P. Larouche, R. E. Zee. Precision Formation Flight: The CanX-4 and CanX-5 Dual Nanosatellite Mission. *IAA Symposium on Small Satellite Systems and Services Proceedings* (4S), Rhodes, Greece, **2008**, 26 – 30 May.

[41] J. Eyer, C. Damaren, R. Zee, E. Cannon. A Formation Flying Control Algorithm for the CanX-45 Low Earth Orbit Nanosatellite Mission. *Space Technol.,* **2007**, 27(4), 147 – 158.

[42] M. Ali, S. Mauthe, F. Pranajaya. CNAPS: A Novel Propulsion System for the CanX-4 & CanX-5 Nanosatellite Mission. *27th International Symposium on Space Technology and Science (ISST) Proceedings,* 2009, Tsukuba, Japan, **2009**, 5 – 12 July.

[43] J. Bowen, M. Villa, A. Williams. CubeSat based Rendezvous, Proximity Operations, and Docking in the CPOD Mission. *29th Annual AIAA/USA Conference on Small Satellites*, Logan, UT, USA, **2015**, 8 – 13 August; DOI: 10.1109/AERO.2015.7119124

[44] VACCO propulsion system data sheet: https://www.vacco.com/images/uploads/pdfs/ReactionControlPropulsionModule-X13003000-01_0414.pdf

[45] G. Pini, H. Jacob, M. Meidad. The SAMSON Project – Cluster Flight and Geolocation with Three Autonomous nanosatellites. *AIAA/USU Conference on Small Satellites Proceedings*. **2012**.

[46] RACE double CubeSat mission, 05 June 2019, http://www.esa.int/ESA_Multimedia/Images/2019/06/RACE_double_CubeSat_mission (accessed 10.08.2020).

[47] ICEYE. ICEYE SAR Product Guide. 2019. Available online: https://www.iceye.com/hubfs/Downloadables/ICEYE-SAR-Product-Guide-2019.pdf (accessed on 01 October 2020).

[48] R. Bird, P. Whittaker, B. Stern, B, N. Angli, M. Cohen, R. Guida. NovaSAR-S: A low-cost approach to SAR applications. *Asia-Pacific Conference on Synthetic Aperture Radar (APSAR),* Tsukuba, Japan, **2013**, 23–27 September.

[49] H. Saito, P.R. Akbar, H. Watanabe, V. Ravindra, J. Hirokawa, K. Ura, P. Budhaditya. Compact X-band synthetic aperture radar for 100 kg class satellite. *IEICE Trans. Commun.,* **2017**, 1653–1660; https://doi.org/10.1587/transcom.2016PFI0008.

[50] R. O. Bartlett. Nasa standard multimission modular spacecraft for future space exploration. *16th American Astronautical Society and Deutsche Gesellschaft fuer Luftund Raumfahrt Proceedings,* Washington, DC, **1978,** March.

[51] IEEE. IEEE Standard 1451.2-1997 IEEE Standard for a Smart Transducer Interface for Sensors and Actuators-Transducer to Microprocessor Communication Protocols and Transducer Electronic Data Sheet (TEDS) Formats. IEEE, 1997.

[52] S. McDermott, D. Goldstein. The bitsytm spacecraft kernel: reducing mission cost with modular architecture and miniature technology. *IEEE Aerospace Conference Proceedings*, 2000, 4, 1-6.

[53] B. M. Cook, P. H. Walker. Spacewire and IEEE 1355 revisited. *International Spacewire Conference Proceedings*, **2007.**

[54] J. Lyke, D. Fronterhouse, S. R. Cannon, D. Lanza, T. Byers. Space plug-and-play avionics. *3rd Responsive Space Conference Proceedings,* Los Angeles, CA, **2005**, April.

[55] D. Fronterhouse, K. Center, B. Strunce, T. Mann, J. Dipalma. Pnpsat-2 SPA technology testbed initial results and development status. *AIAA Aerospace Conference*, **2010**, March, 1-12.

[56] P. McGuirk, G. Rakow, C. Kimmery, P. Jae, R. Klar, A. Bertrand. Spacewire plug-and-play (pnp). *AIAA Aerospace Conference*, Rohnert Park, CA, **2007**, May.

[57] N. Francis, P. Collier, J. Lyke. Optical networking for aerospace systems pro-visioned through plug-and-play avionics. *AIAA Aerospace Conference,* Atlanta, GA, **2010**, April.

[58] J. Lyke, J. Christensen, S. Cannon. A plug-and-play approach based on the i2c standard. *24th Annual AIAA/USU Conference on Small Satellites,* Logan, UT, **2010**, August.

[59] C. Kief, B. K. Zufelt, J. Christensen, J. K. Mee. Trailblazer: Proof of concept cubesat mission for SPA-1. *AIAA Aerospace Conference*, St.Louis, MO, **2011**, March.

[60] M. Martin, J. Summers, J. Lyke. AFRL plug-and-play spacecraft avionics experiment (sae). *Aerospace Conference Proceedings*, **2012**, March, 1-6.

[61] C. Kief, B. Zufelt, S. Cannon, J. Lyke, J. K. Mee. The advent of the pnp cube satellite. *Aerospace Conference*, **2012**, March, 1-5.

[62] J. Lyke, M. Ahlsberg, D. Fronterhouse, C. Kief, M. Hannon, P. Christian. Nanosatellite and Plug-and-Play Architecture II (NAPA II) Update. Technical Report, **2019**, August; https://apps.dtic.mil/sti/pdfs/AD1082033.pdf.

[63] C. Kief, M. Hannon, J. Lyke, C. Peters, D. Fronterhouse and M. Ahlberg. SPARC – 1: A New, Improved Modular 6U Spacecraft. *IEEE Aerospace Conference*, **2019**, 1-8, DOI: 10.1109/AERO.2019.8742248.

[64] M. Thomas. Design automation and performance analysis of modular reconfigurable attitude control systems. PhD dissertation, Technische Universität Berlin, **2019**; DOI: http://dx.doi.org/10.14279/depositonce-8949.

[65] V. H. Selby. Modular Attitude Determination and Control System for Small Satellites. *4th Annual AIAA/USU Conference on Small Satellites Proceedings*, **1990**, 1–13.

[66] T. Osterloh, J. Rossmann. A rigid body dynamics simulation framework for the analysis of attitude control systems of modular satellite systems. *IEEE International Systems Conference (SysCon),* **2019,** 8-11 April; DOI: 10.1109/SYSCON.2019.8836713.

[67] S. C. Grocott. Modular Attitude Control System for Microsatellites with Stringent Pointing Requirements. *14th AIAA/USU Small Satellites Conference Proceedings*, Logan, Utah, **2000**, 21-24 August.

[68] J. Hansen, P. Graven, D. Fogle, J. Lyke. The Feasibility of Applying Plug-and-Play Concepts to Spacecraft Guidance, Navigation, and Control Systems to Meet the Challenges of Future Responsive Mission. *7th International ESA Conference on Guidance, Navigation, & Control Systems*, Tralee, County Kerry, Ireland, **2009**, June 2-5.

[69] J. Hansen, J. Pollack, P. Graven, Y. Plam. Plug-and-Play for Creating Instant GNC Solutions. *21st annual AlAAJUSU Conference on Small Satellites Proceedings*, Logan Utah, **2007**, 13- 16 August.

[70] P. Graven, J. Hansen, A Guidance, Navigation and Control (GNC) Implementation of Plug-and-Play for Responsive Spacecraft. *Aerospace Conference and Exhibit*, Rohnert Park, CA, **2007**, 7 - 10 May.

[71] J. Hanson, J. Hansen. Development of attitude control systems for modular spacecraft. *Aerospace Conference Proceedings,* Big Sky, MT, **2014**.

[72] A. Moccia. Synthetic Aperture Radar. In: Blockley R, Shyy W (eds) Encyclopedia of aerospace engineering. Wiley, Chichester, **2012**.

[73] P. A. Rosen, S. Hensley, I.R. Joughin, F.K. Li, S.N. Madsen, E. Rodriguez, R.M. Goldstein, Synthetic aperture radar interferometry. *IEEE*, **2000**, 88(3), 333–382. DOI: 10.1109/5.838084.

[74] N. A. Goodman, J.M. Stiles. Resolution and synthetic aperture characterization of sparse radar arrays. *IEEE*, **2003**, 39, 921–935; DOI: https://doi.org/10.1109/TAES.2003.1238746.

[75] N. Gebert, G. Krieger, A. Moreira. Digital beamforming on receive: Techniques and optimization strategies for high-resolution wide-swath SAR imaging. *IEEE Trans. Aerosp. Electron. Syst.,* **2009***,* 45, 564–592; DOI: https://doi.org/10.1109/TAES.2009.5089542.

[76] G. Krieger, N. Gebert, A. Moreira. Unambiguous SAR signal reconstruction from nonuniform displaced phase center sampling. *IEEE Geoscience Remote Sens. Lett.,* **2004**, 1, 260–264; DOI: 10.1109/LGRS.2004.832700.

[77] N. Sakar, M. Rodriguez-Cassola, P. Prats-Iraola, A. Reigber, A. Moreira. Analysis of Geometrical Approximations in Signal Reconstruction Methods for Multistatic SAR Constellations with Large Along-Track Baseline. *IEEE Geosci. Remote Sens. Lett.*, **2018**, 15, 892–896; DOI: 10.1109/LGRS.2018.2811804.

[78] C. Prati, F. Rocca. Improving Slant-Range Resolution with Multiple SAR Surveys. *IEEE Transaction on Aerospace and Electronic Systems*, **1993**, 29, 1, 135-144; DOI: 10.1109/7.249119.

[79] S. V. Baumgartner, G. Krieger. Dual-Platform Large Along-Track Baseline GMTI. *IEEE Transactions on Geoscience and Remote Sensing,* **2016**, 54, 3, 1554-1574; DOI: 10.1109/TGRS.2015.2483019.

[80] P. Guccione, A. Monti Guarnieri, F. Rocca, F, D. Giudici, N. Gebert. Along-Track Multistatic Synthetic Aperture Radar Formations of Minisatellites. *Remote Sens*. **2020**, 12(1), 124; https://doi.org/10.3390/rs12010124

[81] R. Opromolla, G. Fasano, G. Rufino, M. Grassi. Design of relative trajectories for in orbit proximity operations. *Acta Astronautica*, **2018**, 145, 342–356; DOI: 10.1016/j.actaastro.2018.01.062.

[82] G. Fasano, A. Renga, M. D'Errico. Formation Geometries for Multistatic SAR Tomography. *Acta Astronautica*. **2014**, 96, 11-22; DOI: 10.1016/j.actaastro.2013.11.024.

[83] M. Nannini, R. Scheiber, A. Moreira. Estimation of the minimum number of tracks for SAR tomography. *IEEE Trans. Geosci. Remote Sens.,* **2009,** 47, 531-543; https://doi.org/10.1109/TGRS.2008.2007846.

[84] N.A. Goodman, J.M. Stiles. Resolution and synthetic aperture characterization of sparse radar arrays. *IEEE Trans. Aerosp. Electron. Syst.*, **2003**, 39, 921–935; https://doi.org/10.1109/TAES.2003.1238746.

[85] P. López-Dekker, G. Krieger, A. Moreira, Multistatic Radar Systems BT in *Distributed Space Missions for Earth System Monitoring*, M. D'Errico (Ed.), Springer New York, **2013**, New York, NY, pp. 61–122; https://doi.org/10.1007/978-1-4614-4541-8_2.

[86] G. Fornaro, F. Serafino, F. Soldovieri. Three-dimensional focusing with multipass SAR data. *IEEE Trans. Geosci. Remote Sens.* 41, 507–517; https://doi.org/10.1109/TGRS.2003.809934

[87] V. Stanzione, B. Sabatinelli. Platino Project: A new italian multi-application small satellite platform for highly competitive missions. *69th International Astronautical Congress*, Bremen, Germany, **2018**, 1–5 October.

[88] A. Moccia, A. Renga. Spatial Resolution of Bistatic Synthetic Aperture Radar: Impact of Acquisition Geometry on Imaging Performance, *IEEE Trans. on Geoscience and Remote Sensing*, **2011**, 49(10), 3487 – 3503; DOI: 10.1109/TGRS.2011.2115250.

[89] S. Chiu, C. Livingstone. A Comparison of Displaced Phase Centre Antenna and Along-Track Interferometry Techniques for RADARSAT-2 Ground Moving Target Indication. *Canadian Journal of Remote Sensing*, **2005**, 31(1), 37–51; DOI: 10.5589/m04-052.

[90] NASA's General Mission Analysis Tool (GMAT), [online] available at https://gmat.gsfc.nasa.gov/.

[91] I. G. Cumming, F. Wong. Digital Processing of Synthetic Aperture Radar. Norwood, MA, USA: Artech House, 2005.

[92] G. Krieger, M. Younis. Impact of oscillator noise in bistatic and multistatic SAR. *IEEE Geosci. Remote Sens.*, **2006**, 424–428; DOI: 10.1109/LGRS.2006.874164.

[93] M. Rodriguez-Cassola, S. V. Baumgartner, G. Krieger, A. Moreira. Bistatic TerraSAR-X/F-SAR Spaceborne–Airborne SAR Experiment: Description, Data Processing, and Results. *IEEE Transactions on Geoscience and Remote Sensing,* **2010**, 48(2), 781-794; DOI: 10.1109/TGRS.2009.2029984.

[94] R. Bamler, F. Meyer, W. Liebhart. Processing of bistatic SAR data from quasi-stationary configurations. *IEEE Trans. Geosci. Remote Sens.*, **2007**, 45(11), 3350–3358; DOI: 10.1109/TGRS.2007.895436.

[95] W. Q. Wang, C. B. Ding, X. D. Liang. Time And Phase Synchronization Via Direct-Path Signal For Bistatic Synthetic Aperture Radar Systems. *IET Radar Sonar Navig.*, **2008**, 2(1), 1-11; DOI: 10.1049/iet-rsn:20060097.

[96] J.C. Curlander, R. N. McDonough. Synthetic aperture radar systems & signal processing. Wiley, Wiley Series in Remote Sensing, New York, 1991.

[97] R. Conley, R. J. Cosentino, C. J. Hegarty, E. D. Kaplan, J. L. Leva, M. U. de Haag, M. U, K. Van Dyke. Performance of Stand-Alone GPS. In Understanding GPS – Principles and Applications, 2nd Ed.; E. D. Kaplan and C. J. Hegarty, Eds., Artech House, Boston/London, 2006.

[98] R. J. Cosentino, D. W. Diggle, M. U. de Haag, C. J. Hegarty, D. Milbert, J. Nagle. Differential GPS in Understanding GPS—Principles and Applications, E. D. Kaplan and C. J. Hegarty, Eds., Artech House, London, UK, 2nd edition, 2006.

[99] U. Tancredi, A. Renga, M. Grassi. Novel closed-loop approaches for precise relative navigation of widely separated GPS receivers in LEO. *Acta Astronautica*, **2014**, 93, 243-251; DOI: 10.1016/j.actaastro.2013.07.029.

[100]F. Menzione, A. Renga, M. Grassi. On-board orbit determination for low thrust LEO-MEO transfer by Consider Kalman Filtering and multi-constellation GNSS. *Acta Astronautica*, **2017**, 138, 242-254; DOI: 10.1016/j.actaastro.2017.05.029.

[101]J. R. Wertz. Spacecraft Attitude Determination and Control, Springer Netherlands, 1978. https://books.google.it/books?id=GtzzpUN8VEoC.

[102]M. Schwerdt, J.H. Final. TerraSAR-X Calibration Results Based on Novel Efficient Calibration Methods. *IEEE Trans. Geosci. Remote Sens.*, **2010**, 48, pp. 677-689; DOI: 10.1109/TGRS.2009.2035308.

[103] H. Saito, A. Tomiki, P. R. Akbar, T. Ohtani, K. Nishijo, J. Hirokawa, and M. Ando, "Synthetic aperture radar compatible with 100kg class piggy-back satellite," in *Conference Proceedings of 2013 Asia-Pacific Conference on Synthetic Aperture Radar, APSAR 2013*, 2013.

[104]C. D. Brown. Elements of Spacecraft Design. 2002.

[105]J. R. Wertz, W. J. Larson. Space mission analysis and design. *Choice Rev. Online*, 1992.

[106]R. Kahle, S. D'Amico. The TERRASAR-X Precise Orbit Control - Concept and Flight Results. *Int. Symp. Sp. Flight Dyn.*, 2014.

[107]D. A. Vallado. Fundamentals of Astrodynamic and Applications. Space Tech. Springer and Microcosm Press, 2007.

[108]SAFT Li-Ion Batteries datasheet; URL: http://www.houseofbatteries.com/documents/VES.pdf.

[109]NanoPower BP4, 10 October 2014; URL: https://gomspace.com/UserFiles/Subsystems/datasheet/gs-ds-nanopower-bp4-27.pdf.

[110]30% Triple Junction GaAs Solar Cell Type: TJ Solar Cell 3G30C, 05 June 2019; URL: http://www.azurspace.com/images/products/0004148-00-01_DB_GBK_80%C2%B5m.pdf.

[111]Berlin Space Technology, 2020. ST-200 datasheet; URL: https://www.berlin-space-tech.com/portfolio/1913/.

[112]Blue Canyon Tech, 2020. Reaction wheels datasheet; URL: https://bluecanyontech.com/components.

[113]Sitael, 2020. Sun and magnetic sun sensors datasheet; URL: https://www.sitael.com/space/small-satellites/subsystems/aocs-gnc/digital-sun-sensor-sitael.

[114]Hegel D. Attitude Determination Control, 2018; URL: https://storage.googleapis.com/blue-canyon-tech-news/1/2020/06/BCT_DataSheet_Components_ACS_06_2020.pdf.

[115]A. Dinardi et al. High-Performance Green Propulsion (HPGP): A flight-proven capability and cost game-changer for small and secondary satellites. *Proceedings of the AIAA/USU Conference on Small Satellites*, Advanced Technologies I, SSC12-III-6; https://digitalcommons.usu.edu/smallsat/2012/all2012/27/.

[116]IQ spacecom, 2020. S-link intersatellite link datasheet; URL: https://www.iq-spacecom.com/products/slink.

[117]SST X-band data transmitter and recorder: URL: http://www.sst-us.com/downloads/datasheets/x_band-antenna-pointing-mechanism-v1_05.pdf.

[118]Embarked Flight Computer; URL: http://www.sst-us.com/SSTL/files/d5/d552c05a-b8b4-4b1b-b18d-163e190ce7eb.pdf.

[119]NanoDockSDR datasheet, April 2019; URL: https://gomspace.com/UserFiles/Subsystems/datasheet/gs-ds-nanodock-sdr_-_1.PDF.

[120]A. Lovascio, A. D'Orazio, V. Centonze. Design of COTS-Based Radio-Frequency Receiver for Cubesat Applications. *IEEE Proceeding International Workshop on Metrology for AeroSpace* (MetroAeroSpace). 2019.

[121]NewSpace-GPS receiver datasheet, April 2020; URL: https://www.newspacesystems.com/wp-content/uploads/2020/04/NewSpace-GPS-Receiver_9a.pdf.

[122]P. M. Wegner, P. Blower, and J. Wilkenfeld. Standard buses, modular buses, and plug-and-play buses; what is the difference and why does it matter? Report No. A553345, 2008.

[123]C. Passerone, M. Tranchero, S. Speretta, L. Reyneri, C. Sansoe, D. Del Corso. Design solutions for a university nanosatellite. *IEEE Aerospace Conference*, Big Sky, MT, USA, 1-8 March 2008, 1-13; DOI: 10.1109/AERO.2008.4526530.

[124]T. Morphopoulos, L.Hansen, J. Pollack, J. Lyke, S. Cannon. Plug-and-Play – An Enabling Capability for Responsive Space Missions. *Responsive Space Conference*, Los Angeles, CA, 19-22 April 2004.

[125]J. Lyke. Plug-and-play as an Enabler for Future Systems. *Proceedings of the AIAA Space Conference*, Anaheim, California, 30 August – 2 September 2010; https://doi.org/10.2514/6.2010-8660.

[126]J. Lyke. Bringing the Vision of Plug-and-Play to High-Performance Computing on Orbit. *13th Annual Workshop on High Performance Embedded Computing*, Lexington, MA, September 2009.

[127]D. Fronterhouse, J. Lyke, S. Achramowicz. Plug-and-play satellite (PnPSat). *AIAA Aerospace Conference and Exhibit*, May 2007, p. 2914; DOI: 10.2514/6.2007-2914.

[128]J. Patel, D. E. Brinza, T. A. Tran, B. R. Blaes. Plug-and-play environmental monitoring spacecraft subsystem. Tech. Rep., Vol. 35, no. 3, pp. 30-32. NASA Jet Propulsion Laboratory, Pasadena, CA, March 2011.

[129]D. Lanza, J. Lyke, P. Zetocha, D. Fronterhouse, D. Melanson. Responsive Space Through Adaptive Avionics. *Responsive Space Conference*, Los Angeles, CA, April 19-22, 2004.

[130]J. Lyke. Space-Plug-and-Play Avionics (SPA): A Three-Year Progress Report, *Proceedings of the AIAA Infotech Conference*, 7-9 May 2007, Rohnert Park, CA.

[131]J. H. Christensen. Space plug-and-play architecture networking: A self-configuring heterogeneous network architecture. PhD. Dissertation, Utah State University, 2012.

[132]Y. Gao, K. Tu. A plug-and-play implementation method for general spaceborne device. *IEEE advanced information technology electronic and automation control conference*. Chongqing, China, 25-26 March 2017, 142-146; DOI: 10.1109/IAEAC.2017.8053994.

[133]Space Plug-and-Play Architecture: Standards Development Guidebook (AIAA G-133-1-2013e). https://doi.org/10.2514/4.102295.001.

[134]C. Lin, G. Chen, S. He, L. Chi. Overview of Space Plug-and-Play Avionics Interface Technology. *2020 International Conference on Computer Engineering and Application (ICCEA)*, Guangzhou, China, 18-20 March 2020, 34-38; DOI: 10.1109/ICCEA50009.2020.00015.

[135]J. Lyke, Q. Young, J. Christensen. Lessons Learned: Our Decade in Plug-and-play for Spacecraft. *28th Annual AIAA/USU Conference on Small Satellites*, 2014.

[136]C. Kief et al. The Advent of the PnP Cube Satellite. *IEEE Aerospace Conference*, Big Sky, MT, USA 3-10 March 2012; DOI: 10.1109/AERO.2012.6187237.

[137]C. J. McNutt, R. Vick, H. Whiting, J. Lyke. Modular Nanosatellites–(Plug-and-Play) PnP CubeSat. *7th Responsive Space Conference*, April 2009.

[138]F. Bruhn. QuadSatPnP: A Space-Plug-and play Architecture (SPA) Compliant Nanosatellite. Infotech@Aerospace, St. Louis, 2011.

[139]C. Kief, B. Zufelt, J. Christensen, J. Mee. Trailblazer: proof of concept CubeSat Mission for SPA-1. In *Infotech@ Aerospace 2011*, p.1473.

[140]D. Barnhart, L. Hill, M. Turnbull, P. Will. Changing Satellite Morphology through Cellularization. *AIAA SPACE 2012 Conference & Exposition,* September 2012; DOI: 10.2514/6.2012-5262.

[141]J. Lyke. Reconfigurable systems: A generalization of reconfigurable computational strategies for space systems. *IEEE Aerospace Conference*, Big Sky, MT, USA, 9-16 March 2002, pp. 4-4; DOI: 10.1109/AERO.2002.1036906.

[142]L. J. Hansen, D. Lanza. Creating standardized electronic data sheets for applications and devices. *2013 IEEE Aerospace Conference*, Big Sky, MT, USA, 2-9 March 2013, 1-8; DOI: 10.1109/AERO.2013.6496940.

[143]R. Gerard, R. R. Downs, J. J. Marshall, R. E. Wolfe. The Software Reuse Working Group: A Case Study in Fostering Reuse. *2007 IEEE International Conference on Information Reuse and Integration*, Las Vegas, NV, USA, 13-15 Aug. 2007, 24-29; DOI: 10.1109/IRI.2007.4296592.

[144]Quang M. Lam, Nick Stamatakos, Craig Woodruf, Sandy Ashton. Gyro Modeling and Estimation of Its Random Noise Sources. *AIAA Guidance, Navigation, and Control Conference and Exhibit*, Austin, TX, August 2003, 11–14; DOI: 10.2514/6.2003-5562.

[145]J. L. Crassidis, J. L. Junkins. Optimal Estimation of Dynamic systems, Goong Chen and Thomas J.Bridges, Eds. New York, USA: Chapma & Hall/CRC, 2004

[146]ANALOG DEVICES; URL: https://www.analog.com/media/en/technical-documentation/data-sheets/ADIS16400_16405.pdf.

[147]NSS Coarse Sun Sensor; URL: https://www.cubesatshop.com/wp-content/uploads/2020/11/NewSpace-Sun-Sensor_2020-10a.pdf.

[148]STIM277H Multi-Axis Gyro Module. URL: https://sensonor.azurewebsites.net/media/gwqdimq4/ts1672-r2-datasheet-stim277h.pdf.

[149]NSS Fine Sun Sensor; URL: https://www.cubesatshop.com/wp-content/uploads/2020/11/NewSpace-Sun-Sensor_2020-10a.pdf.

[150]NSS Magnetometer; URL: https://www.cubesatshop.com/wp-content/uploads/2020/11/NewSpace Magnetometer_11.2020_10a.pdf.

[151]CubeSTAR Star Tracker; URL: https://www.cubespace.co.za/products/adcs-components/cubestar/

[152]Arcsec Star Tracker; URL: https://www.cubesatshop.com/wp-content/uploads/2020/06/arcsec-Star-Tracker-Datasheet.pdf

[153]Nano Star Tracker ST-1; URL: https://nanoavionics.com/cubesat-components/star-tracker-st-1/

[154]J. Korczyc. Reliable On-Board Data Processing System for the ICEYE-1 satellite. Master's Thesis, 2016, p.53.